ESCOLA POLITÉCNICA
PROGRAMA DE PÓS-GRADUAÇÃO DE ENGENHARIA E TECNOLOGIA DE MATERIAIS
DOUTORADO EM ENGENHARIA E TECNOLOGIA DE MATERIAIS

DANIELI BORN GUERRA

NANOPARTICLES FOR RADIATION THERAPY ENHANCEMENT: INVESTIGATION OF RADIOSENSITIZATION INDUCED BY GOLD AND IRON OXIDE NANOPARTICLES IN GLIOBLASTOMA CELLS EXPOSED TO PHOTON AND PROTON BEAMS

Porto Alegre
2021

Ficha Catalográfica

G934n Guerra, Danieli Born

Nanoparticles for radiation therapy enhancement : Investigation of radiosensitization induced by gold and iron oxide nanoparticles in glioblastoma cells exposed to photon and proton beams / Danieli Born Guerra. – 2021.

107.

Tese (Doutorado) – Programa de Pós-Graduação em Engenharia e Tecnologia de Materiais, PUCRS.

Orientador: Prof. Dr. Ricardo Meurer Papaléo.

1. Radiotherapy. 2. radiosensitization. 3. human glioblastoma cells. 4. cancer nanotechnology. 5. nanoparticles. I. Papaléo, Ricardo Meurer. II. Título.

Elaborada pelo Sistema de Geração Automática de Ficha Catalográfica da PUCRS
com os dados fornecidos pelo(a) autor(a).
Bibliotecária responsável: Clarissa Jesinska Selbach CRB-10/2051

Pontifícia Universidade Católica do Rio Grande do Sul
Programa de Pós-Graduação em Engenharia e Tecnologia de Materiais

NANOPARTICLES FOR RADIATION THERAPY ENHANCEMENT: INVESTIGATION OF RADIOSENSITIZATION INDUCED BY GOLD AND IRON OXIDE NANOPARTICLES IN GLIOBLASTOMA CELLS EXPOSED TO PHOTON AND PROTON BEAMS

DANIELI BORN GUERRA

BACHELOR'S IN MEDICAL PHYSICS

MASTER IN MATERIALS ENGINEERING AND TECHNOLOGY

THESIS TO OBTAIN A DOCTOR'S TITLE IN ENGINEERING AND MATERIALS TECHNOLOGY

Porto Alegre

June, 2021

Pontifícia Universidade Católica do Rio Grande do Sul
Programa de Pós-Graduação em Engenharia e Tecnologia de Materiais

NANOPARTICLES FOR RADIATION THERAPY ENHANCEMENT: INVESTIGATION OF RADIOSENSITIZATION INDUCED BY GOLD AND IRON OXIDE NANOPARTICLES IN GLIOBLASTOMA CELLS EXPOSED TO PHOTON AND PROTON BEAMS

DANIELI BORN GUERRA

BACHELOR'S IN MEDICAL PHYSICS

MASTER IN MATERIALS ENGINEERING AND TECHNOLOGY

Advisor: Professor Dr. Ricardo Meurer Papaléo

Thesis developed at the Graduate Program in Materials Engineering and Technology (PGETEMA) at the Pontifical Catholic University of Rio Grande do Sul, as part of the requirements for obtaining the title of Doctor in Materials Engineering and Technology.

Porto Alegre
June, 2021

Pontifícia Universidade Católica do Rio Grande do Sul
ESCOLA POLITÉCNICA
PROGRAMA DE PÓS-GRADUAÇÃO EM ENGENHARIA E TECNOLOGIA DE MATERIAIS

NANOPARTICLES FOR RADIOTHERAPY ENHANCEMENT: INVESTIGATION OF RADIOSENSITIZATION INDUCED BY GOLD AND IRON OXIDE NANOPARTICLES IN GLIOBLASTOMA CELLS EXPOSED TO PHOTON AND PROTON BEAMS

CANDIDATA: DANIELI BORN GUERRA

Esta Tese de Doutorado foi julgada para obtenção do título de DOUTOR EM ENGENHARIA E TECNOLOGIA DE MATERIAIS e aprovada em sua forma final pelo Programa de Pós-Graduação em Engenharia e Tecnologia de Materiais da Pontifícia Universidade Católica do Rio Grande do Sul.

DR. RICARDO MEURER PAPALÉO - ORIENTADOR

BANCA EXAMINADORA

DR. FERNANDO LÁZARO FREIRE JUNIOR - DO DEPARTAMENTO DE FÍSICA - PUCRJ

DR. PEDRO LUIS GRANDE - DO INSTITUTO DE FÍSICA - UFRGS

DR. JARBAS RODRIGUES DE OLIVEIRA - PROGRAMA DE PÓS-GRADUAÇÃO EM BIOLOGIA CELULAR E MOLECULAR - PUCRS

DRA. ROSANE ANGÉLICA LIGABUE - DO PGETEMA - PUCRS

The present is theirs; the future, for which I really worked, is mine.
(Nikola Tesla)

PUCRS
Campus Central
Av. Ipiranga, 6681 - Prédio 32 - Sala 507 - CEP: 90619-900
Telefone: (51) 3353.4059 - Fax: (51) 3320.3625
E-mail: engenharia.pg.materiais@pucrs.br

DEDICATION

I dedicate these pages to all the teachers, friends and family who helped in my education. Especially to my mother, Ana Cristina Born, and to my father, José Aparício Guerra, pillars of my formation, both as a person and as a professional. Thank you for always being by my side and supporting me. I am grateful for the love, encouragement and dedication made to me, today and always.

ACKNOWLEDGEMENT

I am grateful for the opportunity given to me in this life. To my beloved parents, Ana and José, for the sacrifices made so that I could study. They have believed in me and always supported me in my choices.

I want to thank Prof. Dr. Ricardo Meurer Papaléo, for his guidance and patience, for having seen more potential in me than myself, and for his teachings over the years.

Dr. Fernanda Morrone, and the entire Laboratory of Applied Pharmacology, in helping and collaborating in the activities of the in vitro assays.

The research group of professors Coppes and Barazzuol, for giving me the opportunity to work and learn with them.

LABCEMM at PUCRS, especially Moema, for their patience in obtaining the TEM images

The radiotherapy team at Hospital São Lucas da PUCRS, helping with the irradiation experiments.

Bruna and Gabriel, my homemates in Groningen, for taking me in and helping me through the pandemic. I don't know what I would have done if I hadn't had you by my side at such a delicate time.

All colleagues in the NANOPUC group, for their support and help in the activities developed in the project, and for their fellowship and friendship. For the moments of relaxation, especially during our coffee break.

The "hehe" girls, for being always present showing me that I was not alone.

The "Nata intellectual", Elisa and Fernando, for helping me with the experiments and for the discussions about the project. For helping me to mature as a researcher and for always being willing to help.

Amanda, our IC , for being my lab partner and for staying with me until 10 pm at PUC (more than once). Without her I would not have been able to carry out the experiments.

My boyfriend Rodrigo (also known as Nito), for supporting me, and keep me company when I had to stay until 4:00 in the morning in the lab.

My colleagues at PGETEMA and friends who were by my side at various stages of my doctorate, especially in times of despair.

CAPES and the National Institute of Surface Engineering for financial assistance.

I thank everyone who contributed in some way to the realization of this work.

CONTENTS

FIGURES

TABLES

SYMBOLS

BSCS	Department of Biological Sciences of Cells and Systems
DSB	Double-strand break
DDR	DNA Damage Response
DLS	Dynamic Light Scatter
DMEN	Dulbecco´s Modified Eagle´s Medium
DMSO	Dimethyl Sulfoxide
DNA	Deoxyribonucleic acid
FBS	Fetal bovine serum
GBM	Glioblastoma
GNP	Gold Nanoparticle
HSL	Hospital São Lucas da PUCRS
ICP-MS	Inductively coupled plasma mass spectrometry
IMRT	Intensity Modulated Radiotherapy
IR	Ionizing radiation
LEE	Low energy electrons
LET	Linear energy transfer
LPL	Lethal, potentially lethal
LQ	Linear-Quadratic
MC	Monte Carlo
MTT	3-4,5-dimethyl-thiazol-2-yl-2,5-diphenyltetrazolium bromide
NHEJ	Non-homologous end-joining
NII	Nuclear Irregularity Index
NP	Nanoparticle
NTCP	Normal tissue complication probability
PBS	Phosphate-Buffered Saline
PCWC	Probability of cure without complication
PE	Platting efficiency
PEG	Polyethylene glycol
RBE	Relative biological effectiveness

RIF	Radiation induced foci
RNA	Ribonucleic acid
ROS	Reactive oxygen species
RT	Radiotherapy
SER	Sensitization enhancement factor
SF	Survival fraction
SPION	Superparamagnetic iron oxide nanoparticle
SSB	Single-strand break
SSD	Source to surface distance
SOBP	Spread out Bragg peak
TCP	Tumor control probability
TEM	Transmission electron microscopy
UMCG	University Medical Center of Groningen
Z	Atomic number

ABSTRACT

GUERRA, Danieli B. **Nanoparticles for radiation therapy enhancement: investigation of radiosensitization induced by gold and iron oxide nanoparticles in glioblastoma cells exposed to photon and proton beams.** Porto Alegre. 2021. PhD Thesis. Graduation Program in Materials Engineering and Technology, PONTIFICAL CATHOLIC UNIVERSITY OF RIO GRANDE DO SUL.

Radiotherapy (RT) is one of the most effective and widely used techniques for cancer treatment. Despite the great development of this technique, considerable efforts still need to be made to improve its efficacy and to maximize the differential response between tumor and healthy tissues. The use of nanomaterials as treatment enhancers hold great promises, potentially allowing the reduction of the delivered radiation dose. Recent studies have indicated that high atomic number nanoparticles show enhancement effects; however, with large variability between experiments and radiation type. Moreover, the underlying mechanisms of action are not well understood. Therefore, in this work we sought to improve the mechanistic knowledge about the radiosensitizing effect of metal-based nanoparticles, more specifically gold and iron oxide nanoparticles, in human gliobastoma cells irradiated with different radiation qualities. To further understand the impact of introducing NPs into cells exposed to radiation, five different variables were considered, i) NP material, ii) coating iii) treatment concentration, iv) cell type, and v) radiation quality. Findings from this work show the potential of using metal-based nanoparticles as radiosensitizers, relating the possible mechanisms involved in the radioenhancement observed.

Key-words: Radiotherapy, radiosensitization, human glioblastoma cells, cancer nanotechnology, nanoparticles.

RESUMO

GUERRA, Danieli B.: **Nanopartículas para o aprimoramento da radioterapia: Investigação da radiossensibilização induzida por nanopartículas de ouro e óxido de ferro em células de glioblastoma expostas a feixes de prótons e fótons.** Porto Alegre. 2021. Tese de Doutorado. Programa de Pós Graduação em Engenharia e Tecnologia de Materiais. PONTIFÍCIA UNIVERSIDADE CATÓLICA DO RIO GRANDE DO SUL.

A radioterapia (RT) é uma das técnicas mais eficazes e amplamente utilizadas para o tratamento do câncer. Apesar do grande desenvolvimento dessa técnica, esforços consideráveis ainda precisam ser feitos para melhorar sua eficácia e maximizar a resposta diferencial entre o tumor e os tecidos saudáveis. O uso de nanomateriais como potencializadores de tratamento traz grandes promessas, permitindo potencialmente a redução da dose de radiação fornecida. Estudos recentes indicaram que nanopartículas (NPs) de alto número atômico induzem o aumento de dose local; no entanto, há uma grande variabilidade entre experimentos e tipo de radiação utilizados. Além disso, os mecanismos de ação subjacentes não são bem compreendidos. Portanto, neste trabalho buscamos aprimorar o conhecimento sobre os mecanismos envolvidos no efeito radiossensibilizador de nanopartículas à base de metais, mais especificamente, nanopartículas de óxido de ferro e ouro, em células de gliobastoma humano irradiadas com diferentes tipos de radiação. Para entender melhor o impacto da introdução de NPs em culturas celulares expostas à radiação, cinco variáveis diferentes foram consideradas, i) material da NP, ii) revestimento iii) concentração de tratamento, iv) tipo de célula, e v) tipo de radiação. Os resultados deste trabalho mostram o potencial das nanopartículas metálicas como radiossensibilizadores, relacionando os possíveis mecanismos envolvidos no efeito de radiossensibilização observado.

Palavras-chave: Radioterapia, radiossensibilização, células de glioblastoma humano, nanotecnologia do câncer, nanopartículas.

1. INTRODUCTION

High energy radiations such as X-rays, gamma rays, electrons or heavy particles have been used since the early twentieth century as a potent method of diagnosis and therapy of various diseases, including cancer [1], [2]. In medicine, this has given rise to the field of cancer radiotherapy, where the primary goal of the treatment is to eradicate tumor cells while minimizing the effects to surrounding healthy tissues [2]. In modern treatment accelerators, shaping of the dose around the tumoral regions is possible to a certain extent employing multiple modulated radiation fields as in IMRT (Intensity Modulated Radiotherapy). The use of charged particles, such as protons, has proven to be another promising approach [3]–[9]. Due to their physical nature, charged particles can be used for more conformal dose delivery to the tumor than photon-based conventional irradiation techniques [10]–[12]. Despite huge advances in beam delivery methods, there is still needed to improve the therapeutic effectiveness of the technique, without increasing the damage to surrounding healthy tissues. One strategy to improve the dose discrimination between tissues involves the use of radiosensitizers.

In the last years there has been an increasing interest in utilizing nanoparticles (NPs) with high atomic number (Z) as radiosensitizers in cancer treatment [13]–[21]. Originally, the rationale for using high-Z materials as radiosensitizers was based on differences in the energy absorption properties of metals compared to soft tissues, allowing the physical increase of the dose deposited in the target volume [21]. Indeed, detailed Monte Carlo simulations [22], [23] indicate best physical performance for NPs of small radii and made of heavy elements such as gold [22]. According to the theory, NP-enhanced radiotherapy would only be effective with low energy (kV) X-rays, and no increase in overall dose deposition would be expected using higher energies (MV) [22], [23]. However, several *in vitro* studies have reported significant radiosensitization effects with MV X-rays [24]–[31]. Moreover, reported radiosensitization enhancement effects are usually larger than the predictions for the corresponding maximal physical

dose increase. Therefore, other mechanisms must be involved in the process, including chemical and biological effects triggered by the presence of the NPs. Moreover, experimental data on enhancement effects produced by various NPs on different biological systems show a large variability. Thus, results far from being conclusive, even for the most investigated case of photons beams [18]. The data is even more limited in the case of charged particle beams. Hence, despite the promising preclinical results of the nanoparticle-assisted radiosensitization strategy, especially with the use of high-Z NPs, several details of the complex cynergistic process of NPs in a radiative field within a biological system need to be clarified. One aspect is the suitable formulation of the nanoparticulated system, especially its surface functionalization and its impact on pharmacokinetic properties in *in vivo* systems. There are also gaps in the knowledge on the interaction of NPs with ionizing radiation and the subsequent biochemical and biological effects [14].

Thus, the general aim of this work was to investigate the basic mechanism of the radiosensitization process assisted by metal based NPs using an *in vitro* model, considering four different variables: i) NP material, ii) NP concentration, iii) cell type and iv) radiation quality. We evaluated the radiosensitization effects induced by gold (GNPs) and superparamagnetic iron oxide (SPION) nanoparticles in human gliobastoma (GBM) cells irradiated by different types of high-energy beams (photons and charged particles). GNPs have attracted a lot of attention due to their unique properties that include high photon attenuation coefficient, excellent biocompatibility, surface plasmon resonance, possibility of radioactive activation, in addition to being easily linked to biomolecules that bind to cellular receptors present in the cancerous tissue [32], [33]. SPIONs were a case for which local dose enhancement is considered to be negligible due to its low effective Z. As the presence of SPIONs have been associated to the production of reactive oxygen species in cells [34], it allows to evaluate the importance of chemical and catalytical effects in the radiosensitization process. Moreover, due to their unique magnetic properties, SPIONs are excellent candidates for theranostics agents which could be employed in MRI-guided radiotherapy to improve both tumor localization via medical imaging, as well as the treatment efficacy.

This work has been performed as an interdisciplinary effort between the Center of Nanoscience and Micro-Technology (NanoPUCRS), the Applied Pharmacology Laboratory, and the radiotherapy division of Hospital São Lucas da PUCRS (HSL). And

supported by the National Institute of Surface Engineering (INCT-INES). The work was also complemented by a 6 month stay at the BSCS in Groningen, with a sandwich grant from CAPES-PrInt program. Photon irradiations were performed in the Radiotherapy Center of Hospital São Lucas da PUC in a 6 MV clinical accelerator. Gamma ray irradiations were performed during my six-month sandwich PhD in the Netherlands, at University Medical Center of Groningen (UMCG) in the Biomedical sciences of cells and systems (BSCS). Beyond that, a pilot study with 150 MeV H^+ beam was also conducted at the UMCG PARTREC cyclotron facility in Groningen. Due to the pandemic, we were not able to complete the study. The sandwich grant was provided by the CAPES-PrInt internationalization project of PUCRS under the subject “Development of innovative health technologies and processes”.

.

2. GOALS

This study aims to investigate the radiosensitization induced by gold and iron oxide nanoparticles in human glioblastoma cells exposed to photon and proton beams.

2.1. **Especific goals**

- Evaluate the cytotoxicity of gold and iron oxide nanoparticles at different concentration treatments in U87 and M059J human glioblastoma cells.

- Determine the nanoparticle internalization within the cells and quantify the cellular elemental uptake, correlating these factors with the dose enhancement induced by the presence of gold and iron NPs.

- Assess the overall characteristics of the NP-induced radiosensitization process, evaluating the impact of nanoparticle design, cell line, treatment concentration and beam quality on the radiosensitization effect induced by gold and iron oxide nanoparticles.

- Investigate the interaction of the nanoparticles with different types of ionizing radiation on the DNA Damage Response (DDR) in U87 human glioblastoma cells.

3. FUNDAMENTALS

3.1. Interaction of ionizing radiation with matter

Ionizing radiation (IR) is characterized by its ability to excite and ionize the atoms, being capable of transforming large amounts of energy and to damage the medium with which it interacts. Examples of ionizing radiation are X-rays, γ-rays, fast electrons, charged particles (protons and ions) and neutrons. Ionizing radiation has many possible mechanisms of interaction with matter. The predominant mechanisms are described below:

3.1.1. Interaction of photons with matter

Photons can interact with matter through different processes, depending on the energy of the photons involved and the chemical composition of the target material [1], [35]. Photon interactions are stochastic in nature. In each interaction, secondary particles are created, which may be charged (usually electrons) or uncharged (photons)[1]. The secondary particles deposit their energy around the location of the interaction and spread the deposited energy to larger volumes in the material. [36].

There are three main mechanisms involved in the loss of energy by photons: the photoelectric effect, the Compton scattering and production of pairs. These processes lead to the partial or complete transfer of energy from the photon to the electrons of the target atoms that can be ionized or excited [37]. Electrons removed from atoms can obtain sufficient kinetic energy to cause secondary ionizations of other atoms in the target material (electron cascade). Such electrons are called δ-rays Depending on the energy of the photons and the atomic number of the material, different mechanisms dominate the process of energy deposition. Figure 3.1 shows the predominant Energy regions of each type of interaction.

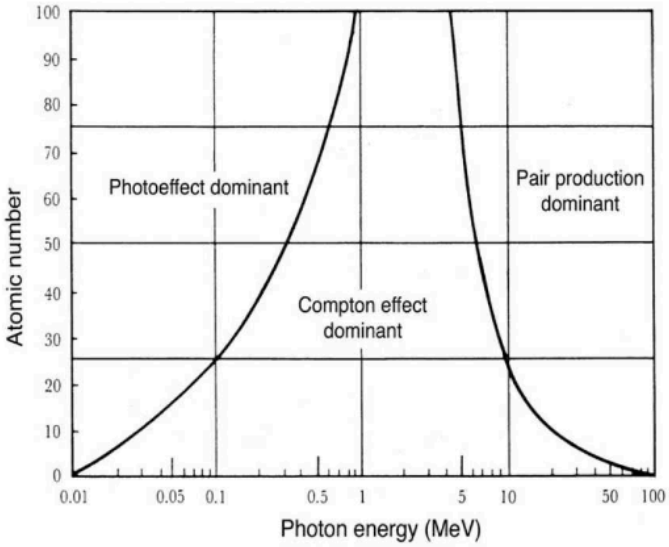

Figure 3.1. Regions of relative predominance of the three main processes of photon interaction with matter. The left curve representes the region where the cross-sections for photoelectric effect and Compton effect are equal, the righ curve representes the region where Compton effect is equally probable to pair production. Addapted from [37], [38]).

In radiotherapy, the interaction of photons with soft tissues, whose effective atomic number is close to that of water (Z_{eff} = 7.4), is dominated by Compton scattering [39]. In this range of energies (of the order of 1 MeV), the mass attenuation coefficient of lead and water does not differ much, as this type of interaction is weakly dependent of the atomic number (Figure 3.2). The photoelectric effect dominates for lowt energy photons, while the production of pairs dominates at high energies [40].

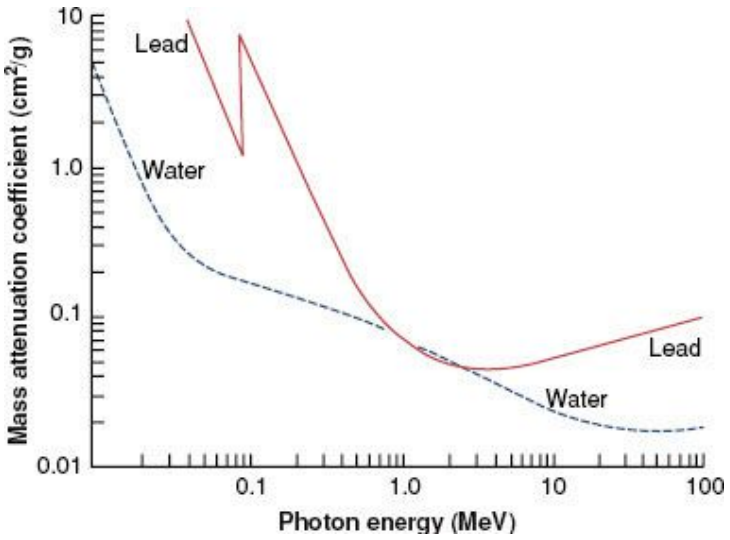

Figure 3.2. Mass attenuation coefficient as a function of photon energy for lead and water. Addapted from [41].

3.1.2. **Interaction of charged particles with matter**

Depending on its velocity, charged particles (projectile) may experience interaction with the target particles by means of inelastic scattering (electron-ion collisions), elastic scattering (nucleus-ion collisions), induction of nuclear reactions, orradiation emission [42]. Inelastic scattering occurs by electronic interaction and results in excitation / ionization of atoms and transfer of kinetic energy to electrons. The nuclear interactions (elastic scattering) transfer energy and momentum directly to the atoms of the target vi Coulomb scattering, providing atomic displacements and collisions. At sufficiently high E, nuclear interactions may also be in the for of nuclear reactions and excitations, comprising several reaction products, such as electrons, neutrons, γ-radiation, and eventually further hadrons. In the range of energies required for proton radiotherapy (of 70 MeV to about 250 MeV), in which the energy used in this work falls, only the inelastic interactions are significant.

At the start of the path through the body, energy transfer of protons is small and its path remains straight. After successive scattering events the protons will slow down, the energy deposition increases dramatically and reaches a maximum. In this region the dose varies almost inversely with the remaining proton energy (see Fig. 3.3 (a)). After some more straggling the protons come to a complete stop. The peak of dose deposition as a function of depth is known as the Bragg peak. The characteristic Bragg peak defining a range for protons in matter, in contrast to x-ray radiation, is the main argument for protontherapy. Within the region of the Bragg peak the energy loss per distance travelled is highest and so is the dose and killing effect for cancerous tissue. In this In Fig. 3.3 (a) the range of protons and of x-rays is compared. The x-ray dose piles up below the surface, goes through a maximum and then drops off without a defined range. In contrast, with protons and other ions the Bragg peak of highest dose can be placed right into the region of the cancer volume by tuning the initial energy of the proton beam. By varying the incident proton energy and beam intensity a Bragg peak plateau is formed that covers the entire cancer volume (Fig. 3.3 (b)). The plateau region is known as *Spread-out Bragg peak* (SOBP).

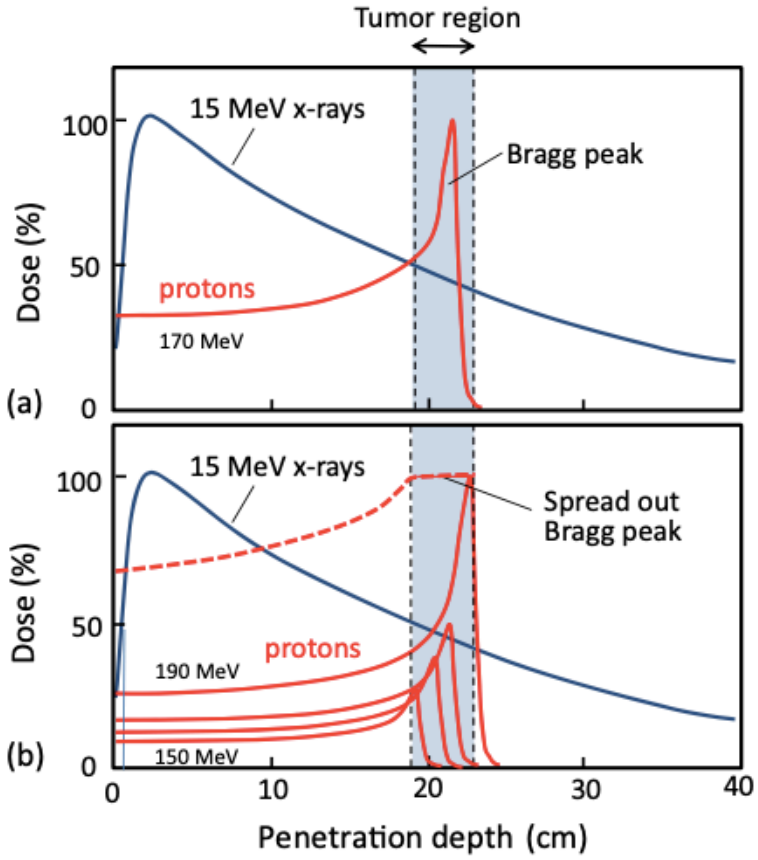

Figure 3.3. a) Comparison of dose versus depth for x-rays and protons. Plots are normalized to maximum dose. By varying the incident energy and intensity of the proton beam a plateau region (spread out Bragg peak – SOBP) of the size of the tumor is formed. Adapted from [41].

3.2. **Interaction of Ionizing Irradiation with biological systems**

The biological effects of radiation are the product of a long series of phenomena which are set in motion by the passage of radiation through the medium. The initial events are ionizations and excitations of the atoms and molecules of the medium along the track of the ionizing particles. These physical perturbations lead to phyco-chemical reactions, then chemical reaction and finally the biological effects [43]–[45]. These processes differ enormously in time-scale [43], as it is illustrated in Figure 3.4 and may be divided into three phases [43], [46], [47], described below.

The **physical phase** consists of interactions between charged particles and the atoms of which the tissue is composed. A high-speed electron takes about 10^{-18} s to traverse the DNA molecule and about 10^{-14} s to pass across a mammalian cell. As it does so, it interacts mainly with electrons, ejecting some of them from atoms

(ionization) and raising others to higher energy levels within an atom or molecule (excitation). If sufficiently energetic, these secondary electrons may excite or ionize other atoms near which they pass, giving rise to a cascade of ionization events.

The **chemical phase** describes the period in which these excited atoms and molecules react with other cellular components in rapid chemical reactions. Ionization and excitation lead to the breakage of chemical bonds and the formation of free radicals. These are highly reactive, and they engage in a succession of reactions that lead eventually to the restoration of electronic charge equilibrium. Free-radical reactions are complete within approximately 1 ms of radiation exposure. An important characteristic of the chemical phase is the competition between elimination reactions with fixation reactions that lead to stable chemical changes in biologically important molecules.

The **biological phase** includes all subsequent processes. The effects caused by ionizing radiation may occur at any level of organization of the living species, ranging from single molecules within individual cell to its tissues and organs. At the basic molecular level, ionizing radiation causes damage to all molecules in the cell. However, there are multiple copies of most molecules (e.g., water, mRNA, proteins, and others) and most undergo a continuous rapid turnover, limiting the consequences of damaging just a few molecules of one type. In contrast, DNA is present only as a single, double-stranded copy, is the largest molecule in the cell, and is central to all cellular functions. A series of cellular processes are activated to repair radiation-induced damage and most lesions are successfully repaired. Unrepaired or incorrectly repaired damage of the DNA may lead to potentially malignant cell transformation or to cell death [48]. At later times after the irradiation of normal tissues the so-called ‘late reactions’ appear. These include fibrosis, spinal cord damage and blood vessel damage. An even later manifestation of radiation damage is the appearance of second tumors (i.e., radiation carcinogenesis). The timescale of the observable effects of ionizing radiation may thus extend up to many years after exposure.

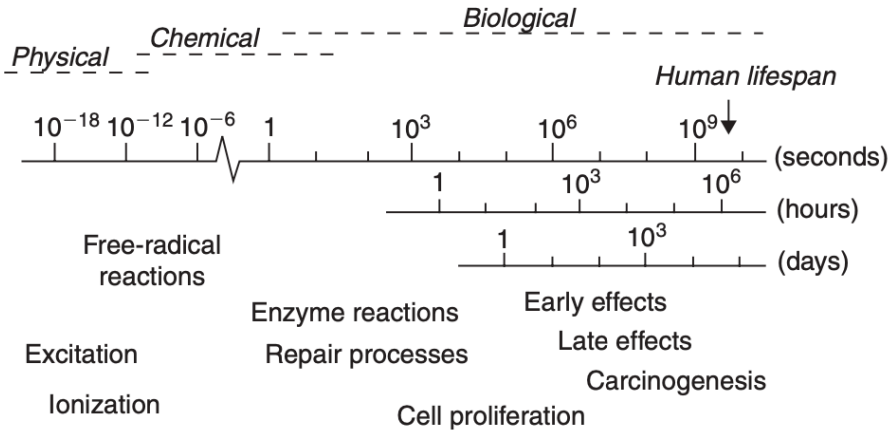

Figure 3.4. Time-scaleof the effects of radiation exposure on biological systems. Addapted from Kogel 2009 [47].

3.2.1. **Irradiation-induced damage and the DNA damage response**

3.2.1.1. DNA structure

Before studying the effects of radiation on DNA, it is necessary to know its composition. The most common form of the DNA double helix is also called B-form DNA. Each strand is a polynucleotide, meaning the strand is made up of many individual units called nucleotides. A nucleotide has three components, a five-carbon sugar (deoxyribose), a phosphate group, and one of four possible nitrogenous bases: adenine (A), guanine (G), thymine (T), and cytosine (C). The nitrogenous base is always attached at the one prime carbon of the sugar. Nucleotides attach to each other in the DNA strand by phosphodiester bonds. The phosphate group of one nucleotide binds to the three-prime oxygen of the neighbouring nucleotide. Thus, the sugars and phosphate groups make up the DNA backbone. Although the nucleotides come together through covalent bonds in the backbone, the two DNA strands interact through non-covalent hydrogen bonds between the bases. Each base forms multiple hydrogen bonds with its complementary base on the opposite strand. Bound together by hydrogen bonds, each unit is called a base pair. The hydrogen bonding contributes to the specificity of base pairing. Thymine preferentially pairs with adenine through two hydrogen bonds and cytosine preferentially pairs with guanine through three hydrogen

bonds. Thymine and cytosine are called pyrimidines, characterized by their single ring structure, and adenine and guanine are called purines, which have double rings.

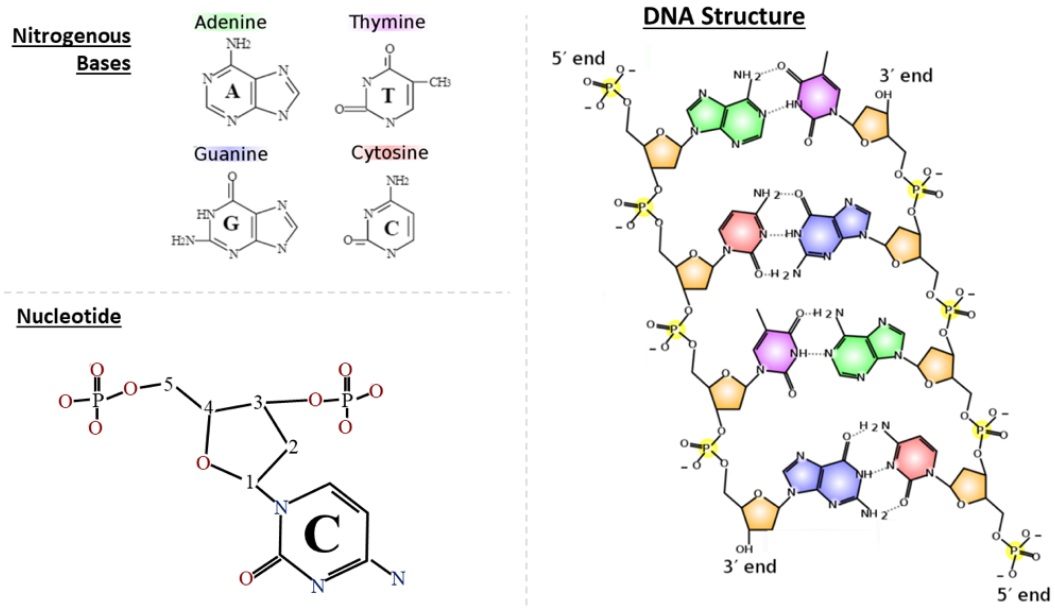

Figure 3.5. DNA molecule model. Representation of DNA structure and chemical composition. Nitrogen bases, structure and nucleotide binding. Source: the author.

The geometry of the AT or TA and GC or CG base pairs is the same, allowing for symmetry and base stacking in the helix. This mostly has to do with the distance between the backbones and the angles to which the bases attach to the backbone. Other base pairs, like GT, for example, do not have the same geometry, cannot form strong hydrogen bonds, and disturb the helix. Each turn of the helix measures approximately ten base pairs. In addition to the hydrogen bonding between the bases, the stacking of the bases also stabilizes the double helix structure.

3.2.1.2. Low Energy Electrons and Direct DNA Damage

If any form of radiation is absorbed in biologic material, there is a possibility that it will interact directly with the DNA. Molecules of the single DNA strand, or both strands, may be ionized or excited. The secondary ionizations produced by emitted energetic electrons set many more low-energy electrons in motion causing additional excitation and ionization along the path of the initial energetic electron. For example, a single 30 keV electron, set in motion following the photoelectric absorption of a single

x-ray or gamma-ray photon, can result in the production of over 1,000 low-energy secondary electrons, each of which may cause additional excitation or ionization events in the tissue. At the end of electron tracks, interactions with other molecules become more frequent, giving rise to clusters of ionizations [49].

The δ-rays and other lower energy electrons produce a unique ionization pattern in which closely spaced ionizations occur over a very short range (~4 to 12 nm) along the path of the primary particle track. The energy deposition along the shorter tracks is referred to as spurs, and their diameters are approximately 4 to 5 nm. Longer and less frequent pear-shaped tracks called blobs deposit more energy (~300 to 500 ev) and thus on average result in more ionization events over their path (~12 nm)[50]. The high concentrations of reactive chemical species produced by these spurs and blobs increase the probability of molecular damage at these locations. If ionizing events occur near the DNA, whose diameter (~2 nm) is on the same order as that of these short ionization tracks, they can produce damage in the DNA in multiple locations in close proximity to one another. These complex lesions are more difficult for the cell to repair or may be repaired incorrectly. The pattern and density of ionizations and their relationship with the size of the DNA double helix is shown in Figure 3.6. The clusters are such that many ionizations can occur within a few base pairs of the DNA.

The complex clustered damage involving several damaged nucleotides within one or two helical turns of the DNA, is a hallmark of ionizing radiation-induced DNA damage. Only a few per cent of the damage is clustered, but when these clusters occur in DNA, the cell has particular difficulty coping with the damage. Ionized molecules are highly reactive and undergo a rapid cascade of chemical changes, which can lead to the breaking of chemical bonds. This can disrupt the structure of macromolecules such as DNA, leading to severe consequences if not repaired adequately or in time.

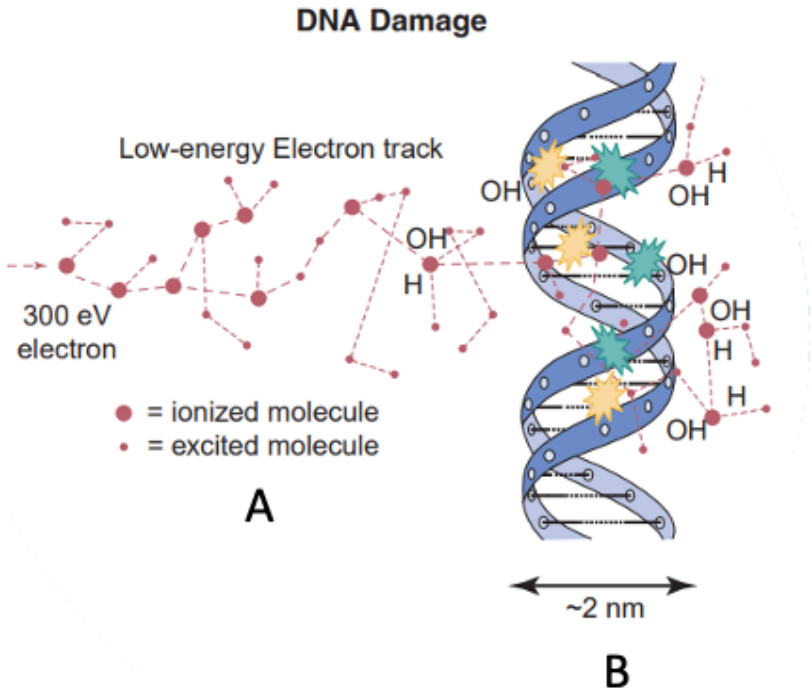

Figure 3.6. A) A segment of the electron track produced by ionizations and excitations along the path of a low-energy (300 eV) electron. B) DNA double helix drawn on the same scale as the ionization track. Direct and indirect damage is represented. Multiple damaged sites are shown as green, or orange, explosion symbols that denote DNA strand breaks, or damaged bases, respectively. (Adapted from [49], [51]).

3.2.1.3. Indirect damage

Indirect action refers to effects that are the result of radiation interactions within the medium (e.g., cytoplasm) that create chemically reactive species that in turn interact with nearby macromolecules. Because most of cells in the body are composed of water (75−85% of the cell mass), most of the radiation-induced damage from medical irradiation is caused by radiation interactions with water molecules. The interaction of highly energetic radiation with water initially results in the ejection of a quasi-free electron from the valence shell in general, leaving behind a positively charged radical cation ($H_2O^{\bullet+}$)[52]. In addition to their recombination, both charged species subsequently follow their own pathway of chemical reactivity. The hot electron relaxes and gets trapped as a hydrated electron (e_{hyd}^-), whilst $H_2O^{\bullet+}$ rapidly reacts with another non-ionized water molecule to form aqueous hydrogen (hydrogen captured by a molecule of water) and a hydroxyl radical ($OH^{\bullet}$) via proton transfer. The hydroxyl is highly reactive and may diffuse a short distance to reach a critical target in the DNA within the cell nucleus. After 10^{-12} seconds, radiolytic species (clusters) with longer

lifetimes (~10^{-6} seconds) are formed. They will diffuse into the solution and can also react to each other in numerous ways. Some of the recombination pathways are radical-radical reactions, which give rise to the formation of molecular products such as hydrogen (H_2), hydrogen peroxide (HOOH) and water.

At the end of a microsecond, the distribution of radicals and molecular species reaches equilibrium in the solution and the homogeneous chemical phase begins. The primary species can continue to react with each other, or they can act as strong oxidizing or reducing agents by combining directly with macromolecules. In the case of DNA bases, the main decomposition of the intermediate product is the elimination of the hydrogen atom, which gives rise to a stable hydroxyl product. Neutral radicals can also give rise to carbon-carbon linkages in phosphate bridges or in deoxyribose causing breaks in the DNA chain.

3.2.1.4. Spectrum of DNA damage

Indirect action constitutes about 70% of the total damage produced in DNA after low-LET radiation, such as X-rays, whereas direct interaction is the dominant process when high-LET radiation interacts with living organisms [11], [53], [54]. The damage to DNA resulting from the indirect and direct action of radiation is in principle similar. The type and frequency of the induced damage depends on the geometrical distribution of ionization events. The chemical changes may include (1) hydrogen bond breakage, (2) molecular degradation or breakage, and (3) intermolecular and intramolecular cross-linking.

The rupture of the hydrogen bonds that link base pairs in DNA may lead to irreversible changes in the secondary structure of the molecule that compromise genetic transcription and translation. Molecular breakages may also involve the sugar-phosphate polymers that comprise the backbones of the two helical DNA strands. They may occur as single-strand breaks (SSBs), double-strand breaks (DSBs) (in which both strands of the double helix break simultaneously at approximately the same nucleotide pair), base loss, base changes, or cross-links between DNA strands or between DNA and proteins. A DSB can occur if two SSBs are juxtaposed or when a single, densely ionizing particle (e.g., an alpha particle) produces a break in both strands. SSBs (caused in large part by the $OH^{\bullet}$ radical) are more easily repaired than DSBs and are more likely to result from the sparse ionization pattern. While DSBs and

complex DNA damage are less likely to be repaired [55]. Figure 3.7 illustrates some of the common forms of damage to DNA.

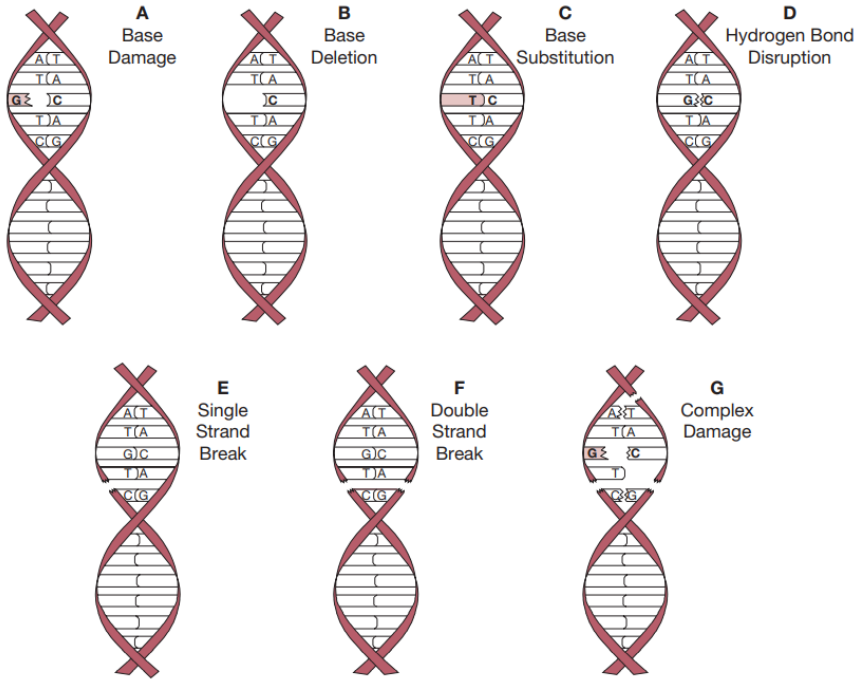

Figure 3.7. Several examples of DNA damage. Addapted from [51].

3.2.1.1. DNA damage response

The DNA damage response (DDR) is a highly complex and coordinated system that determines the cellular outcome of DNA damage caused by radiation [47]. The DDR is not a single pathway, but rather a group of highly interrelated signalling pathways, each of which controls different effects on the cell. This system can be divided into two parts, the sensors of DNA damage and the effectors of damage response. The sensors consist of a group of proteins that actively survey the genome for the presence of damage. These proteins then signal this damage to three main effector pathways that together determine the outcome for the cell.

The initial cellular response to DSBs is characterized by the physical recruitment of a large number of different proteins to the sites of DNA damage. This clustering or recruitment of various proteins can be visualized microscopically as small regions or speckles in the nucleus after DNA damage following staining with antibodies to these

proteins (Fig. 3.8). These subnuclear regions are commonly referred to as ionizing radiation induced ‘foci’ (RIF). One of the earliest events known to occur in the DDR is the phosphorylation of a protein called histone H2AX [56]. Starting within a few minutes of DSB formation, H2AX becomes phosphorylated in a region that extends over an extensive region around the site of the unrepaired DSBs [56], [57]. This phosphorylated form, known as γH2AX, is necessary for the recruitment of many of the other proteins involved in the DDR and the resulting formation of RIF.

Another protein that accumulates at sites of DSBs is 53BP1 [58]–[61], which is an important regulator of non-homologous end-joining (NHEJ)-mediated DSB repair and a p53-binding protein 1. In recent years, the presence of γH2AX and 53BP1 foci, which can be detected using microscopy, has become a highly sensitive method for detecting the presence and/or repair of individual DSBs in irradiated cells, and it is also used in this Thesis.

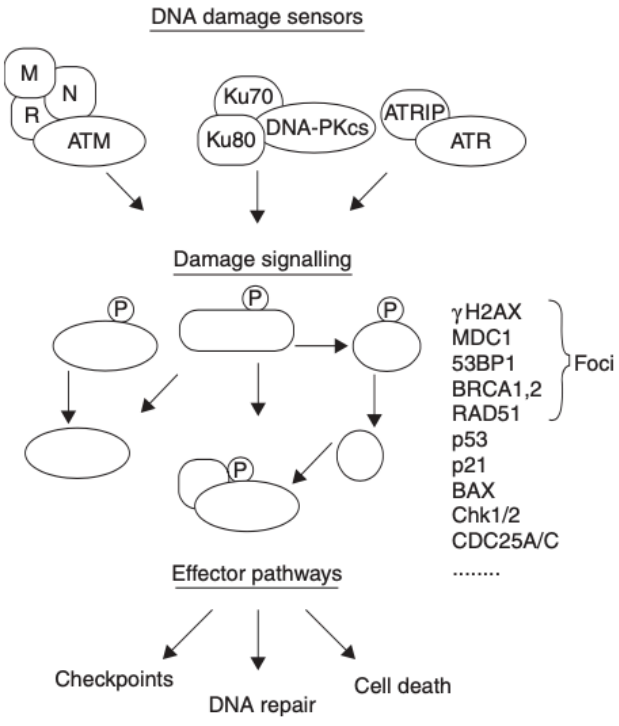

Figure 3.8. The DNA damage response can be divided into sensors and effectors. The sensors consist of protein complexes which recognize DNA damage. These proteins signal to many other proteins which activate three important effector pathways: checkpoints, DNA repair and cell death. Examples of some of the proteins which signal from the sensors to the effector pathways are listed.

3.2.2. **Quantifying cell kill and cell survival**

3.2.2.1. Concept of clonogenic cells and survival curve

In radiobiology, ’cell death’ means that the cell loses its reproductive or clonogenic activity, or it is no longer able to continue its tissue-specific functions [4], [46], [47], [62], [63]. In a small minority of cell types, cell death occurs rapidly, immediately or within several hours after irradiation. The vast majority of proliferating normal and tumour cells die at a relatively long time after irradiation, usually after attempting mitosis one or more times (mitotic catastrophe). Following a transient delay, most cells resume proliferation and progress through the cell cycle one, two or more times before eventually permanently ceasing proliferation [47]. In this case, cell death does not occur until after the cell attempts to divide. In cells that die at long times after irradiation, the DDR is unable to induce apoptosis and DNA repair is allowed to take place and can have a large influence on the outcome and radiosensitivity of the cell. Cells that experience mitotic catastrophe may ultimately undergo a secondary form of programmed cell death such as apoptosis, autophagy, necrosis, or senescence.

Therefore, researchers have focused on assessing clonogenic survival, which is defined as the ability of a cell to proliferate indefinitely. This is a relevant parameter to assess the efficacy of radiation treatment, since any tumor cell that retains proliferative capacity can cause failure in tumor growth control. Consequently, cell death in the context of radiobiology is generally equated with any process that leads to the permanent loss of clonogenic capacity [4], [46], [47], [62], [63].

Along this line, clonogenic assay or colony formation assay is the method of choice to determine cell reproductive death after treatment with ionizing radiation [47], [64]. It is an *in vitro* cell survival assay based on the ability of a single cell to grow into a colony. The assay essentially tests every cell in the population for its ability to undergo ‘‘unlimited’’ division. By convention it was stipulated that if a single cell grows into a colony of at least 50 daughter cells after exposure to ionization radiation it has retained its reproductive capacity [64]. The necessary steps to carry out such assay will be discussed in detail in the methodology section. Even if a cell is not irradiated, not all seeded cells will form a colony. The factor indicating the percentage of cells seeded, which grow into colonies is called ‘plating efficiency’ and is given by the formula:

$$PE = \frac{n_o\ of\ colonies\ formed}{n_o\ of\ cells\ seeded} \times 100 \quad (3.8)$$

Different cell lines have different plating efficiencies. The number of cells seeded per dish is adjusted to the expected survival following the exposure to a dose of radiation. The number of colonies that arise after treatment of cells, expressed in terms of PE, is called the surviving fraction (SF):

$$SF = \frac{n_o\ of\ colonies\ formed\ after\ treatment}{n_o\ of\ cells\ seeded \times PE} \times 100 \quad (3.9)$$

Based on SF, we can obtain the dose-survival dependence (the survival curve for cells in culture). When the survival curve of cells irradiated in tissue culture is plotted on linear scales, it is often sigmoid: there is a shoulder followed by a curve that asymptotically approaches zero survival (Figure 3.9). Therefore, cell survival curves are usually plotted on semi-logarithmic coordinates (log SF as a function of D). This type of plot emphasizes the very small values of SF at high doses, more easily allowing us to see and compare the very low cell survivals required to obtain a significant reduction in tumour size, or local tumour control. The type of the cells, their oxygen status, the phase in the cell cycle they are irradiated at, and type (LET) of radiation are factors which affect the shape of the cell survival curve.

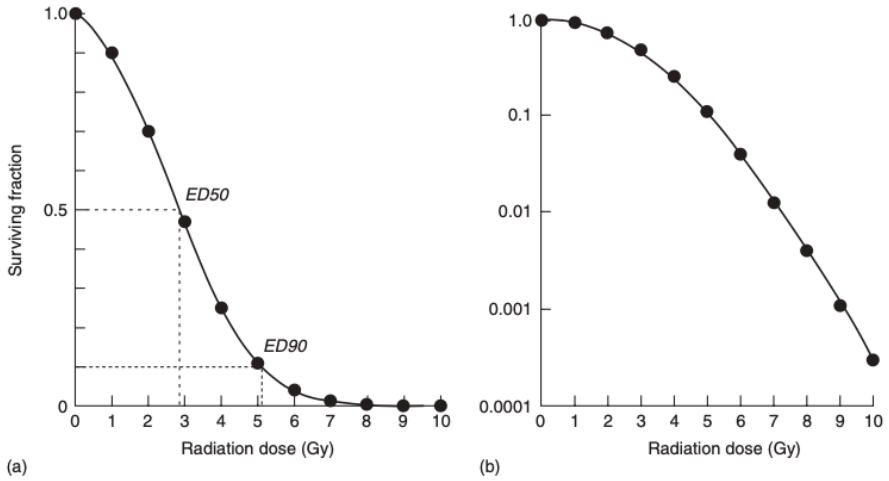

Figure 3.9. A typical cell survival curve for cells irradiated in tissue culture, plotted a) on a linear survival scale. ED50 and ED90 correspond to the dose that kills 50% and 90% of the cells, respectively. b) The same data on a logarithmic scale. Adapted from [47].

For comparing SF curves, it is convenient to represent these curves by mathematical functions. These are based on hypothetical models of cell death. For the purpose of this work, two descriptions will be discussed: the linear-quadratic (LQ) model and the Lethal Potentially-Lethal (LPL) model. Details about other descriptions may be found elsewhere [43], [47].

The continually downward bending form of a cell survival can simply be fitted by an expression containing a linear and a quadratic component in the exponent, as follows:

$$SF = \exp(-\alpha D - \beta D^2) \tag{3.10}$$

When compared to previous mathematical models, sometimes even more complicated (e.g. two-component model [46]), the simple LQ formula gives a better description of radiation response in the low-dose region (0–3 Gy): LQ survival curves are continuously bending with no straight portion either at low or high radiation doses. The shape (or 'bendiness') is determined by the ratio α/β. Since the dimensions of the parameters for α are Gy^{-1} and for β are Gy^{-2}, the dimensions of α/β ratios are Gy. The LQ model is now in widespread use in both experimental and clinical radiobiology and generally works well in describing responses to radiation *in vitro* and *in vivo*.

Curtis et. al [65] suggested a radiobiology significance of these parameters in his LPL (lethal, potentially lethal) repair model. The model assumes that two different kinds of lesions relevant to cell killing are created within a cell during irradiation: "lethal" and "potentially lethal" lesions. Lethal lesions are irreparable and lead to the death of the cell or its progeny. The non-repairable such as double strand brakes (DSBs) or complex damage are more likely to be form by direct damage produced by single-hit lethal effects resulting in the linear component of survival fraction [$\exp(-\alpha D)$]. Potentially lethal lesions are capable of being repaired and are correctly repaired at and average rate constant ϵ_{PL} per unit time. These lesions may also interact with each other with rate constant ϵ_{2PL} per unit time to produce a lethal lesion (irreparable). The latter process is called binary misrepair. Therefore, the repairable lesions depend on the competition between the repair and the binary misrepair processes leading to a quadratic component in cell survival [$\exp(-\beta D^2)$]. Repairable damages are more likely to be produced by indirect damage, such as free radical-induced damage to DNA,

resulted from the formation of ROS during radiation, as discussed previously. The authors define the linear and quadratic coefficients, α and β, respectively:

$$\alpha = \eta_L + \eta_{PL} e^{-\epsilon PL/r} \quad (3.11)$$

$$\beta = \frac{\eta_{PL}^2}{2\epsilon} (1 - e^{-\epsilon PL/r})^2 \quad (3.12)$$

The model has two sensitivity parameters (η_L determines the number of non-repairable lesions produced per unit dose, and η_{PL} the number of repairable lesions). This model can provide a possible mechanistic interpretation of the LQ equation. It predicts that, as dose rate is reduced, the probability of binary interaction of potentially lethal lesions will fall and parameter values can be found that allow the model accurately to simulate cell survival data on human and animal cells irradiated at various dose rates.

3.2.2.2. Linear Energy Transfer (LET)

In radiobiology and radiation protection the physical quantity that is most relevant for defining the quality of an ionizing radiation beam is the linear energy transfer (LET). In contrast to the stopping power, which focuses attention on the energy absorption by the medium, the LET measures the linear rate of the energy loss by energetic particles moving through a medium [10], [11], [66]. The LET at a point on the track of an ionizing particle represents the mean energy absorbed by the medium per unit lenght [67]. A more detailed treatment separates the contributions of the δ-rays, considered as independent of the particles from which they arose. The energy deposited in the medium close to the track is defined by the energy transfers, which are below a specified cut-off energy, Δ (usually expressed in eV):

$$LET_\Delta = -\left(\frac{dE_\Delta}{dx}\right)_{el} \quad (3.15)$$

At a first aproximation, LET is equivalent to the restricted collisional (electronic) stopping power. By including all possible energy transfers, one obtains the unrestricted LET_∞ which is equivalent to the total electronic stopping power:

$$LET_{\infty} = -\left(\frac{dE}{dx}\right)_{el} \tag{3.14}$$

For a given particle with defined incident energy, LET is not constant along the track. This variation is especially noticeable at Bragg peak [68], where the deposited dose can be 100 times greater than none of the rest of track [69].

Depending on the value of LET which characterizes a specific radiation, one may distinguish between high-LET and low-LET radiations. For example, α-particles and charged particles heavier than He are called high-LET radiation, because they cause dense ionization along their tracks. In contrast, X- and γ-rays are recognized as low-LET radiations as they produce sparse and randomly distributed isolated ionization events. The considerable difference between low- and high-LET charged-particle tracks is illustrated in passing through a cell nucleus is shown in Figure 3.10.

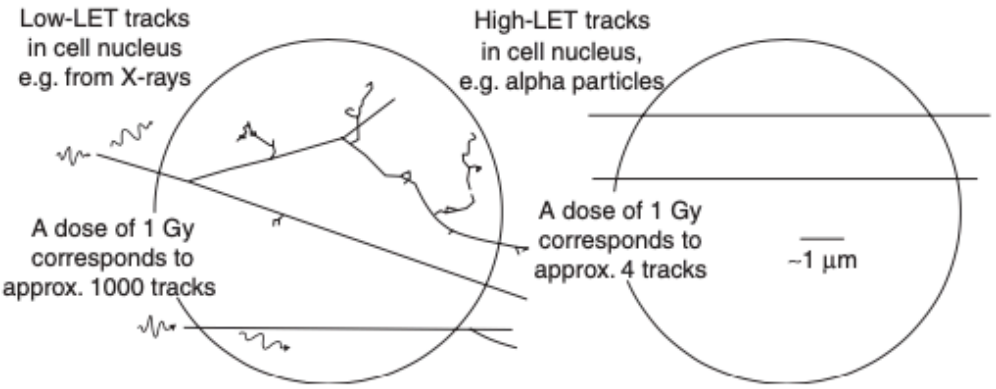

Figure 3.10. Particle track structure for low-LET radiation (left) and for a-particles (right). The circles represent the typical size of the nucleus of a mammalian cell. The tortuous/twisting nature of the low-LET secondary electron tracks are in complete contrast to the high-LET particles, of which only around four are required to deposit a dose of 1 Gy in that small volume. Adapted from [70].

At the scale of the cell nucleus, the γ-rays deposit much of their energy as single isolated ionizations or excitations and much of the resulting DNA damage is efficiently repaired by enzymes within the nucleus. About 1000 of these sparse tracks are produced per gray of absorbed radiation dose. The α-particles produce fewer tracks but the intense ionization within each track leads to more severe damage where the track intersects vital structures such as DNA. The resulting DNA damage may involve several adjacent base pairs and will be much more difficult or even impossible to repair.

3.2.2.1. Relative biological effectiveness (RBE)

As LET increases, radiation produces more cell killing per gray, until a certain level of LET is reached [71].The factor which describes differences in the response of cells to doses of radiation of different quality is called relative biological effectiveness (RBE). The RBE of a radiation under test is defined as the ratio of the dose of reference, low-LET radiation (usually 250 kVp X-rays or ^{60}Co γ-rays) to that of high-LET tested radiation required to give the same biological effect.

$$RBE = \frac{dose\ of\ reference\ radiation}{dose\ of\ test\ radiation} \tag{3.16}$$

The RBE value depends on the biological endpoint under consideration. The RBE cannot be uniquely defined for a given radiation, since it depends on many different factors, as the dose, dose per fraction, degree of oxygenation, cell or type of tissue [43], [47]. The RBE also depends on LET, and rises to a maximum at an LET of about 100keV/μm, then falls for higher values of LET because of overkill. Densely ionizing, very high-LET radiation becomes inefficient because it deposits more energy per cell, and hence produces more DNA double-strand breaks than are actually needed to kill the cell. These cells are ‘overkilled’, but others will receive no dose or too low dose levels, leading to a reduced biological effect. Radiation of optimal LET deposits the right amount of energy per cell, which produces just enough DNA damage to kill the cell. This optimum LET is usually around 100 eV/Å but does vary between different cell types and depends on the spectrum of LET values in the radiation beam as well as the mean LET.

3.2.3. Therapeutic index and radiosensitizer

As with any other medical procedure, prescription of a course of radiotherapy must represent a balance between risks and benefits. The likelihood for a tumor to be controlled is called the tumor control probability (TCP), while the one for the healthy tissue side-effect is called normal tissue complication probability (NTCP) [72]. These probabilities are illustrated in Figure 3.11. One can see that the dose associated with tumor eradication is not very different from the dose associated with normal tissue complication development. The probability of cure without complication (PCWC) is given by equation:

$$PCWC = TCP\,(1 - NTCP) \tag{3.13}$$

The relative position and shape of the dose–response curves for tumour control and a given radiotherapy complication determine the possibility of delivering a sufficient dose with an acceptable level of side-effects. Hence, we may define the radiobiological concept of therapeutic index as the tumour response for a fixed level of normal-tissue damage. Therefore, improvements have been made over the past few decades to enlarge the differences between TCP and NTCP curves. One strategy involves the use of chemical localized into the tumor, which can increase cancer cell killing and move the TCP curve towards the left. Consequently, a significant increase in the maximum and width of the PCWC distribution generates a larger margin for the therapeutic window. These molecules are called “radiosensitizers” and enable to reach a given tumor cell killing using a reduced total dose delivered to the patient.

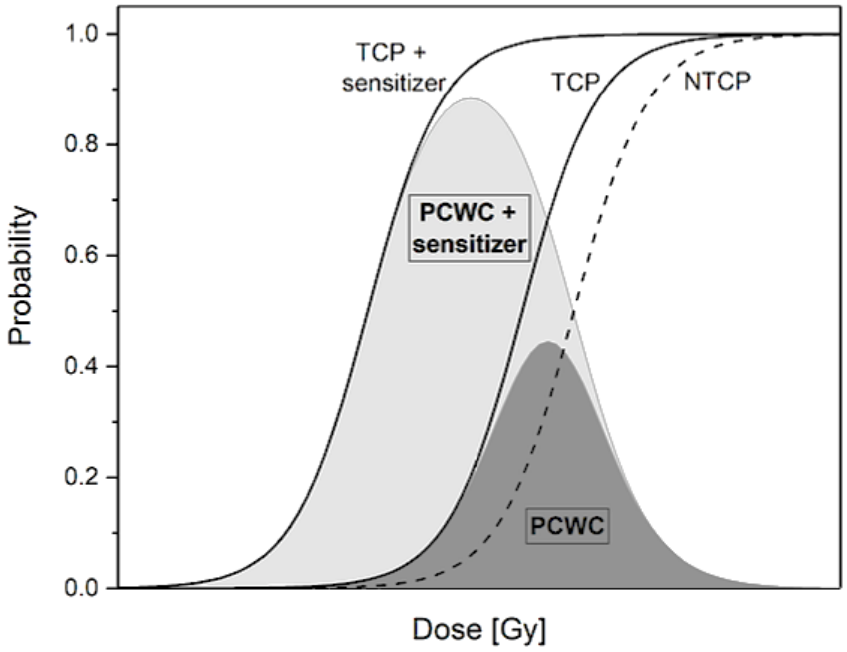

Figure 3.11. Schematic representation showing the action of tumor-targeted radiosensitizer on the probability of cure without complication (PCWC). The tumor control probability (TCP, solid line) and normal tissue complication probability (NTCP, dashed line) are shown as a function of the dose delivered to the patient. Two scenarios are illustrated with or without the use of a radiosensitizer and the associated PCWC is shown by the surface in each case.

3.3. **Radiosensibilization induced by metal based NPs**

The use of metal-based NPs to preferentially sensitize tumors to ionizing radiation has aroused great interest in radiotherapy, but to translate their preclinical potential into the clinic still remains a challenge. Radiosensitizers based on metal-based NPs have many interesting characteristics for the area of oncology. NPs have a high surface area to volume ratio which allows drugs and other therapeutic agents (eg, peptides, proteins, antibodies, even small molecules) to attach to their surface for further targeted treatment and combination therapy of tumors [73]–[77]. They have low permeability to normal tissue and may preferential deposit at tumor sites, due to their enhanced permeability and retention (EPR) effect [78]. As an imaging contrast agent, they can be used in disease diagnosis as well as biological imaging [79]–[89]. Therefore, metal-based NPs are currently undergoing preclinical development for various therapeutic and diagnostic applications. The main *in vitro* studies on metal-based NPs as radiosensitizers are briefly described in Table 3.1. From these studies,

three classes of mechanisms have been outlined: physical enhancement, chemical reactions and biological effects. Bellow we briefly review the current knowledge on mechanistic aspects of NP-assisted radiosensitization.

Considering that metal-based NPs have been extensively studied in the literature as radiosensitizers agents, an exceedingly small number really reach the stage of validation and clinical approval. So far, NBTXR3® (hafnium oxide nanoparticles, HfO_2NPs) is the only metal-based NP that has been approved for clinical use (European market in 2019) as a radiosensitizer agent [90], [91]. NBTXR3 is indicated for advanced soft tissue sarcoma radiotherapy treatments and is administred via tumor injection. Currently, there are three clinical trials on NBTXR3 and conventional radiotherapy for the treatment of inoperable recurrent Non-small Cell Lung Cancer (NCT04505267), pancreatic cancer (NCT04484909), and esophageal cancer (NCT04615013). The combination of NBTXR3 with brachytherapy or intensity modulated radiotherapy (IMRT) in patients with prostate cancer (NCT02805894), are also being studied. In addition, another study with metal-based NPs for enhancement of radiotherapy was able to achieve clinical trials. AGuIX , a gadolinium-based NP, is being investigated for the treatment of multiple brain metastases, in combination with whole brain radiation therapy (WBRT) (NCT02820454). There is also a study on the combination of AGuIX with radiation and cisplatin in patients with locally advanced cervical cancer (NCT03308604).

The difficulty in translating preclinical studies into clinical trials may be attributed to the number of variables that need to be investigated to control and optimize the effect. The reported studies have investigated different aspects, diverging in cell lines, NPs material and their respective coatings, incubated NP concentrations, incubation times, irradiation parameters, as well as the assays used to demonstrate the effects. There are also differences between research groups in both maintenance of cells and protocols assays. As consequence, experimental data on radiation enhancement levels produced by various NPs on different biological systems show a large variability. Results are far from being conclusive, and substantial controversy remains. Hence, despite the promising preclinical results of the NP-assisted radiosensitization, the exact mechanism of action in a biological system is still an enigma. One aspect is the optimal formulation of the NPs (especially surface functionalization) and its impact on pharmacokinetic properties in an in vivo system. There are also gaps in the knowledge

on the interaction of NPs with ionizing radiation and the subsequent biochemical and biological effect.

Table 3.1. Summarized main *in vitro* studies on metal-based NPs as radiosensitizers.

Year	NP design	Size (nm)	Cell line	Cell type	Radiation	Ref
2015	Gd_2O_3	35	CT26	Human colon carcinoma	50 keV X-ray 45 MeV proton	[92]
2016	PEG-Se PVP-Se	500 200	HeLa NIH3T3	Human cervical carcinoma Mouse embryonic fibroblast	X-ray	[93]
2016	ZnO	9	L929 HeLa PC3	Human fibroblast Human cervical cancer Human prostate cancer	60-70 keV X-ray 1.3 MeV γ-rays	[94]
2016	AuNP	1.9	MDA-MB-231	Human breast cancer	X-ray	[95]
2016	AuNP	16	HepG2	Human liver cancer	50 kVp X-rays	[96]
2017	AuNP AuNP@PEG AuNP-TAT	113-128	HeLa	Human cervical cancer	6 MV X-rays	[97]
2018	AuNP	150	HepG2	Human liver cancer	160 kVp X-rays	[98]
2018	Bi	46 56	4T1 HDF	Mouse breast cancer Human dermal fibroblast	115 kVp X-ray	[99]
2018	FePt FePt-Cy	3.3 26.4	H1975 A549	Human lung adenocarcinoma	204 kV X-ray	[100]
2018	AuNP	24	HT-29	Human colon cancer	18 MV X-rays	[101]
2019	Gd-ZnO	9.39	SKLC-6	Human lung carcinoma	6 MV X-ray	[102]
2019	$CaWO_4$@PEG- PLA $CaWO_4$@FOL-PEG-PLA	600-800	HN31	Human pharyngeal carcinoma	320 kVp X-ray	[103]
2019	Glutathione-Au	2.5	U87-MG	Human glioblastoma	50 kV X-ray	[104]
2019	Pt@PEG	50	H460	Human lung carcinoma	250 kVp X-ray	[105]
2019	Bi_2S_3@BSA Bi_2S_3@BSA-FA-CUR	78.9 170.9	4T1	Mouse breast cancer	X-ray	[106]
2020	$MgFe_2O_4$	8.2 - 14.9	MCF-7	Human breast cancer	6 MV X-ray	[107]
2020	Bi_2O_3	70	MCF-7	Human breast cancer	6 MV X-ray	[108]
2020	SPION PG-SPIONS	17.9	U87-MG	Human glioblastoma	6MV X-ray	[109]
2020	Bi_2S_3-MoS_2	90	L929	Murine fibroblast	160 keV X-ray	[110]
2020	TaO_x@PEG	107	4T1	Mouse breast cancer	225 kV X-ray	[111]
2020	AuNP	1.9	U87 MCF-7	Human glioblastoma Human breast cancer	6 MV X-rays	[112]

3.3.1. Physical enhancement

Originally, the rationale for using high-Z materials as radiosensitizers was based on differences in the energy absorption properties of metals compared to soft tissues (the photoelectric absorption cross section is proportional to $\approx Z^4$). By exploring the difference in atomic number between high-Z materials and organic tissue, a significantly larger dose will be deposit in the region of interest. This effect is translated into a significant higher local dose that is proportional to the NP weight percent in the medium. If we consider charged particles, the radiation-matter interaction changes. The nuclear contribution is negligible for protons at energies used in clinics (< 230 MeV) meaning that the energy loss is mainly driven by inelastic Coulomb collisions with the electrons. The stopping power for protons in gold is up to 10-fold higher when compared to water for a 200 MeV proton beam, for example.

Physical enhancement is difficult to verify experimentally due to technical issues. The most straightforward way to quantify should be through the measurement of LEE emission from NPs in the medium of interest. Few authors have sucssefully measured the LEE emission from GNPs in water [113] and dosimetric films [114], [115], but such experiments involve the use of complex indirect measurement using chemical or biological reactions.

3.3.1.1. Monte Carlo simulations

In addition to these indirect physical measurements, theoretical simulations can predict LEEs and Auger emission and the subsequent physical enhancement [116]–[125]. Detailed Monte Carlo (MC) simulations indicate that NPs modulate the dose mainly within the first 100 nm from the particle surface [126], where the effect can be very large due to the cascades of LEEs and Auger electrons from the ionized NPs atoms [23], [127]. In most cases, the energetic photo- or Compton electron has a very long range in the surrounding water volume. By contrast, the LEEs have much shorter ranges, and so deposit much more of their energy near the NP. As a consequence, the energy deposition decreases quickly as the distance from the NP increases [116], [128]. Due to this nanoscale nature of dose enhancement, more recent studies are considering microscopic dose distributions instead of classical macroscopic analyses to obtain information in the area close to the NP surface [49], [129].

In addition, radiation mass attenuation coefficient depends on the material thickness, meaning that the NP size has an impact. LEEs have even shorter ranges in high Z than in water — on the order of a few nanometers. Thus, while events that occur on the surface of the NP tend to emit the entire Auger electron spectrum, only highly energetic particles escape after events that occur within the NP volume. As a result, the LEEs that contribute to the dose increase come from events that occur within a thin layer of the nanoparticle's surface. The vast majority of lower energy secondary electrons are absorbed within the NP volume. This phenomenon is called self-absorption [125]. This indicates better physical performance for NPs of small size made of heavy elements (for elements lighter than Fe, the dose increase is expected to be negligible [130].

Furthermore, the MC simulations show that no increase in overall dose deposition would be expected using MV X-rays and protons. However, various *in vitro* studies have reported significant radiosensitization effects with both radiation qualities [16], [24], [63], [109], [116], [117], [119], [131]–[134]. Finally, the observed enhancement values are generally higher than the predicted ones for almost all *in vitro* experimental results. Thus, the radiosensitization effect induced by NPs must not be attributed exclusively to the physical enhancement.

3.3.2. Chemical mechanisms effect

In comparison to the physical and biological pathways of radiation enhancement by metal based NPs, chemical enhancement has not been extensively investigated. Despite the limited number of studies, findings to date suggest a significant influence on the radiolysis effects in biological systems, highlighting the importance of a chemical contribution to radiosensitization [135]. The main chemical effect contributing to the NP-induced radiosensitization, so far, is the production of ROS. In the literature, two main mechanisms by which NPs may enhance ROS generation are described. The first is based on the physical effect. The ionizing radiation interacting with NPs creates energetic charge-carrier pairs, known as hot carriers, which can diffuse through the NPs surface and cause the ejection of electrons from the surface at the nano/water interface [136], [137]. Since some LEEs have enough energy to ionize oxygen-based molecules surrounding NPs, they may lead to ROS formation.

The second mechanism involves catalytic processes. In contrast to the widely accepted notion that noble metals, such as gold, are chemically inert, an increasing number of studies have reported that the surface of NPs is electronically active and is capable of catalyzing chemical reactions [138]–[141]. NPs have a large surface/volume ratio and so a considerable amount of surface atoms are not fully coordinated. This leads to defects in their crystal structure, which results in reactive electron donating and accepting sites [135]. These sites may interact with reagents and/or stabilize reaction intermediates, leading to a decrease in reaction energy barriers. *In vitro* studies have confirmed that the catalysis by NPs occurs predominantly through the interaction of the surface with molecular oxygen, which facilitates the electron transfer mediated by the surface [77], [142]–[144]. For example, smaller size of NPs can trigger necrosis by oxidative stress and induce mitochondrial damages, which depends on their ability in an induction of enhanced ROS and oxidative stress after the radiation [145]. In the case of GNPs, it has been recognized that the radiosensitization is dependent on their surface chemistry [137].

In order to assess the different routes of ROS, most of the studies in the literature used fluorescent chemical probes [62]. Some authors reported that the addition of NPs to water led to an increase the hydroxyl radical (OH•) levels [20], [146] , which is considered the most harmful to cells. Other studies showed an increase in H_2O_2 [34], [147] as it has a longer half-life than other ROS species in cultured cells and therefore is a more convenient molecule to be detected. In addition, several ROS are converted to H_2O_2 within the cells. The relationship between particle size and ROS production was also evaluated, revealing that small NPs with larger surface area produced higher levels of ROS, further confirming the catalytic role of the NP surface [148]. Few authors described results that followed the same tendency to create ROS species after irradiation in the presence of NPs [149]–[152]. With regard to high LET radiation, even though some *in vitro* studies indicate radiosensitization assisted by NPs [153], [154], the production of radicals has not yet been quantified experimentally. Only the production of H_2 on the surface of ZrO_2 NPs irradiated with 5 MeV α particles was evaluated [155].

Taken together, these studies provided evidence that NPs chemically enhance the effects of radiation by catalyzing radical reactions, and increasing the production of ROS. These highly reactive free radicals ultimately lead to radiation-induced cell kill by causing a cascade of ionization, and fixation of radiation-induced damage.

Furthermore, chemical enhancement, as described herein, may also have biological consequences by exerting oxidative stress as a result of the elevated levels of intracellular ROS.

3.3.3. Biological effects

Based on the studies conducted to date, three main biological pathways for radiosensitization have been identified: (1) Oxidative stress, and mitochondrial dysfunction, (2) interruption of the cell cycle and (3) inhibition of DNA repair [14]. The biological contribution to radiosensitization is strongly dependent on the parameters of the particles; and therefore, the exact mechanism by which cells respond to biological stress exerted by NPs has yet to be determined.

Most studies in the literature have investigated the impact of NP combined with radiation on DNA damage and repair mechanisms. Several authors reported higher DSBs numbers when cells were irradiated in the presence of metal-based NPs [95], [156]–[159]. Overall, the increase in DSBs in cells with internalized NPs was consistent with the clonogenic radiation cell survival *in vitr*o. Due to the short-range effect of NPs it is often assumed that NPs need to be placed close to the DNA (within the cell nucleus) to induce DNA damage. But the vast majority of metal-based NPs have shown endo/lysosomal entrapment of NPs in the cytosol, restricting nuclear entry [25]. Thus, it has been proposed that enhanced DNA damage is due to an increase in ROS production, and consequently indirect DNA damage [160], [161].

Although some groups attribut the higher post-IR RIF level to a higher DNA damage induction caused by physical and chemical enhancement, the reality seems to be more complex. In fact, some studies [162], [163] did not observe any significant difference in DNA damage post-irradiation, suggesting that NPs did not increase the amount of DSB produced by the irradiation. Despite these studies indicate that the presence of NPs did not influence the total number of DSBs per cell, they observed a decrease in the repair process rate. Therefore, DNA repair inhibition seems to be another biological mechanism of NP radiosensitization.

As we can see, there is currently no consensus in the literature on the specific role of NPs in the process of DNA damage repair. Some of these studies were performed with doses ranging from 2 to 6 Gy, which correspond to a range where RIF-dose relationship reachs a saturation indicating multiple DSB coalescence into single

RIF. Unfortunately, the loss of relationship between DSB and RIF prevents a clear understanding of these results. Although other groups worked in the linear RIF-dose range, they investigated NP impact on DNA repair by analyzing the RIF number at only one or two time-points post-IR [95]. This approach only offers a static view of a dynamic process lasting several hours. Therefore, it is still complex to conclude if the higher RIF number reported after irradiation in cells incubated with NPs is due to DNA repair delay or to a higher level of persistent DSBs.

In addition to their indirect effects on DNA, like base oxidation, ROS also affect other biomolecules. Due to ROS chemical instability, they are capable of interacting with several types of biological molecules leading to severe damages to cellular components [164], [165]. Lipid peroxidation is one of the primary consequence of a cellular oxidative stress [166]. In addition, plasma membrane phospholipids and organelle membranes such as the mitochondria can be oxidized, leading to biophysical changes that disturb membrane and organelle function [164], [165]. Along this line, several author appoint the impairment mitochondrial function as a consequence of elevated intracellular ROS to be the mains mechanism to trigger oxidative stress [143], [159], [167]–[170].

It has also been reported that high-Z NPs can induce radiosensitization through cell cycle arrest, despite some studies did not evidence any significant change in cell cycle distribution [171]. The large majority reported a G2/M phase arrest coupled to a G0/G1 or S phase acceleration [145], [172] or an increase in the sub-G1 population [173][174]. Zhang et al. [175] reported that GNPs were able to induce cell cycle arrest in the G2/M phase and promoted cell apoptosis under 6 MV radiation. Also, Roa et al. [176] reported that glucose capped GNPs could accelerate the G0/G1 progression resulting in accumulation of cells in the G2/M phase and enhanced radiation sensitivity in the radiation-resistant prostate cancer cell line. Li et al [105] demonstrated that platinum NPs (PtNPs) could enhance radiosensitivity through cycle arrest under radiotherapy conditions. The PtNPs themselves had no effect on cell cycle distribution, but significantly enhanced radiation-induced G2/M arrest when the cells received combined treatment with PtNPs and X-ray irradiation. Despite increasing evidence that metal-based NPs can induce cell cycle arrest under radiotherapy conditions, it is still not possible to draw conclusions about it due to the lack of data regarding biological mechanisms and the great variability in experimental conditions used in the studies.

4. METHODS

4.1. Synthesis and characterization of nanoparticles

4.1.1. Synthesis

GNPs (GNP-naked) were synthesed by adapting Deraedt et al [177] method, which is based on the reduction of chlorouric acid ($HAuCl_4.3H_2O$) by sodium boron hydride ($NaBH_4$). 30 mL of a 0.1 mM chlorouric acid solution was added to a 50 mL reaction flask and kept under constant stirring at room temperature. After 20 minutes of stirring, 10 mL of $NaBH_4$ solution with a concentration of 7.9 mM was added to the solution. At the time of addition, the solution changed to a light pink color, indicating the formation of NPs. Stirring was continued for additional 5 min. After synthesis, the nanoparticles were washed with deionized water and collected by centrifugation in Amicon tubes, to concentrate the dispersion. This centrifugation process continued until the final volume of the solution reaches ~ 5 mL.

Dextran-coated superparamegnetic iron oxide nanoparticles (SPION-DX) were prepared according to Oliveira et al. [178]. Briefly, $FeCl_3.6H_2O$ was added to ice-cold dextran solution (0.9 mmol) in constant magnetic stirring for 30minutes, under N_2 atmosphere. Then, the $FeCl_2.4H_2O$ was added to the mixture, which was inserted in a reflux system. A volume of 10mL of cooled NH_4OH was added to the mixture and the reaction was conducted at 80ºC for 1.5h. The NPs were centrifuged in Amicon tubes (50k MWCO) to remove the remaining free dextran. Afterwards, an additional crosslinking step of the dextran shell was performed by adding 5 M NaOH and14 mL of epichlorohydrin into the solution, under magnetic stirring for 10h. Finally, for the amination of the coating, 60 mL of NH_4OH (28%) was added to the solution and maintained under magnetic stirring for 24h. The ammonia excess was extracted by dialysis, using Spectra/Pro® membranes and changing the deionized water every 30 minutes. At the end, both NPs (GNPs and SPION-DX) were centrifuged in Amicon

tubes (50k MWCO) for 15 minutes and washed several times to eliminate undesired residues. The SPION-DX was kept in a sodium citrate buffer solution and both final solutions were stored in a refrigerator at 4ºC.

The GNP coated with PEG (GNP@PEG) were provided by Professor Mateus Borba Cardoso's research group, from the National Nanotechnology Laboratory (LNNano).

4.1.2. Transmission electron microscopy (TEM)

The analysis of the size distribution and morphology of NPs were performed using a transmission electron microscope, model Tecnai G2 T20 - FEI, located at the Central Laboratory of Microscopy and Microanalysis (LabCEMM), PUCRS. The NPs were dripped onto carbon film TEM grids and left to dry at room temperature. The grids were kept in vacuum for at least 24 h before TEM analysis. The average diameter of the NPs was measured using the ImageJ software.

4.1.3. Dynamic light scattering (DLS)

The measurements of the hydrodynamic diameter and the zeta potential of the dispersed NPs were performed in a Zetasizer, model ZEN3600 – Malvern at room temperature (~25 °C). Ultra-pure deionized water was added to the analysis cuvettes and the colloidal NP system was dripped into deionized water, in order to dilute the colloidal system by 100 times.

4.2. **In vitro assays**

The *in vitro* assays were performed with U87 and M059J human GBM cells (ATCC, USA), the first one characterized as radioresistant and the second as radiosensitive. The assays were carried out in the facilities of the Applied Pharmacology Laboratory – PUCRS and of the department of Biological Sciences of Cells and Systems (BSCS) of the University Medical Center Groningen (UMCG).

4.2.1. Cell cultivation and NPs treatment

The cells were cultivated in Dulbecco-modified Eagle Medium (DMEM), supplemented with 10% fetal bovine serum (FBS). The cultures were kept in a humidified cell incubator under ideal culture conditions (37ºC, 5% CO2, 95% humidity). The cells were incubated for 24 hours with GNP-naked, GNP@PEG and SPION-DX, dispersed in the DMEM 10% FBS at concentrations of 20, 50 and 100 μg/mL.

4.2.2. Cell viability assay

The MTT reduction assay (3-4,5-dimethyl-thiazol-2-yl-2,5-diphenyltetrazolium bromide) is a rapid method, often used to measure cell proliferation and cytotoxicity. The assay is based on the reduction of MTT during cellular metabolic activity, forming insoluble formazan crystals, which are blue or purple. The reduction of MTT to formazan is directly proportional to mitochondrial activity and cell viability.

To perform the test, the cells were collected from a culture bottle (stock) by means of trypsinization: the culture medium is removed, and the cells are washed once with PBS (Phosphate-Buffered Saline). The PBS is removed and replaced with trypsin, an enzyme that degrades adhesion proteins, causing detachment of the cells from the flask. After trypsinization, the cells are resuspended in the culture medium and counted in the Neubauer chamber with the help of trypan blue. Then, the cells were plated in 96-well plates, at a concentration of 3,000 cells / well. The plates were incubated in the CO_2 oven for 24 hours. After that, the culture medium was removed and the cells were treated with NPs diluted in the culture medium, in concentrations ranging between 0.01 mM and 1 mM. The plates were again placed in the CO_2 incubator. After 24 hours, the culture medium was removed, and the wells were washed twice with sterile PBS. 100

µl of the MTT solution in PBS (0.5mg / mL) was added to all wells and the plates were incubated for 2 hours. The MTT solution was removed from the plates and 100 µl of pure DMSO was added. Cell viability was quantified by measuring the average the absorbance at 490 nm (Spectra Max M2e, Soft Max® Pro 5, Molecular Devices).

4.2.3. Nanoparticle internalization

4.2.3.1. Intracellular localization of nanoparticles by TEM

The internalization of NPs by cells was evaluated by transmission electron microscopy (TEM). The cells were treated with NPs for 24h. Subsequently, the cells were centrifuged to form a pellet. Fixation was done with a solution containing 2.5% glutaraldehyde, 2% parafolmadeide and phosphate buffer. After fixing, the samples were washed three times with 0.1 M phosphate for 30 min. Post-fixation was done with Osmium tetroxide and 0.2 M phosphate buffer for 45 min and washed again. Then, the samples were dehydrated with acetone and soaked in resin for 24 hours. The cells already embedded in pure resin were left in the oven at a constant temperature of 60 °C for 72 hours. Finally, the samples were cut by ultramicrotomy into 100 nm slices and placed in TEM grids. The images were acquired in a FEI Tecnai G2 T20 microscope.

4.2.3.2. Elemental cellular uptake by ICP-MS

Cellular uptake of nanoparticles determined using Inductively coupled plasma mass spectrometry (ICP-MS) (modelo Agilent-2012). U87 and M059J cells were seeded in 12-well plates and treated with NPs at 20, 50 and 100 μg/mL concentrations. Following the incubation period of 24 hours, the NP solution was removed, and wells were gently washed twice with PBS. Cells were trypsinized and counted using trypan blue to determine the total number of cells per sample. The cell suspension was centrifuged for 15 min at 1000 RPM. Pellets were then dissolved by aqua regia (three parts hydrochloric acid to one-part nitric acid) and the solution was diluted with ultrapure water. Reference measurements were initially carried out on a known concentration of each NP type, to obtain a reference curve relating the counts per second to the NP concentration. Each sample was then processed, and counts were

related to the reference curve to determine the elemental concentration of each material per sample. Results were then reported as the mass of NP element per cell (pg per cell).

4.2.4. Clonogenic assay

Immediately after irradiation the cells were collected by trypsinization and resuspended in 3 ml of culture medium. The number of cells in the resulting suspension was counted with the help of trypan blue and a Neubauer chamber, in order to establish the appropriate volume to be pipetted into 6 cm diameter test plates (dishes). The quantity of cells pipetted varied from 100 to 10^4 cells / dish, depending on the irradiation dose and cell line, according to Table 4.1. As M059J cells are radiosensitive, the seeding values had to be increased, to allow the formation of colonies.

Table 4.1. Number of cells seeded per dish according to the irradiation dose and cell line.

Dose (Gy)	0	1	2	4	6	8
U87	100	100	200	500	1.000	10.000
M059J	200	500	1.000	1.000	10.000	10.000

The dishes were kept in the incubator for 13-15 days, to allow the cells to form sufficiently large colonies. In order to reveal the colonies, the cells were stained with crystal violet: The medium was removed and the dye was added so that it covered the entire bottom of the dish (around 3 ml). Then, the crystal violet was removed and the dishes washed with water. After washing the dishes were left to dry at room temperature. Figure 4.1 summarizes the different steps of the clonogenic assay.

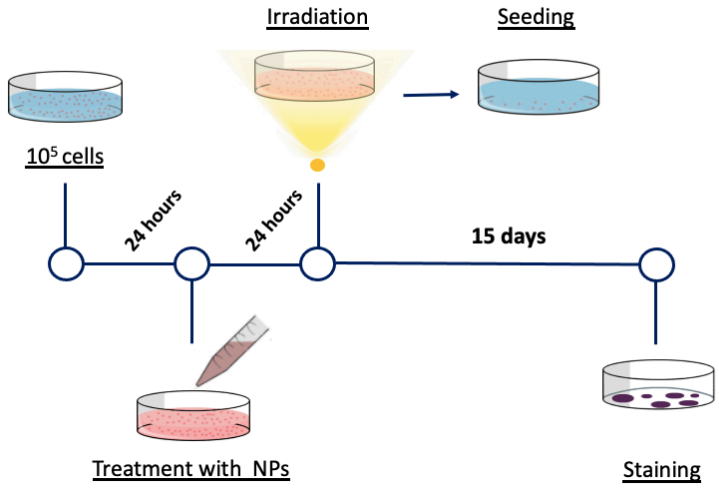

Figure 4.1. Summary of the different steps taken to perform the clonogenic assay,consisted of cell seeding prior to radiation, incubation of the cells with NPs for 24 hours, irradiation, seeding in culture dishes and colony staining.

Colonies with more than 50 cells were counted. All experiments were normalized for plating efficiency of control samples (0 Gy). The SF curves were obtained and fitted to the LQ model to extract the α and β parameters.The sensitization enhancement ratio at a 10% survival ($SER_{10\%}$) was extracted to quantify the effectiveness of the NPs in reducing cell survival after irradiation:

$$SER_{10\%} = \frac{Dose\ at\ 10\%\ survival\ without\ NPs\ (D_{control})}{Dose\ at\ 10\%\ survival\ with\ NPs\ (D_{NP})} \quad (4.1)$$

4.2.5. DNA damage and repair (Immunofluorescence assay)

For this analysis, circular glasses with an approximate diameter of 1.5 cm (cover slips) were placed at the bottom of the wells before the cells were plated. The cells were incubated with NPs for 24 hours and irradiated with gamma and proton beams. The cells were then fixed in different periods of time after irradiation (15 min, 2h, 6h and 24h). with 4% PFA in PBS for 10 min at room temperature. Santa Cruz antibodies (mouse-anti-H2AX and rabbit-anti-53BP1) were used as primary antibodies and the Alexa Fluor antibodies from Life technologies (goat-anti-mouse-488-green and goat-anti-rabbit-594- red) as secondary antibodies. The cells were permeabilized using 0.2% Triton for 5 min. The wells were filled with 200 μL of a diluted (1: 500) solution of

the primary antibodies in blocking solution (2% BSA in PBS). After 1 hour, the primary antibody solution was removed and the secondary antibodies diluted to a concentration of 1: 1,000 in BSA blocking solution were added and maintained for an additional 1 hour. From this step onwards, the samples were kept in the dark. The secondary antibody solution was removed and DAPI was added for 12 minutes. The coverslips were mounted with the DAKO mounting solution and fixed with enamel. Between each step, the samples were washed 3 times with PBS. To visualize the formation of foci, an Leica DM 4000B fluorescence microscope was used. The average number of foci per cell and the number of cells that showed foci were counted.

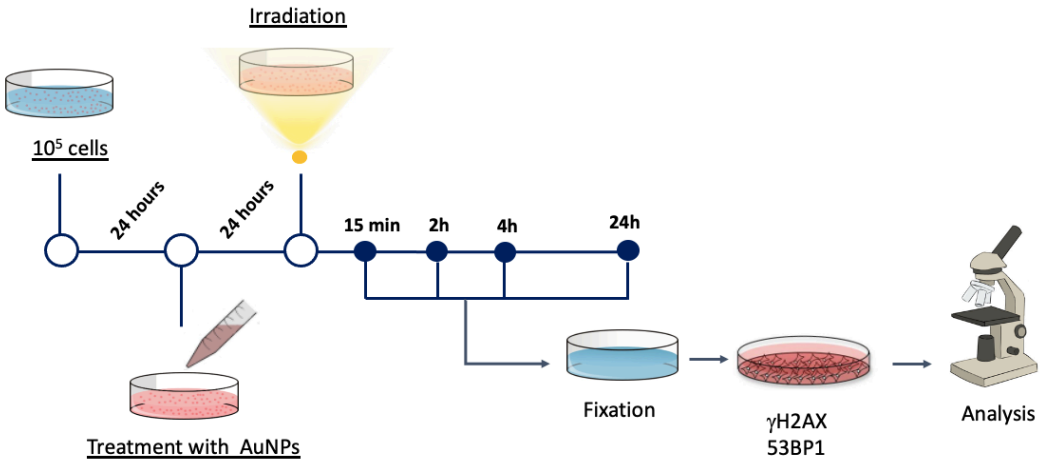

Figure 4.2. Summary of the different steps taken to perform the immunofluorescence assay: 1st cell seeding prior to radiation, 2nd incubation of the cells with NPs for 24 hours, 3rd irradiation, 4th cell fixation at specific time points, 5th antibody staining, and 6th analysis.

4.2.6. Nuclear Morphometric Analysis (NMA)

In addition to DNA damage and repair studies, immunofluorescence images of DAPI-labeled nuclei were also used to perform the nuclear morphometric analysis (NMA) [179]. NMA is an image analysis tool able to indicate the proportion of cells in senescence, apoptosis or with nuclear irregularities in a cell population *in vitro* based on nuclear morphology. The NII Plugin of the Image J Software was used to extract the morphometric information about nuclei from the DAPI immunofluorescence images. The contours of the cores were individually delimited with the "magic wand" tool, preventing excessive or wrong marks from occurring. The measures of nuclear area and of four parameters of irregularity, named Aspect, Area/Box, Radius Ratio and Roundness were extracted. These four parameters are used to generate a Nuclear

Irregularity Index (NII) which, added to area measurement, classify the nuclei in normal (N), irregular (I), small and regular (SR), small (S), small and irregular (SI), large and regular) or large and irregular (LR). Results were plotted as the nuclei area as a function of the NII.

4.2.7. Irradiation

Prior to irradiation, the cells were plated (12-well plates) at 10^5 cells / well and treated with NPs in culture medium, according to the protocol described in the previous sections. The plates were incubated with the NPs for 24 hours. After the incubation period, the cells were exposed to different beams of ionizing radiation at doses of 0, 1, 2, 4, 6 and 8 Gy. In the case of protons, doses were up to 6 Gy. For each irradiation experiment, an untreated group was transported to the irradiation site, as a control group. All irradiations were performed with 70 - 80% of confluent cells.

4.2.7.1. 662 keV gamma-rays

The irradiations with gamma-rays of 662 keV were carried out at UMCG in the BSCS department, with a ^{137}Cs source (IBL 637 Cesium-137 γ-ray machine). Figure 4.3 A shows a photograph of the irradiation equipment. The ^{137}Cs source is formed by four sealed stainless-steel tubes that contain the radioactive material. At the time of irradiation, the source is 25 cm from the base of the chamber and is kept in an armored compartment. The equipment has a cubic irradiation chamber (40 cm of edge to edge) divided into 4 levels, depending to the distance in relation to the source (Figure 43 B). The dose rate is measured for each level, and the irradiation dose is controlled by the exposure time. Due to the ^{137}Cs decay, the dose rate and irradiation times are updated annually by the BSCS.

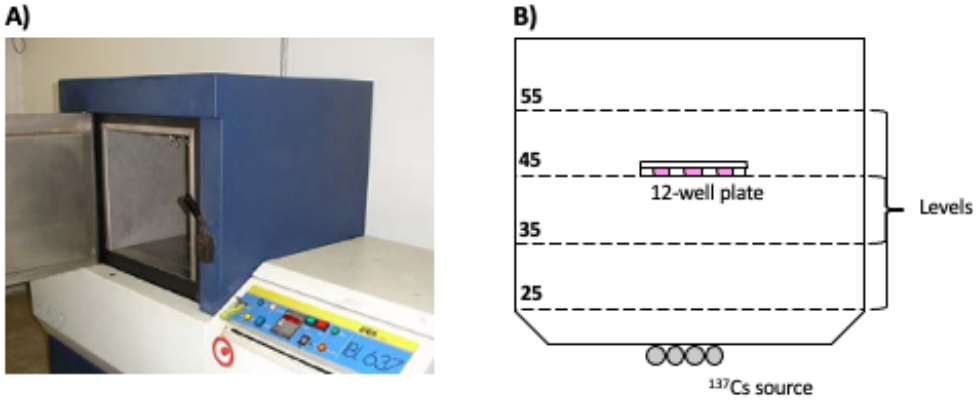

Figure 4.3. A) IBL 637 Cesium-137 γ-ray machine. B) Representation of the interior of the irradiation chamber, representing the levels of irradiation, the source of ^{137}Cs and the position of the 12-well plate.

The irradiations were performed following the BSCS protocol. The plates were positioned in the center of level 45, where the irradiation region is delimited by a circle with a diameter of around 10 cm and the dose rate is 9,445 mGy/s. The exposure time was fixed on the equipment, according to the pre-established values and is controlled by a shutter in front of the source.

4.2.7.1. 6 MV Clinical Accelerator

X-ray irradiations were performed in the Radiotherapy Center of Hospital São Lucas at PUCRS in a 6 MV linear accelerator (Clinac IX and Clinac Trilogy by Varian), which are standard in radiotherapy services.

To perform the irradiations, we developed an acrylic phantom of 30cm X 30cm with a slot for the culture plates in the central region (Figure 4.4 A-C). The phantom was made so that the plate can be easily removed, but still minimizing the volume of air between the plate and the walls of the phantom. In addition, a 3 cm solid water bolus was placed under the phantom/plate system to simulate backscattered radiation. Another layer of 5 cm of solid water is positioned between the plate and the exit of the X-ray beam for build-up.

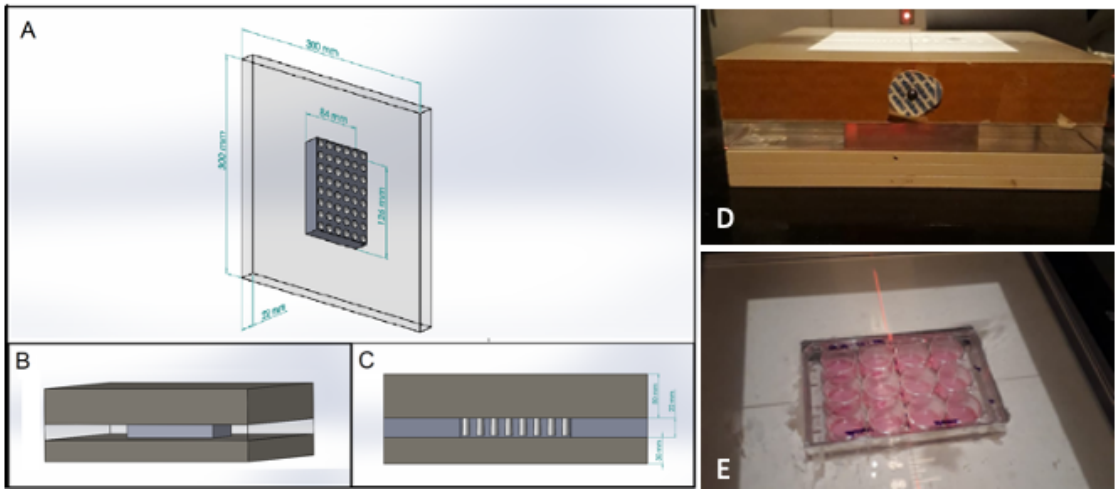

Figure 4.4. A – C) Sheme of the acrylic phantom constructed for the irradiation of cell culture plates. D The phantom-plate system is positioned between two boluses of solid water of 3 cm and 5 cm are positioned below and above the phantom, respectively. E – 12 well culture plate inside the phantom.

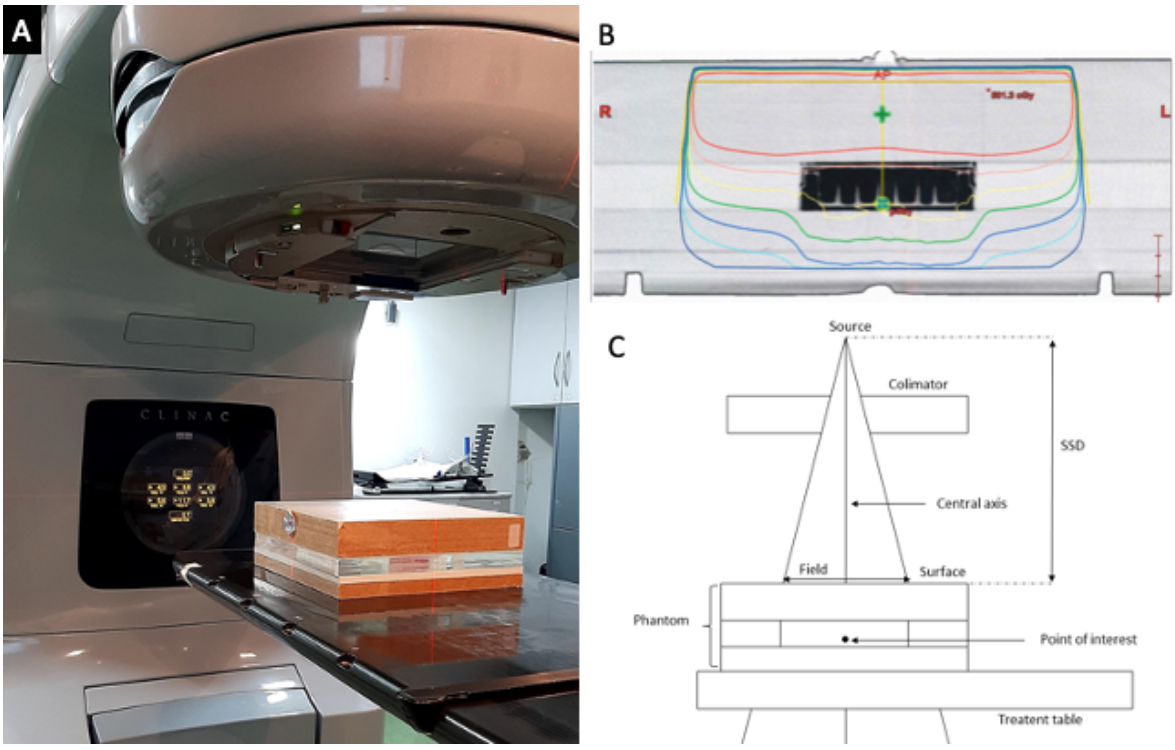

Figure 4.5. A) Set up irradiation at radiotherapy center, Hospital São Lucas da PUCRS. The phantom is placed in the 6 MV Linac accelerator. B) Transverse tomographic image of the phantom, where the colored lines represent isodose curves and the isocenter was placed at the same position where the culture plates would be placed. The colored lines represent the isodose curves. C – Representative figure of the irradiation set up. The “x” in the center defines the region of interest, which coincides with the isocenter. Irradiation field 20 x 20 cm and source to surface distance (SSD) of 93 cm is represented.

The symmetry and flatness tests of the beam and the absorbed dose in the isocenter region were performed with the help of the medical physics team at the hospital. The irradiation planning was done based on tomographic images of the phantom, using the three-dimensional planning software Eclipse, Figure 4.5B. The coloured lines represent the isodose curves and the central region was placed at the same position where the cell culture plate would be placed. The irradiations were carried out with a 20 X 20 cm field and a 93 cm SSD (source to surface distance). The size of the field was chosen so that the isodose curves were as uniform as possible in the region of interest.

4.2.7.1. Proton irradiations

Proton beam irradiation was carried out at the KVI-Center for advanced radiation technology (KVI-CART), Groningen. Figure 4.6a shows a scheme of the irradiation line. The charged particles are extracted from the cyclotron to the irradiation line and after traversing a collimator system (about 3 m of air), it reaches the sample position on the XY table. The irradiation field had a diameter of 70 mm and homogeneity of ± 3%.

The irradiations were performed following the KVI pre-established protocol. After incubating the cells with the NPs, the wells of the culture plates were filled with DMEM 10% FBS medium. The wells were sealed with parafilm, preventing the culture medium from leaking. The culture plates were positioned vertically with the side to which the cells are attached facing the exit of the proton beam. The protons were extracted out at 150 MeV/u with a fluence of 10^9 protons / cm^2. The dose delivered to the cells was controlled by the exposure time, which were pre-set according to the irradiation protocol. After irradiation, it was necessary to wait a little more than 2 hours, as the samples became radioactive and to handle them it was necessary to wait for the activity to fall to safe levels

a)

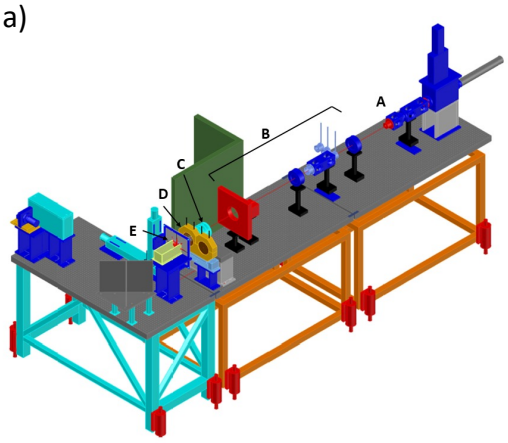

b)

Figure 4.6. Beam line diagram KVI-CART. A - beam exit. B - collimator system. C - energy degrader. D - double collimator. E - XY table where the samples are placed. b) Culture plates are placed vertically in front of the beam, in position E. The side which the cells are adhered to faces the exit of the beam.

5. RESULTS AND DISCUSSION

5.1. Nanoparticles characteristics

The TEM images revealed SPION-DX with approximately spherical shape and mean diameters around 5.1 ± 1.7nm (Fig. 5.1 a). This roughly corresponds to the size of the iron oxide core, as the organic coatings are not identifiable in the TEM images. GNPs showed a rounded shape with diameters of 5.9 ± 2 nm and 6.2 ± 1.3 nm, for GNP-naked and GNP@PEG, respectively (Figure 5.1 b and c). The mean hydrodynamic diameters of the NPs in ultrapure water dispersions are displayed in Table 5.1. The mean values are larger than the physical sizes measured by TEM, as expected. The zeta potential (ζ), which indicates the surface charge, of the different NPs dispersed in ultra-pure water is also given in Table 5.1.

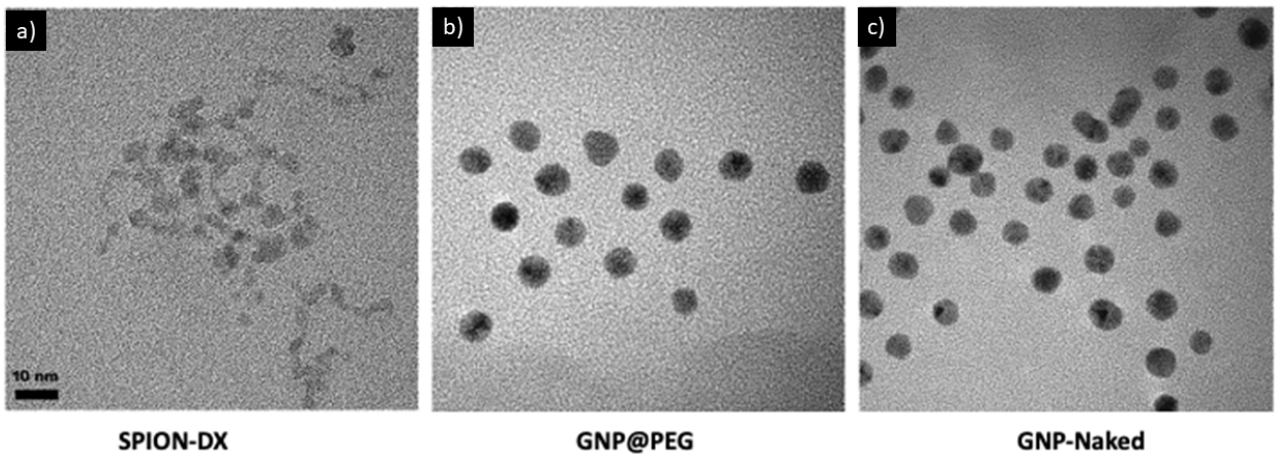

Figure 5.1.TEM images of a) SPION-DX, b) GNP@PEG and c) GNP-naked. The scale bar represents 10 nm.

Table 5.1. Average TEM (D) and hydrodynamic (D_h) diameters, and zeta potential (ζ) of the NPs. TEM data were obtained from direct counting of individuals particles. Hydrodynamic diameters and zeta potential were obtained from DLS measurements of NPs dispersions in ultrapure water.

Nanoparticle	D (nm)	D_h (nm)	ζ (mV)
GNP-naked	5.9 ± 2	31.8 ± 0.6	-18.8 ± 0.7
GNP@PEG	6.2 ± 1.3	27.2 ± 1.1	-15.3 ± 0.6
SPION-DX	5.1 ± 1.7	22.0 ± 1.4	+11.6 ± 0.3

5.2. **Quantification of cell uptake and intracellular distribution**

To investigate whether NPs were internalized by cells and to determine their intracellular location, U87 and M059J GBM cells were incubated with different concentrations of well dispersed GNPs and SPION-DX for 24h. Cellular uptake was quantified by ICP-MS and the intracellular localization was analysed by TEM. U87 and M059J cell lines represent two different GBM types, where differences in cellular uptake and radiation response are expected.

Differences in cellular uptake were observed between cell lines and NP treatments, as shown in Figure 5.2. The uptake of GNPs was shown to be proportional to the treatment concentration, where the uptake increases with increasing concentration. This was observed for both U87 and M059J cell lines. In the case of SPION-DX, the uptake of NPs was dependent on the cell line considered. Significant differences in uptake were seen for U87 cells exposed to different concentrations. For M059J cells no significant difference in cellular uptake was seen. For U87 cells, despite no significant difference was observed between 50 and 100 μg/mL, both treatments led to a higher internalization compared to the lowest concentration of 20 μg/mL. This result suggests a saturation in the internalization capacity of the cells. Overall, the uptake was higher for SPION-DX NPs than for the GNP-naked ones, except at 100 μg/mL, where no difference was observed.

When comparing uptake between cell lines, for GNP-naked the uptake was similar, except at 100 μg/mL ($p^{***} = 0.0002$), for which internalization was higher for U87 cells. For SPION-DX, U87 cells showed a considerably higher uptake than M059J cells ($p^{*} = 0.0120$ for 20 μg/mL, and $p^{**} = 0.0011$ for 50 and 100 μg/mL).

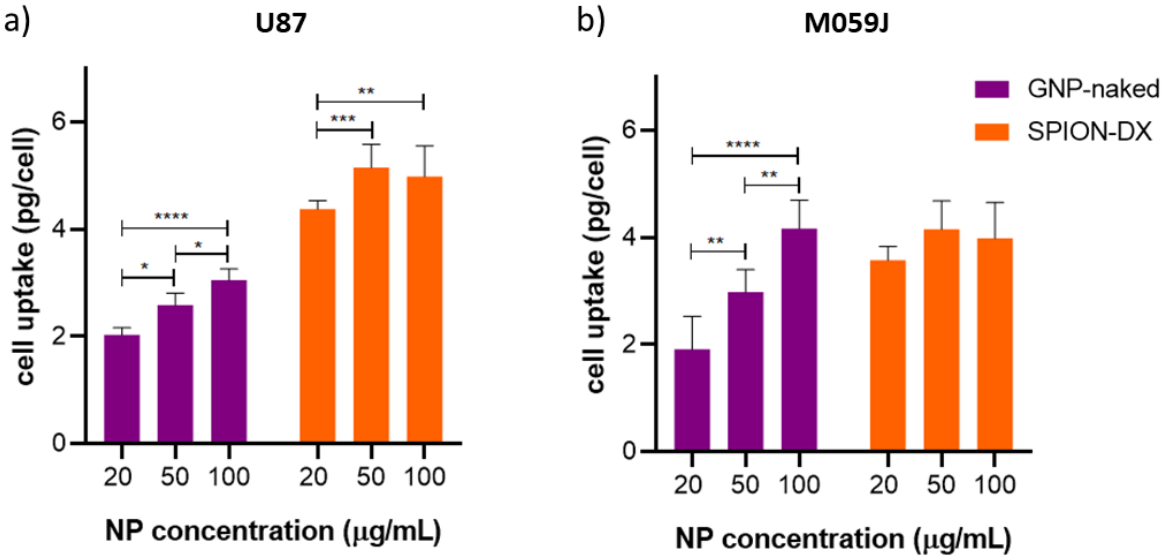

Figure 5.2. Uptake measurements determined using mass-spectrometry (ICP-MS), for a) U87 and b) M059J incubated for 24 hours with different concentrations of GNP-naked and SPION-DX nanoparticles. The results are presented as pg of gold and iron oxide per cell. P-values are presented as: * p<0.05; ** p<0.01; *** p<0.001; **** p<0.0001.

As shown in Figure 5.3, NPs were localized within the cytoplasm in a very heterogeneous distribution. No particles were found inside the nucleus. Magnified TEM images show that NPs are present as aggregates on the order of hundred nanometres which may or not be within vesicles. We also observed few isolated NPs dispersed within the cells. In addition to the intracellular localization of the NPs, the analyses showed that the exposure to NPs did not alter the cell morphology.

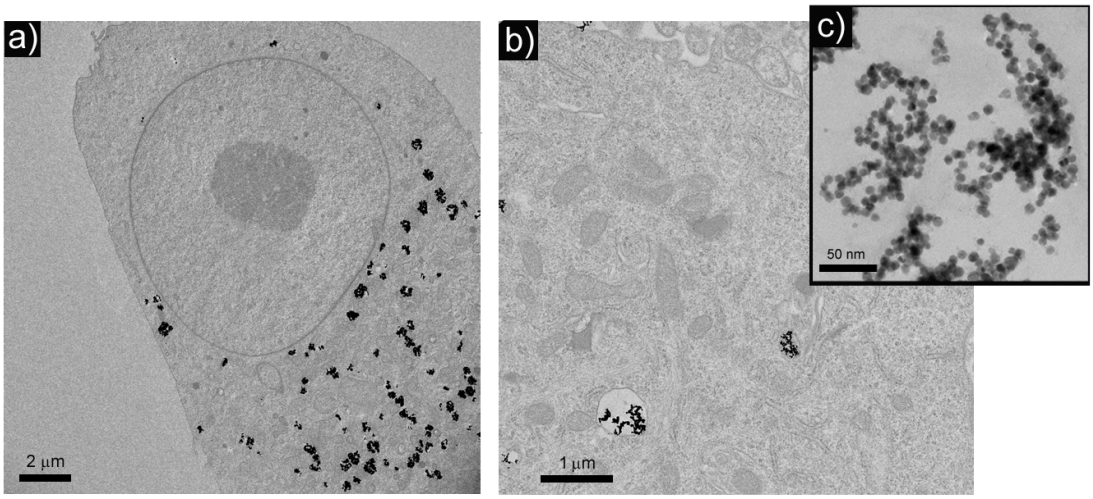

Figure 5.3. TEM micrographs of U87 cells exposed to 50 μg/mL GNP-naked showing a) NPs (black spots) localized within the cytoplasm, while none was found within the nucleus. b) Magnified TEM image from the same cell, showing the NPs within vesicle c) in aggregates.

It has been shown in the literature that depending on the cell type, differences in NP uptake can occur due to characteristics of the microenvironment, affecting NPs internalized within the cell [180]. Other factors such as the surface-to-volume ratio can affect uptake, as a larger ratio increases the probability of interacting with cellular receptors for uptake [181], [182]. Differences in uptake across cell lines were demonstrated by Dos Santos et al.[182] , where they investigated the level of uptake in five different cell lines, with negatively charged carboxylate poly-styrene (PS–COOH) NPs.

Previous work also reported the tendency of metal-based NPs to form aggregates when they are internalized by cells, usually in endo/lysosomal entrapment, restricting nuclear entry[171], [183]–[186]. Due to their size, NP uptake can follow the same internalization routes as biological molecules, such as proteins, viruses, or DNA. As a rule, the cellular transport of macromolecules occurs via endocytosis pathways [183], [186]. In addition, isolated NPs can be internalized through the cell membrane by passive diffusion and gradually be clustered, as they are transported by endosomes [186].

5.3. **Nanoparticles cytotoxicity**

Cytotoxicity of NPs in the absence of radiation was first evaluated through MTT assay. This is important to establish the background level of toxicity associated with exposure to the NPs alone. As it can be seen in Figure 5.4, for all concentrations considered, cell viability remained greater than 90% in all groups treated with NPs, with no statistically different viability levels evidenced.

Several reports have shown negligible levels of toxicity of metal-based NPs in different cell lines [24], as in our study. However, other works such as Xia et al. [187] reported a significant genotoxic potential of commercially available 5 nm GNPs. The authors observed a dose-dependent increment in DNA damage in HepG2 human liver carcinoma cells when incubated with 5nm GNPs for 24 hours. Such divergence may be attributed to the type of cell line under investigation. Factors such as cell uptake and cellular response to drugs or external agents are strongly dependent on cell type and are directly related to NP-induced toxicity. Specifically, the biocompatibility of GBM cells to GNPs and SPION have previously been reported [24], [109], [112]. In a recent study, Ahmmad et al.[112] assessd the effect of a 24h exposure to three different

commercial NPs (AuNP aurovist, AguiX and SPIONs) in U87 GBM and MCF-7 (human breast cancer) cells. For both concentrations considered (0.2 and 0.5 mg/mL), all three NPs had no impact on the cells viability for either cell line. In another study, Jafari et al. [109] evaluated the cytotoxicity of SPIONs coated with PEG (PG-SPIONs) or not in U87 GBM cells. The cells were incubated with different concentrations of NPs including 5, 25, 50,100 and 200 µg/ml for 24, 48 and 72 hours. For uncoated SPIONs, cells viability significantly decreases at concentrations above 100 µg/ml in all times, but it does not differ for PG-SPIONs. At lower concentrations, NPs did not affect cell viability. The authors attributed uncoated SPIONs cytotoxicity to formation of ROS, such as H_2O_2 and anion superoxides (O^{2-}), which in turn causes oxidative stress and toxicity to the cells. The organic coating would prevent such reactions, which would decrease the citoxicity of NPs.

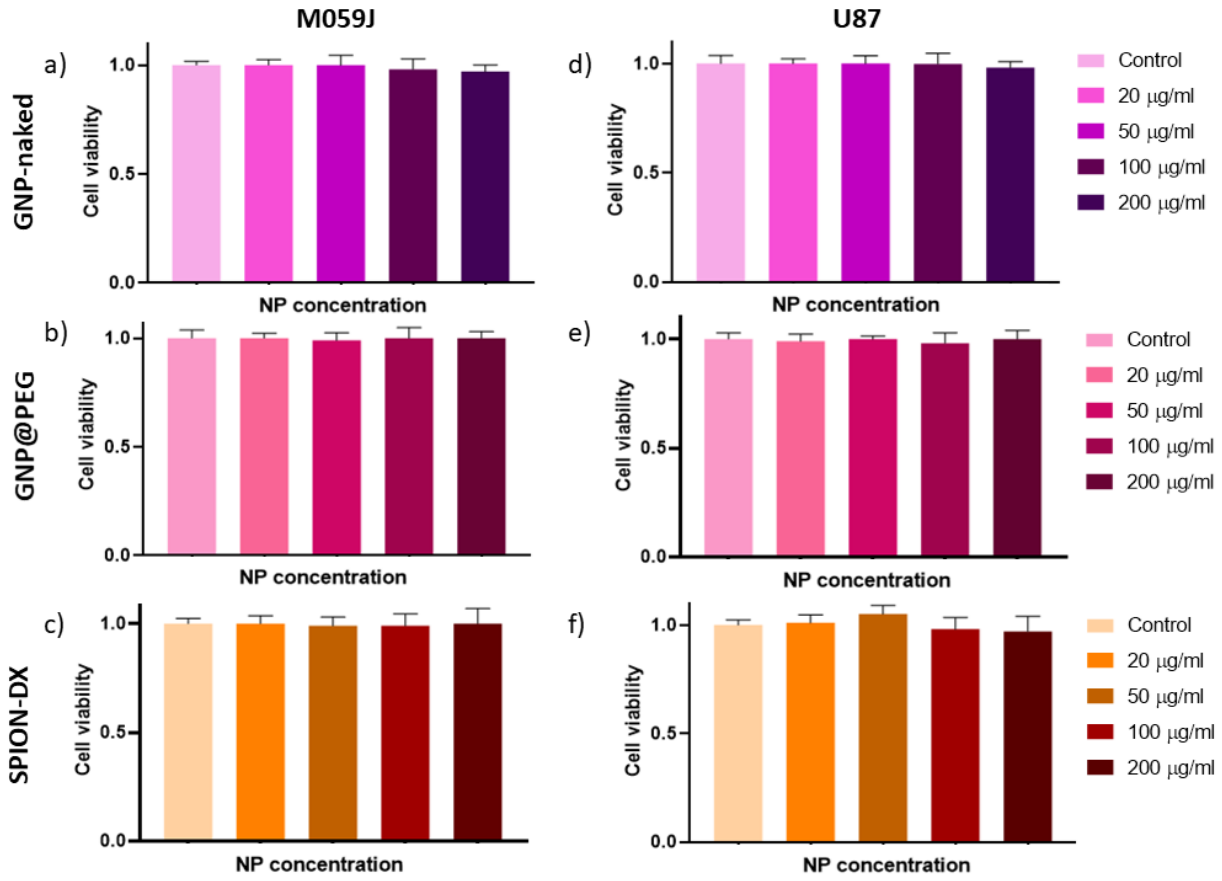

Figure 5.4. MTT cell viability assay for a - c) M059J and, d) - f) U87 GBM cells after 24h incubation with GNP-naked (a and d), GNP@PEG (b and e) and SPION-DX (c and e) at treatment concentrations of 20, 50, 100, and 200 µg/mL.

5.4. **Radiosensitization effect**

Cell survival was quantified by standard clonogenic assays, and the resultant SF were plotted as a function of dose. To enable a clearer visualization, cell dose responses were plotted both as SF curves (semilogarithmic scale) and as bar graphs. As recommended [47], [72], we expressed the NP effect on radiation response in terms of a sensitization enhancement ratio at a 10% survival fraction ($SER_{10\%}$). Values above 1 mean that the treatment of interest enhances the cell death in comparison to control group. The α and β values were extracted from the cell survival curves fitting to the LQ model. Fold change in α/β ratio is defined as the ratio of α/β from sample of interest (with NP treatment) on α/β from control sample (without NPs treatment). In addition to the clonogenic assay, immunofluorescence assays were performed with U87 GBM cells treated with GNP@PEG and GNP-naked and irradiated with gamma rays and proton beams to assess the mechanisms of DNA damage and repair.

5.4.1. **Radiossensitization induced by gold and iron oxide nanoparticles in U87 glioblastomas cells**

Figure 5.5a shows SF curves for U87 GBM cells pre-incubated during 24h with GNPs and SPION-DX at 20 µg/mL and irradiated with 6MV photons at doses up to 8 Gy. The same data is presented in bar format, so that it is possible to analyse the statistically significant differences for the individual doses. From figure 5.5a, we can see that GNP-naked leads to an enhancement on radiation-induced cell killing compared to the effect of radiation alone. In fact, there is a significant reduction in U87 cell survival at the 1 and 4 Gy doses. This effect is reflected in the values of $SER_{10\%,}$ for which the GNP-naked treatment presented a value of 1.26.

For SPION-DX NPs, the SF curve also suggests that the presence of NPs leads to an increase in cell death induced by radiation ($SER_{10\%}$ = 1.08), although not as pronounced as for GNP-naked. At the lower doses of 1 and 2 Gy, the survival of cells treated with SPION-DX is slightly above the control group, forming a shoulder in the initial region of the curve. Such variations in curve shape are indicated by changes in α/β ratios. The presence of SPION-DX led to a significant decrease in α/β ratios of U87 SF curves irradiated with 6 MV X-rays. The fold change was 0.06, indicating that the

curve for control cells is steeper than for treated cells. In contrast, the presence of GNPs induced an increase in α/β ratios after irradiation, with a fold change of 1.33.

As mentioned in the Fundamentals Chapter, Curtis et. al [65] suggested a radiobiology significance of these parameters in his LPL repair model. In summary, an increase in the linear component of survival fraction [exp(-αD)], and consequently in α/β ratios means a more significant contribution of non-repairable such as DSBs and complex damage. The opposite is also true, a decrease in the in α/β ratios means a more significant contribution of repairable lesions. From this, we may assume that the decrease in α/β ratios for SPION-DX treatments indicates a greater proportion of repairable cell damage, and that indirect damage resulted from ROS production is the dominant process involved in the radiossensitization effect induced by this NP. On the other hand, an increase in α/β ratios for GNPs treatments indicates that the formation of lethal lesions, such as complex damage, is the most relevant process to the enhancement observed.

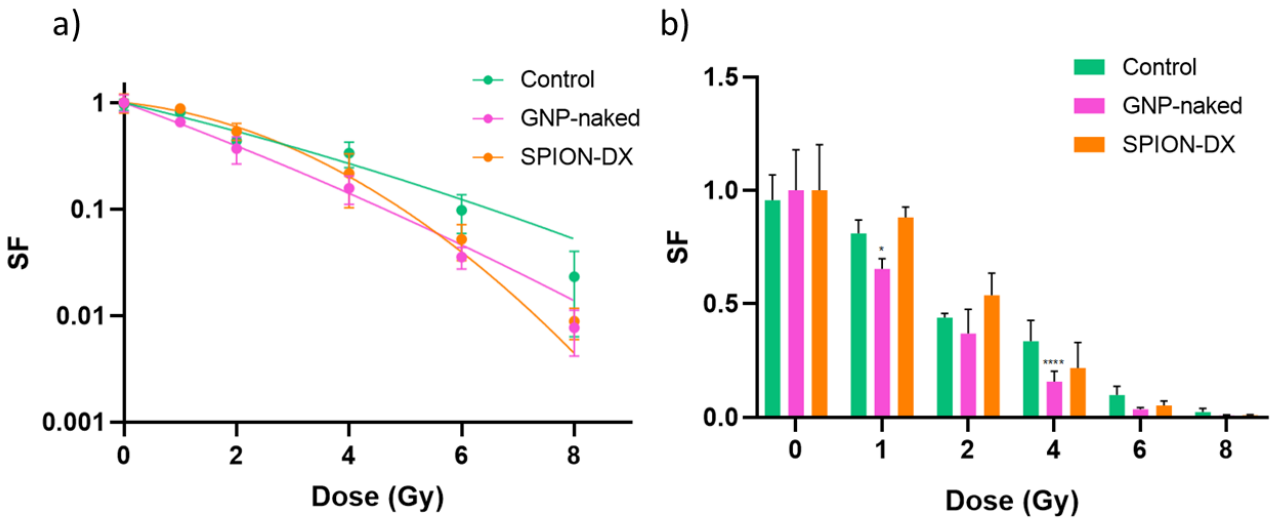

Figure 5.5. a) SF curves for U87 cells after 24h incubation with 20 μg/mL GNP-naked irradiated with 6 MV X-rays. The same data was plotted as bars b) for a better visualization. P-values are presented as: * p<0.05; ** p<0.01; *** p<0.001; **** p<0.0001.

GNPs were also effective when combined with the other beams tested. Figure 5.6a shows SF curves for U87 GBM cells pre-incubated during 24h with GNP-naked and GNP@PEG at 20 μg/mL and irradiated with 662 keV gamma rays and 150 MeV protons. The respective bar graphs are shown as well (Figure 5.6b). Fold changes in α/β ratio as well as $SER_{10\%}$ values are reported in Table 5.2. As we can see by the SF

curves in Figure 5.6a, the addition of GNPs led to a significant decrease in U87 cell survival for both gamma and proton irradiations. For gamma irradiations, $SER_{10\%}$ values were 1.77 and 1.55 for treatments with GNP-naked and GNP@PEG, respectively. When evaluating the influence of NPs in individual doses, both treatments showed significant differences at 1, 2 and 4 Gy. From Table 5.3, it is evident that the addition of NPs increased α/β ratios (Fold change of 1.34 and 2.45 for GNP-naked and GNP@PEG, respectively).

If we compare the case of GNP-naked at 20 mg/mL, the radiosensitization effect was stronger for gamma-ray ($SER_{10\%}$ = 1.77), than for 6 MV X-rays ($SER_{10\%}$ = 1.26). Such findings indicate that dose enhancement induced by GNPs decreases with increasing photon energy. Other studies have found similar results when comparing photons of different energies [188]. Based on physical enhancement, high-Z materials irradiated with low energy photons (such as gamma rays interaction used in this study), the photoelectric cross section dominates the mechanisms, leading to a local increase of energy deposition near the NP. As the photon energy increases, the Compton effect becomes predominant, decreasing the physical contribution of the LEEs in the local dose enhancement, which is the case for the 6 MV X-rays irradiations.

The use of GNPs in combination with proton beams also shows a tendency to increase radiation-induced cell death, which was reflected in the $SER_{10\%}$ values extracted from the SF curves ($SER_{10\%}$ = 1.47 for GNP-naked, and $SER_{10\%}$ = 1.31 for GNP@PEG) and an increase in α/β ratios (fold change of 1.62 for GNP-naked and 1.52 for GNP@PEG). Such results contradict the expectation that GNPs would not be an effective radiosensitizer for proton therapy, due to the high density of ionizing track induced by protons and the weak dependence on Z of the ionization interactions of charged particles [133], [189]. Other studies have also shown that metal-based NPs have radiosensitizing potential when combined with proton beams, with enhancements being observed in both *in vitro* [20], [73], [92], [131] and *in vivo* [31], [134]experiments.

The efficiency of gold to enhance the effects of proton radiation was confirmed *in vitro* by Polf et al. [131]. They observed a significant increase (15–19% RBE at 10 and 50% survival, respectively) of prostate tumour cell mortality when loaded with gold containing phage-nanoscaffolds (44 nm diameter, 1 ng gold per cell) and irradiated by 160 MeV protons. Kim et al.[134] attributed the amplification of tumor regression and mice survival treated by 40 MeV protons combined with metallic nanoparticles (complete tumor regression >37% with 100–300 mg gold/kg) is related to ROS

production in tumor cells. In addition, recent molecular scale experiments performed with platinum and gadolinium nanoparticles, activated by 150 MeV protons, highlighted the amplification of nanosize bio-damage [16]. Here again, the role of hydroxyl radicals was shown.

Comparing the effect of the NP coating, overall, GNP-naked treatments were more effective in increasing radiation-induced cell death when compared to PEG-coated particles, as can be seen by $SER_{10\%}$ values in Table 5.3. Some studies have indicated that the polymeric coating can reduce the emission of LEEs by the particle, since its presence increases the distance that the electron must travel to interact with the biological environment [22]. It was also reported that polymeric coatings may reduce the catalytic effect of NPs [190], [191], by preventing surface electrons from contributing to chemical reactions induced by radiation, such as the water radiolysis. A recent theoretical study by Haume et al. [192] suggests that the presence of a layer of PEG around NPs of 1.6 nm dramatically reduces the production of hydroxyl radicals when irradiated by carbon ions.

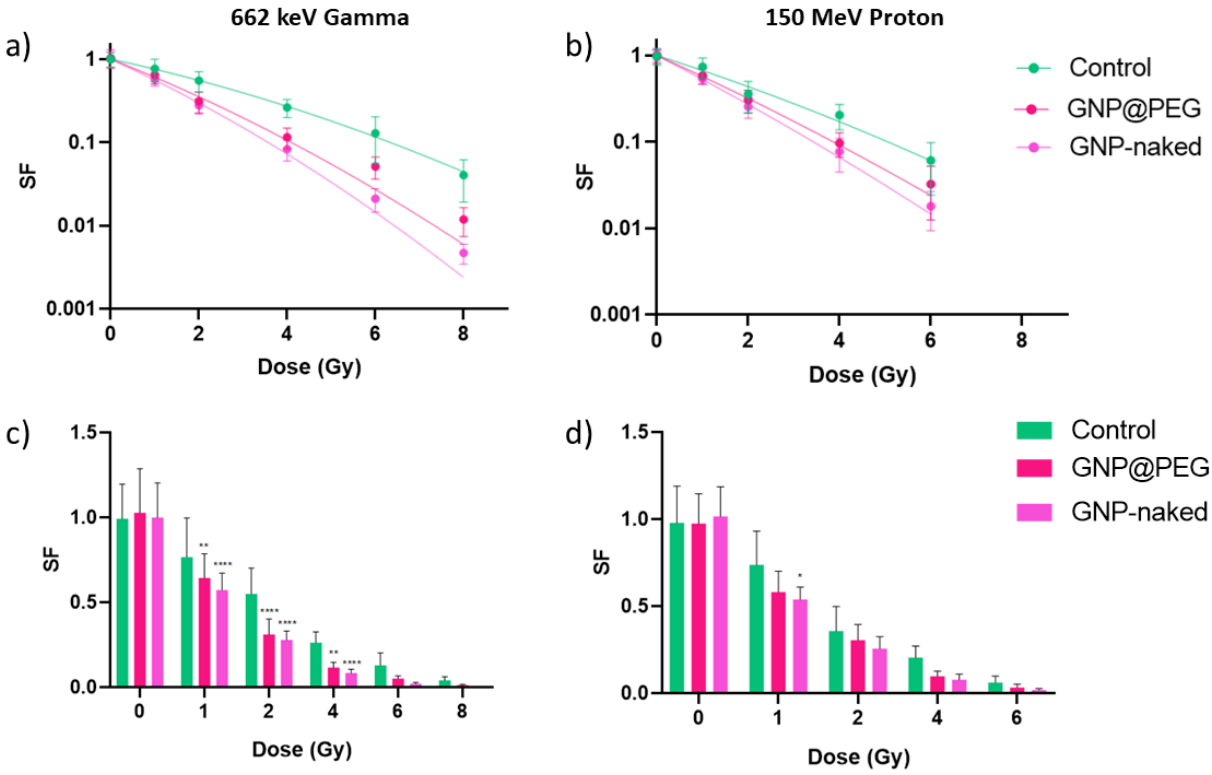

Figure 5.6. SF curves for U87 cells after 24h incubation with 20 μg/mL GNP-naked and GNP@PEG irradiated with a) 662 keV gamma rays and b) 150 MeV H^+ beam. The same data was plotted as bar graphs c) and d) for a better visualization. P-values are presented as: * p<0.05; ** p<0.01; *** p<0.001; **** p<0.0001.

Table 5.2. Sensitization enhancement ratio calculated at a 10% survival ($SER_{10\%}$) for U87 cells irradiated by 662 keV gamma rays and 150 MeV protons after being pre-incubated during 24 h with 20 μg/mL of GNPs-naked and GNP@PEG. $SF_{10\%}$ indicates the dose needed to reduce survival fraction to 10%. Fitting parameters (α and β) were calculated based on the LQ model. Fold change in a/b ratio is defined as the ratio of α/β from sample of interest (with NP treatment) on $\alpha/\beta$from control sample (without NPs treatment).

Beam	Nanoparticle	$SF_{10\%}$ (Gy)	$SER_{10\%}$	Fold change in α/β ratio
662 keV Gamma	Control	6.33	-	-
	GNP-naked	4.09	1.77	1.34
	GNP@PEG	3.57	1.55	2.45
150 MeV Proton	Control	5.06	-	-
	GNP-naked	3.43	1.47	1.62
	GNP@PEG	3.86	1.31	1.52

5.4.1.1. Influence of concentration on the radiossensitization induced by nanoparticles

Once the radiosensitization effect was confirmed for the 20 μg/mL treatments, the study was extended to investigate the effect of NP concentration. Figure 5.7a shows SF curves for U87 GBM cells pre-incubated during 24h with GNP-naked and SPION-DX at 20, 50 and 100 μg/mL, and irradiated with 6MV photons at doses up to 8 Gy. The respective bar graphs are shown as well (Figure 5.7b). Fold changes in α/β ratio as well as $SER_{10\%}$ values are reported in Table 5.3.

In the case of GNPs, the radiosensitization effect increased with increasing treatment concentration. This correlates with statistically significant enhancement of elemental cellular uptake observed, where the internalization of GNPs increases with increasing concentration. The same was not observed for SPION-DX. For U87 cells, although significant radiosensitization effects were reported for all treatment concentrations investigated, our results suggested a saturation in the sensitization enhancement with respect to treatment concentration. SPION-DX were more effective at 50 μg/mL ($SER_{10\%}$ = 1.61) than at 100 μg/mL ($SER_{10\%}$ = 1.49). Regarding elemental uptake, no significant difference was observed. It is also interesting to note that the presence of SPION-DX had a positive impact in U87 control groups. In Figure 5.7b one can see that the SF of U87 cells at 0 Gy is significantly higher for all SPION-DX

concentrations. The cause of this effect is at present unclear. We speculated that this could be attributed to the effect of dextran in physiological cell function. Dextrans are mainly composed by glucose (which has a complex role in cell signalling, besides being the main source of energy of cells) [193], [194] which presence may lead to an increase in cellular resistance to radiation.

Regarding the shape of the SF curves, higher concentrations of GNPs led to increasingly steeper curves, reaching a 13.78-fold change in α/β ratio at 100 μg/mL. In a recent review on gold nanoparticles as radiosensitizers, Penninckx at al. [72] calculated α and β parameters for cell survival curves from several *in vitro* studies, where a range of photon energies and distinct coatings were covered. In most of the cases, higher α/β were reported when GNPs were present during cell irradiation, as in our study. For U87 GBM cells irradiated with 6 MV X-rays, a lower increase of 1.06 in α/β fold change was found [112]. Closer values to those found in this study at 20 and 50 μg/mL were obtained for 6 MV X-rays irradiations for MCF-7 (1.36) [112], and MDA-MB-231 (from 1.41 to 1.86) [195], [196] human breast cancer cells, and HeLa cervical cancer cells (from 1.12 to 2.13) [97], [197], but none as higher as the one we have found for 100 μg/mL. In the case of SPION-DX, despite the shoulder decreasing with increasing concentration, the fold changes kept values below 1, indicating that the radiation effect alone leads to the formation of a straighter curve. Although there is no information on α/β ratios variations for iron oxide nanoparticles, the relevance of indirect damaged induced by ROS production in the radiosensitization effect of these nanoparticle has been highlighted in the literature [20], [34], [67].

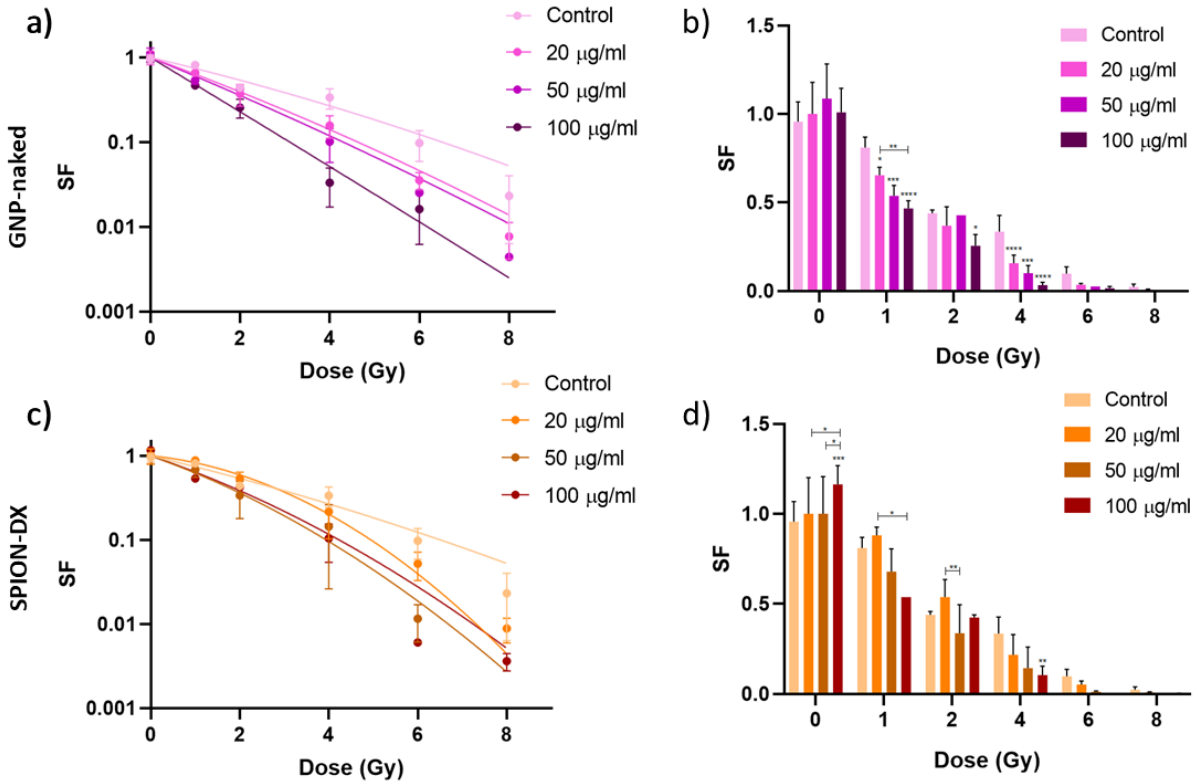

Figure 5.7. SF curves for U87 cells treated with different concentrations of a) GNP-naked, and c) SPION-DX, irradiated with 6 MV X-rays. The same data is plotted on the right (b and d) as bar graphs. P-values are presented as: * p<0.05; ** p<0.01; *** p<0.001; **** p<0.0001.

5.4.2. **Radiossensitization induced by gold and iron oxide nanoparticles in M059J GBM cells**

Figure 5.8a shows SF curves for M059J GBM cells pre-incubated during 24h with GNP-naked and SPION-DX at 20, 50 and 100 μg/mL, and irradiated with 6MV clinical photons at doses up to 8 Gy. The respective bar graphs are shown as well (Figure 5.8b). Fold changes in α/β ratio as well as $SER_{10\%}$ values are reported in Table 5.3. For M059J cells incubated with GNP-naked, all $SER_{10\%}$ values were above 1, indicating that the presence of NPs increased radiation-induced cell death. Such enhancement is proportional to elemental cellular uptake, where the highest enhancement was achieved at 100 μg/mL ($SER_{10\%}$ = 1.30). When assessing the effect on each radiation dose individually (Fig. 5.8b), there are significant differences between GNP-naked treatments and M059J control groups at 1 and 2 Gy. In addition, the presence of GNPs induced an increase in α/β ratios after irradiation and that such

increasing is proportional to treatment concentration. Fold change in α/β ratios for the same concentrations were 1.72, 1.96 and 2.29.

For SPION-DX, at 20 and 50 μg/mL presented $SER_{10\%}$ values of 0.87 and 0.95, respectively, indicating that for the treated cells, a higher radiation dose is necessary to eliminate the same number of cells as the control group. However, for the highest concentration treatment of 100 μg/mL, SPION-DX induced a small increase of 6% in cell killing. The shape of the survival curves for M059J cells incubated with SPION-DX did not differ much from cells subjected only to radiation. The α/β ratios obtained from 20 μg/mL and 50 μg/mL curves were similar to control group (fold changes of 0.98 and 1, respectively). Only for 100 μg/mL an evident decrease in α/β ratio was observed (0.57-fold change). Overall, the radiosensitization effect was not as pronounced for M059J cells as for U87 ones.

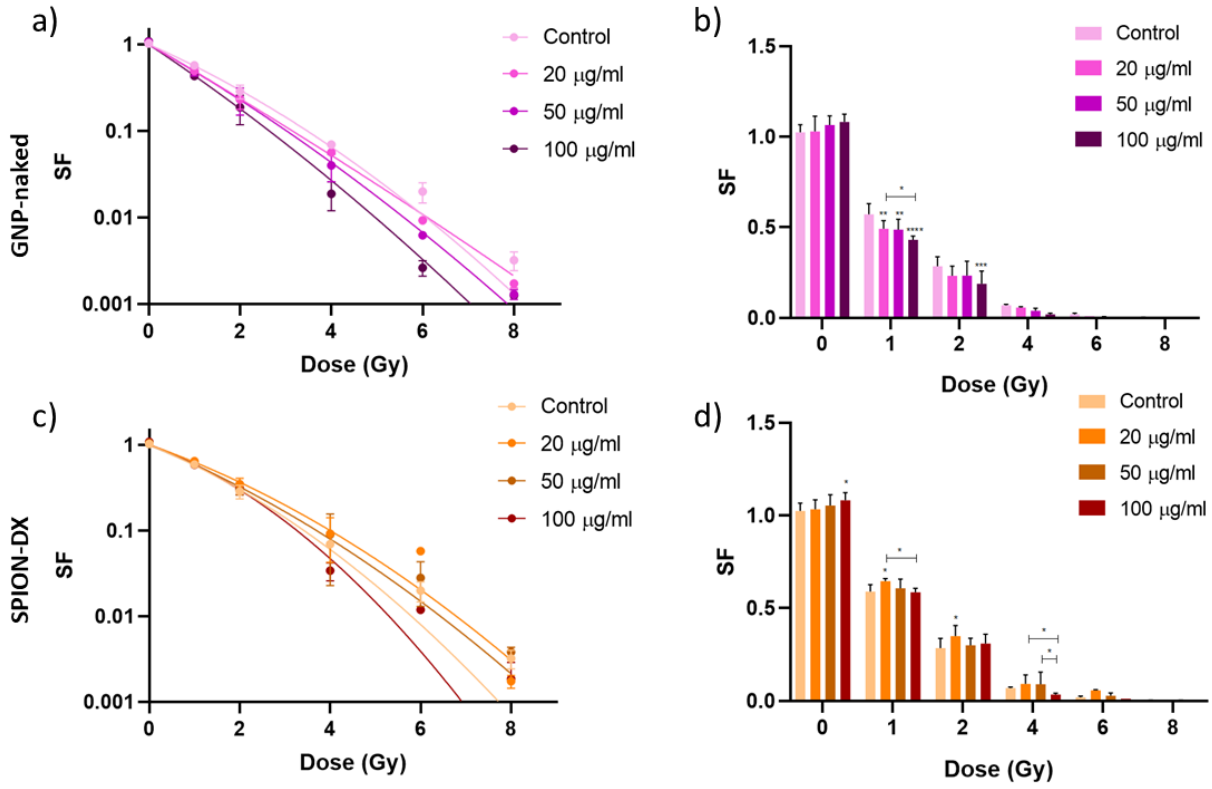

Figure 5.8. SF curves for U87 cells treated with different concentrations of a) GNP-naked, and c) SPION-DX, irradiated with 6 MV X-rays. The same data is plotted on the right (b and d) as bar graphs. P-values are presented as: * p<0.05; ** p<0.01; *** p<0.001; **** p<0.0001.

Table 5.3. Sensitization enhancement ratio calculated at a 10% survival ($SER_{10\%}$) for U87 and M059J cells irradiated by 6 MV photons after being pre incubated during 24 h with GNPs and SPION-DX at treatments concentrations of 20, 50 and 100 μg/mL. $SF_{10\%}$ indicates the dose needed to reduce survival fraction to 10%. Fitting parameters (α and β) were calculated based on the LQ model. Fold change in α/β ratio is defined as the ratio of α/β from sample of interest (with NP treatment) to the α/β from control sample (without NPs treatment).

Cell line	Nanoparticle	Concentration	$SF_{10\%}$ (Gy)	$SER_{10\%}$	Fold change in α/β ratio
U87	Control	-	6.28	-	-
	GNP-naked	20 μg/mL	4.98	1.26	1.33
		50 μg/mL	4.28	1.46	2.17
		100 μg/mL	3.08	2.04	13.78
	SPION-DX	20 μg/mL	5.42	1.15	0.06
		50 μg/mL	3.89	1.61	0.38
		100 μg/mL	4.21	1.49	0.46
M059J	Control	-	3.46	-	-
	GNP-naked	20 μg/mL	3.20	1.08	1.72
		50 μg/mL	3.11	1.13	1.96
		100 μg/mL	2.66	1.30	2.29
	SPION-DX	20 μg/mL	3.98	0.87	0.98
		50 μg/mL	3.64	0.95	1.0
		100 μg/mL	3.26	1.06	0.57

5.5. Influence of gold nanoparticles in radiation-induced DNA damage and repair mechanisms

The cells were fixed at 15 min, 2, 4 and 24 hours after irradiation, following staining with antibodies, as described in Section 4.2.5, for analysis of DNA damage and repair. Examples of images of cells fixed at 15 min post-radiation are shown in Figure 5.9. The presence of γH2AX and 53BP1 foci is easily detected by red and green fluorescence spots, respectively, within the nuclei. Cell nuclei were labeled with DAPI. As we can see in Figure 5.9a, control cells do not show γH2AX-foci, while irradiated cells (Figure 5.9 b and c) have a large number of green spots. As 53BP1 is involved in cellular mechanisms other than just DNA repair, it is common to find some foci in control cells [58]. Nevertheless, irradiated cells have a greater number of 53BP1-foci than control group.

The extent of DNA damage was expressed as average number of γH2AX- and 53BP1-foci per nucleus cell or mean percentage of γH2AX- and 53BP1-positive nuclei. A positive nucleus is a nucleus showing at least one clear visible fluorescent spot. Figure 5.10 shows the quantification of number of foci per cell, as well as the percentage of positive cells for U87 GBM cells treated with 20 μg/mL GNP@PEG and GNP-naked and irradiated with 662 keV gamma rays and 150 MeV proton beam. One can see that the presence of GNP-naked and GNP@PEG induced significant higher levels of DSBs at 4 hours post-irradiation for both radiation types. When combining gamma radiation with GNP@PEG, there was also a significant enhancement in γH2AX foci/cell when considering immediate damage (15-min time point).

By analyzing the number of positive cells for foci formation, one can see that for both proton and gamma radiation, the cells treated with GNPs showed a decrease in the number of cells with repair foci 24 hours post-irradiation, while there is no difference for cells that show damage sites. These findings show that the presence of GNPs induced a higher number of cells with residuals DSBs, which cannot be repaired anymore. The increase in residual DSBs is consistent with our clonogenic results, where the presence of GNPs led to lower cell survival.

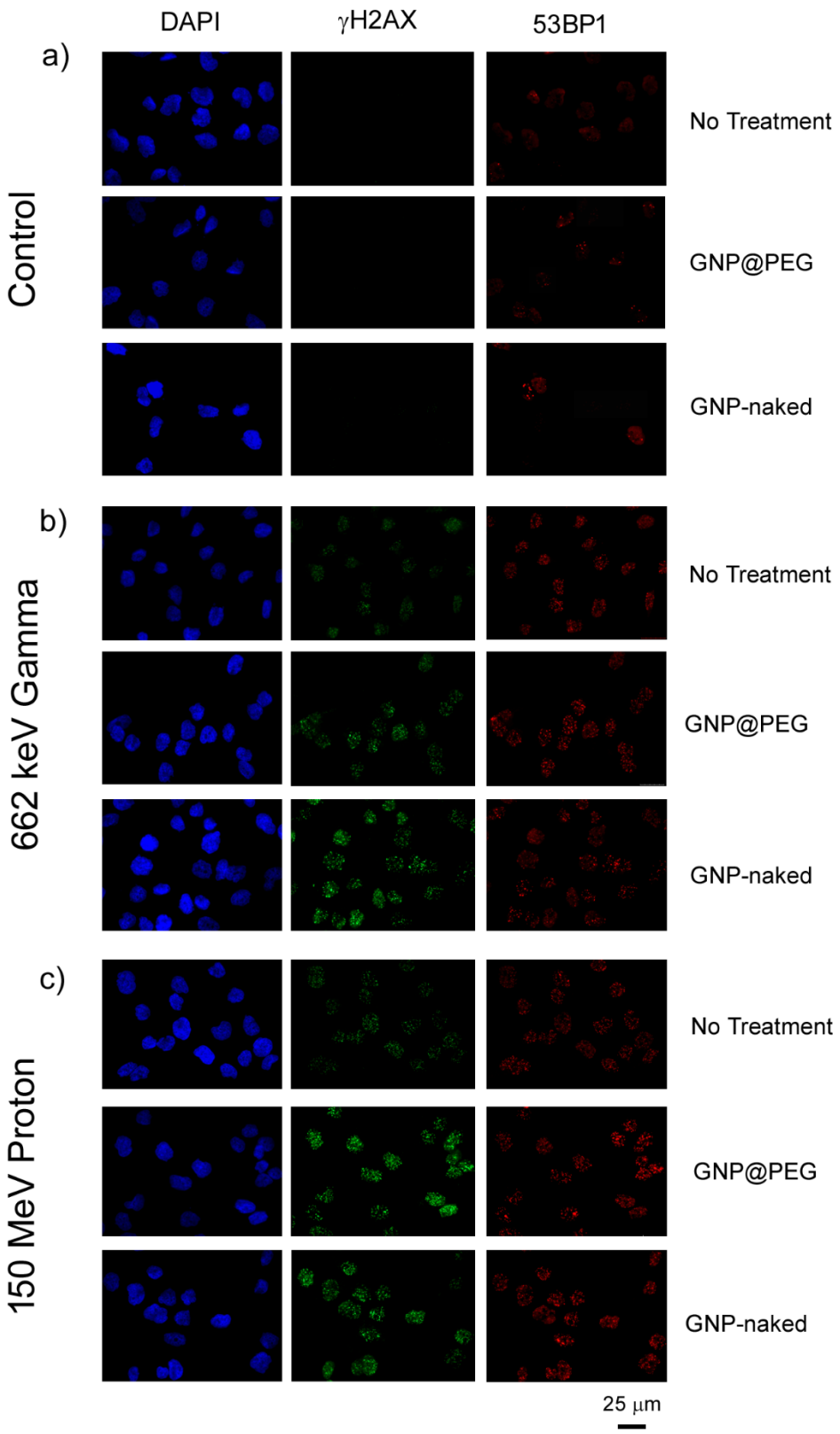

Figure 5.9. Analysis of DNA damage (DSB) and repair of irradiated U87 GBM cells. Cells were incubated with 20 μg/mL GNP@PEG and GNP-naked for 24 hours. DNA DSBs sites were detected by immunofluorescence with anti-γH2AX (green) and repair by anti-53BP1 (red). DAPI stain the nuclei. A control group (a) was taken to the irradiation site, but it was not exposed to radiation. Cells were irradiated with b) 662 keV gamma rays and c) 150 MeV H^+ beam and fixed 15 minutes post-irradiation.

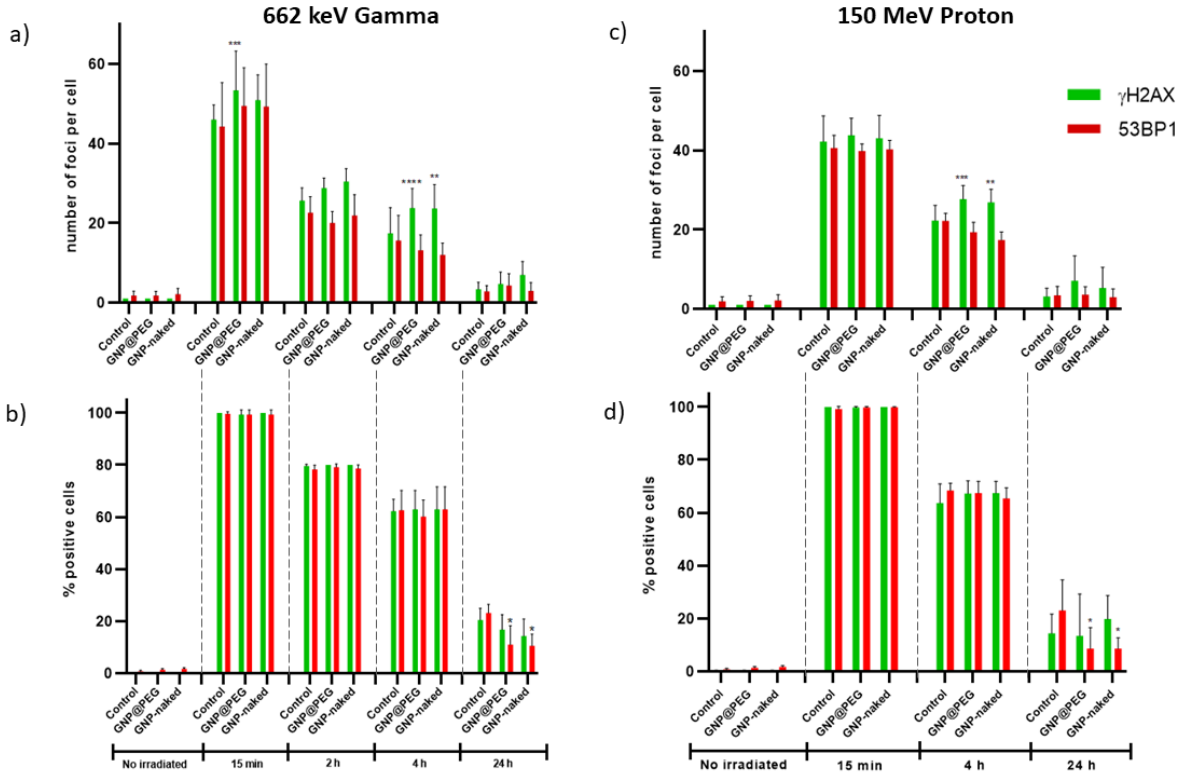

Figure 5.10. Number of 53BP1 and H2AX foci per cell counting and average percentage of positive cells for U87 GBM cells incubated with 20 μg/mL GNP@PEG and GNP-naked for 24 hours. Cells were irradiated with 662 keV gamma rays (a and b) and 150 MeV H^+ beam and fixed at different time points post-irradiation. P-values are presented as: * p<0.05; ** p<0.01; *** p<0.001; **** p<0.0001

Although it is often assumed that NPs need to be placed within the cell nucleus to induce DNA damage, our findings demonstrate that GNPs can increase residual DSBs even though they are located in the cytoplasm. It has been proposed in the literature that enhanced DSBs is due to an increase in ROS production, and consequently indirect DNA damage [160], [161]. If the volume of indirect damage is high enough, the probability of complex damage generation increases, which would saturate the cell's repair mechanisms. Other studies [162], [163] proposed that the presence of NPs did not influence the total number of DSBs per cell, but rather a decrease in the repair process rate. Both hypotheses are in line with what we have observed in clonogenic assays. Concerning ROS production, the steeper curves of cells irradiated in the presence of GNPs indicate a higher contribution of lethal damage, which may be achieve by a great volume of indirect effect, leading to DNA complex damage. The second hypothesis also seems to be in agreement with our results, since no differences were observed in the total number of DNA damage after 24 hours, but there was a significant decrease in the number of cells undergoing repair. In addition,

if the volume of complex damage is large enough, cell repair mechanisms can become saturated, leading to cell death.

Chithrani et al. found that incubation of HeLa cells with 50 nm citrate-AuNPs increased the number of γH2AX and 53BP1 foci at 4 and 24 h post-irradiation at both 220 kVp and 6 MV energies. Based on these findings, the increased residual damage in the presence of nanoparticles, which is indicative of delayed DNA repair, was suggested to be a key mode of radiosensitization [197]. Further evidence for GNP-induced inhibition of DNA repair was provided by Cui et al., who reported a significant increase in the residual DNA damage (24 h post-IR) in cells irradiated with 250 kVp X-rays in the presence of 2.7 nm tiopronin-GNPs, while no effect was seen on the initial (30 min post- IR) levels of DNA DSBs [162]. Based on these findings and considering the influential role of DNA repair in radiosensitization, inhibition of DNA damage response pathways appears to be a plausible mechanism of dose enhancement by GNPs.

5.1. **Changes in nuclei morphology induced by the presence of GNPs during irradiation**

Analysis of nuclear morphology after irradiation was also conducted as a complement to the DNA damage/repair studies. Figure 5.11 shows preliminary results of NMA of U87 cells irradiated with 662 keV gamma rays. The figure displays the distribution of nuclei area versus nuclear irregularity index (NII) for U87 GBM cells incubated for 24h with GNP@PEG, and GNP-naked. Results for irradiations with 150 MeV H+ is shown in Figure 5.12. The control (non-irradiated and not incubated with GNPs) and the irradiated control (irradiated and not incubated with GNPs) groups are plotted overlaying the data from irradiated samples. The graph is divided in six regions; N: normal, I: irregular, LR: large regular; LI: large irregular; SR: small regular; SI: small irregular. In the normal (N) region of the graph there is an ellipse defined from a population of normal/regular nuclei, delimiting the region that corresponds to the normal cells. In all cases, non-irradiated control cells (red spots) have a homogeneous and uniform distribution, remaining inside or close to the normal ellipse.

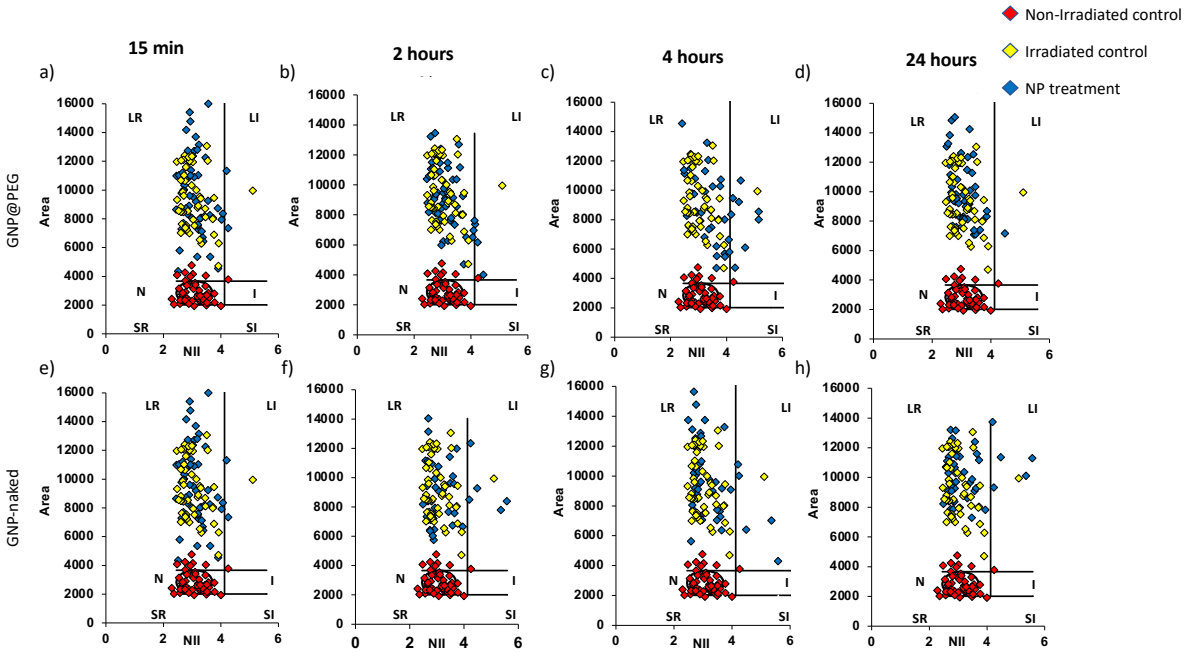

Figure 5.11. Distribution of nuclei for U87 GBM cells incubated for 24h with a-d) GNP@PEG, and e-h) GNP-naked and irradiated with 662 keV gamma rays. The distribution of nuclei is represented as a plot of area versus NII. N: Normal nuclei (crosses represent nuclei used to establish the reference population and the ellipse that represents the conjoint distribution for area and NII for normal nuclei); I: irregular, LR: Large Regular; LI: Large Irregular; SR: Small Regular; SI: Small Irregular.

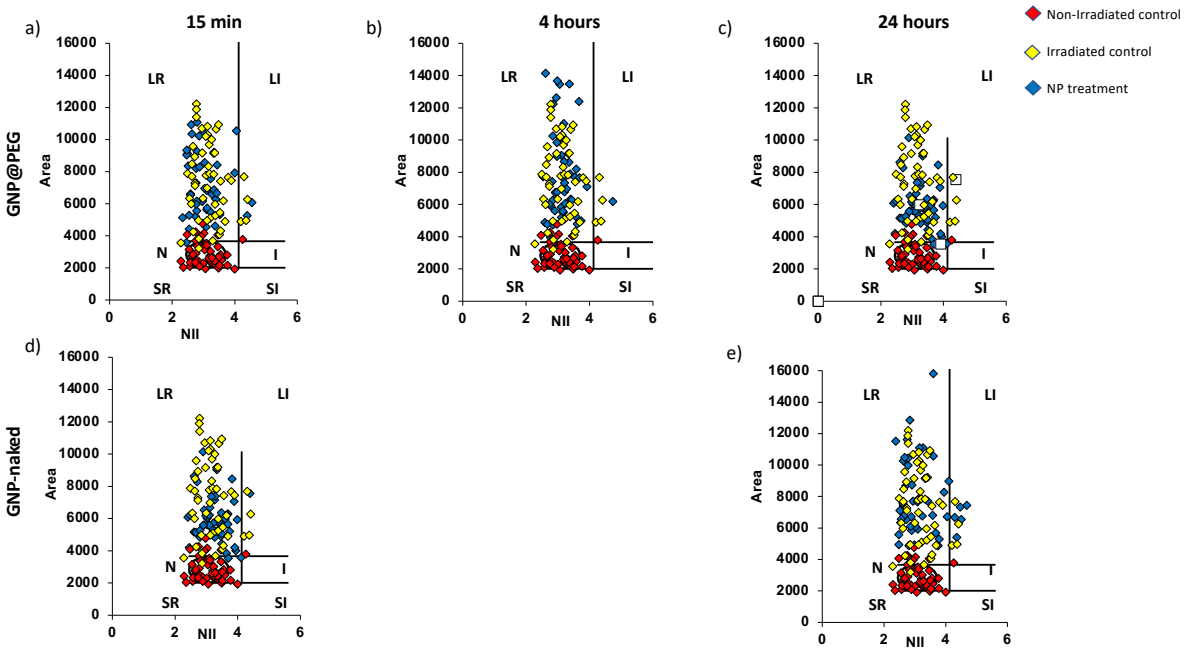

Figure 5.12. Distribution of nuclei for U87 GBM cells incubated for 24h with a-c) GNP@PEG, and d) and e) GNP-naked and irradiated with 150 MeV H^+. The distribution of nuclei is represented as a plot of area versus NII. N: Normal nuclei (crosses represent nuclei used to establish the reference population and the ellipse that represents the conjoint distribution for area and NII for normal nuclei); I: irregular, LR: Large Regular; LI: Large Irregular; SR: Small Regular; SI: Small Irregular.

The population of cells irradiated with 662 keV gamma rays is mostly located on the left upper region of the graph, for all investigated time points, indicating nuclei with area above the normal ellipse, but with NII similar to normal ones. Cells incubated with 20 μg/mL GNP@PEG and subjected to radiation present a similar morphology to those exposed to radiation alone, except for the 24h-time point, where the distribution of the nuclei shifts to the upper right region of the graph. Such nuclei have an area above the "normal ellipse", but with NII higher than that of normal ones. For GNP-naked this shift is observed at 2-, 4- and 24-hour time points. Only at 15-min post-irradiation the morphology of the nuclei is like that of nuclei that have been exposed to radiation alone.

In the case of irradiations with 150 MeV protons, the irradiated cell population also shifts to the upper region of the graph, indicating large and regular nuclei. Cells that were incubated with GNPs have a similar morphology to unexposed cells, except for GNP-naked at 24-h post-irradiation, where a fraction of the population of cells incubated with NPs is in the upper right region of the figure. These results indicate that

the presence of GNPs during irradiation lead to changes in cell morphology not only in relation to the control group, but also in relation to irradiated cells not exposed to nanoparticles.

Alteration in nuclear morphology occurs in physiologic situations, like during mitosis, and in several processes associated with cell death. These modifications include increase in nuclear size observed in senescence, and increase in nuclear irregularity observed in several conditions, such as chemical or physical stresses, defective activation or inactivation of cell checkpoint signaling processes, or exogenous agents that affect microtubule dynamics or chromatin remodeling[198], [199].

When the distribution of nuclei is in the normal region of the plot, it indicates that the cells are in Interphase without damage that affects nuclear morphology. Cell migration to the LR region indicates that they are entering senescence [179]. Senescence produces a drastic increase in cellular and nuclear size, but its contour remains within the patterns of a regular cell. Accumulation of nuclear DNA and mitochondrial damage can lead to cell senescence, and consequently loss of their proliferative capacity [47]. Based on that, one can assume that irradiation generate enough damage for the cells to lose their reproductive capacity irrespective of the presence of NPs. These findings are in agreement with the results obtained in clonogenic assays, where colony formation is reduced for irradiated cells.

Furthermore, the shift to the upper right region induced by the presence of GNPS indicates that the cells suffered a significant nuclear damage, which may indicate a mitotic catastrophe or other nuclear damaging event. This is in agreement with the increase in DSBs observed for a time point of 4 hours post-irradiation and with the increase in residual DSBs after 24 hours. Taken together these findings indicate that the induction of non-repairable (lethal) damage is one of the mechanisms responsible for the radiosensitization effect induced by GNPs.

It is important to highlight that the nuclear morphology method is too simplistic for a definitive identification of such complex cellular processes. Final identification of these processes must be confirmed with standard techniques for each individual process. However, the ability to easily identify these processes simultaneously gives this tool the advantage of an overview of the population dynamics related to these processes.

6. CONCLUSIONS

Metal-based NPs have been shown to be a strong candidate as radiosensitizer agents, but despite having been extensively explored in the literature, the great variability in the methods of quantification and the studied variables, there is a great difficulty in translating preclinical studies into clinical trials. Therefore, the present study used robust and systematic model to investigate the basic mechanism of the radiosensitization process assisted by metal-based NPs. We followed the standardized recommendations to report on the efficacy of NP-enhanced radiotherapy, highlighting metrics such as NP cellular uptake, cell survival (using fitting parameters α and β obtained from the linear-quadratic (LQ) model), and the enhancement sensitization ratio at 10% survival ($SER_{10\%}$). In addition, we investigated a wide range of treatment concentrations, comparing different types of NPs.

In conclusion, we have demonstrated a significant radiosensitization effect induced by metal-based NPs in GBM cell lines using different types of radiation, including a clinical 6 MV photon platform. The radiosensitization values found are superior to enhancements reported in other works in the literature, reaching a 2-fold increase. The presence of SPION-DX caused a significant reduction in cell survival when combined with ionizing radiation, achieving enhancements of 61%, even when no enhancement is expected due to the low Z of iron. Other studies have evaluated the potential of iron oxide NPs as radiosensitizers, but none have systematically evaluated the effect of different concentrations, and most used simpler analytical methods, such as MTT assays [109]. From our findings, the radiosensitization effect of SPION-DX seems to reach a saturation point, where similar values of sensitization enhancement with respect to concentration were found above 50 μg/mL. In addition, fold changes in α/β ratios kept values bellow 1, despite the shoulder decreasing with increasing concentration. According to the LPL model, this indicates that the presence of SPION-DX induced a greater proportion of repairable cell damage.

For GNPs, cell survival was dependent on NP concentration, where the radiosensitization effect increased with increasing treatment concentration. This correlates with the statistically significant increase of elemental cellular uptake observed. NPs also affects the shape of SF curves, where higher concentrations of GNPs led to increasingly steeper curves. From this, we may assume that the presence

of NPs is inducing an increase in lethal damage, preventing the repair from being successfully performed. In addition to these findings, our immunofluorescence assay revealed that the presence of GNPs during irradiation increased residual DSBs. NMA results corroborate such findings, where cells irradiated in the presence of NPs presented morphologies related to nuclear damage and mitotic catastrophe. Such alterations were observed in the mechanisms of DNA damage and repair, even though the NPs were located in the cytoplasm. We can assume two mechanisms to explain this effect, the first is based on the hypothesis that NPs induce a large production of ROS, which form a cluster of complex DNA damage, saturating the repair mechanisms. A second plausible hypothesis is that NPs inhibit DNA repair processes, leading to an increase in residual DSBs.

GNPs were also effective when combined with different types of radiation to induce an enhancement in U87 cell killing. In addition, it was evident that the NPs increased α/β ratios for all radiation types. When comparing the different photon energies, gamma rays induced the most significant decrease in cell survival, when compared to 6 MV X-rays. Such findings indicate that dose enhancement induced by GNPs decreases with increasing photon energy, which can be explained by the contribution of photoelectric effect for low energy photons. The coating was also found to be important, as GNP-naked treatments were more effective in increasing radiation-induced cell death when compared to PEG-coated particles. This may be attributed to the reduction of the production of LEEs and hydroxyl radicals due to the presence of a layer of PEG around GNPs.

It is also interesting to note that the NP-induced radiosensitization was not as pronounced for the radiosensitive cells as for the radioresistant ones. One may assume that, as radiosensitive cells are already susceptible to radiation-induced death, the presence of NPs produces more damage than is actually needed to kill the cells, generating an overkill-like effect.

From our findings the complex nature of NP-enhanced radiotherapy was demonstrated, highlighting the dependence of radiosensitization mechanisms on NP design, treatment concentration, type of radiation and investigated cell line. Due to such complexity, future studies are needed to elucidate the exact mechanism of action in a biological system.

7. FUTURE STUDIES

Although important experimental correlations were observed between NP type, concentration and coating, and their sensitization capacity, further studies are needed to better understand the mechanisms involved. First, it is necessary to expand the data already collected, exploring other cell lines, including different types of cancer and normal tissue cells. It is also important to investigate other designs of NPs, evaluating different combinations of elemental material and coating. Furthermore, it is necessary to elucidate the precise mechanisms of radiosensitization at the molecular and cellular levels, including the potential impact on cellular signalling, quantification of ROS, and further DNA damage/repair assays.

We shall also comment on the limitations of monolayer cell cultures which may not reflect the complexity of tumor/normal tissue environment [200], such as cell-cell and cell-matrix interactions, which contribute to essential cellular functions in proliferation, differentiation and survival [201], [202]. Hence, future *in vitro* studies should be conducted using organoids (ideally with patient-specific cell lines), as this captures the true intratumor heterogeneity and tumor microenvironment [202], [203]. In addition, comparing the response of tumor-derived organoids with the response of normal tissue organoids or possibly even co-cultures are needed to establish the therapeutic window and improve our knowledge on the mechanisms involved in the radiosensitizing effect of NPs.

Furthermore, future *in vivo* studies must be performed to investigate drug metabolism, pharmacokinetic screening, biocompatibility, physicochemical properties and NP stability in a complex biological model. Concerning GBM treatments, we must consider the central nervous system (CNS) environment, which will influence cell response. For example, GBM cell lines have been shown to exhibit metastatic behavior, whereas brain tumor metastasis does not occur *in vivo* [204]. Therefore, it is relevant to study the effect of NPs on GBM radiotherapy in a confined CNS environment. Besides, the blood brain barrier (BBB) is an important factor that needs to be taken into account. For that, a more advanced NP formulation using a coating that allows crossing the BBB may be needed. Otherwise, intratumoral injection of NPs may be a realistic option for a faster clinical translation.

In view of the complex interdisciplinary nature of the radiossensitization effect, the clinical transition will require the strengthening of collaborations between multidisciplinary scientific teams and medical/pharmaceutical partners. This will enable to bridge the regulatory gap, one of the main obstacles to current developments of nanomedicine.

8. REFERÊNCIAS BIBLIOGRÁFICAS

[1] S. Stathakis, "*The Physics of Radiation Therapy*," *Med. Phys.*, vol. 37, no. 3, pp. 1374–1375, Mar. 2010, doi: 10.1118/1.3319185.

[2] J. Thariat, J.-M. Hannoun-Levi, A. Sun Myint, T. Vuong, and J.-P. Gérard, "Past, present and future of radiotherapy for the benefit of patients," *Nat. Rev. Clin. Oncol.*, vol. 10, no. 1, pp. 52–60, Jan. 2013, doi: 10.1038/nrclinonc.2012.203.

[3] H. Tsujii and T. Kamada, "A review of update clinical results of carbon ion radiotherapy," *Japanese Journal of Clinical Oncology*, vol. 42, no. 8. pp. 670–685, Aug. 2012, doi: 10.1093/jjco/hys104.

[4] M. Durante and J. S. Loeffler, "Charged particles in radiation oncology," *Nature Reviews Clinical Oncology*, vol. 7, no. 1. pp. 37–43, Jan. 2010, doi: 10.1038/nrclinonc.2009.183.

[5] M. Dosanjh, U. Amaldi, R. Mayer, and R. Poetter, "ENLIGHT: European network for Light ion hadron therapy," *Radiotherapy and Oncology*, vol. 128, no. 1. Elsevier Ireland Ltd, pp. 76–82, Jul. 01, 2018, doi: 10.1016/j.radonc.2018.03.014.

[6] M. Krämer *et al.*, "Helium ions for radiotherapy? Physical and biological verifications of a novel treatment modality," *Med. Phys.*, vol. 43, no. 4, pp. 1995–2004, Apr. 2016, doi: 10.1118/1.4944593.

[7] W. Hu *et al.*, "Outcomes of orbital malignancies treated with eye-sparing surgery and adjuvant particle radiotherapy: a retrospective study," *BMC Cancer*, vol. 19, no. 1, Dec. 2019, doi: 10.1186/s12885-019-5964-y.

[8] D. C. Weber *et al.*, "Proton therapy for pediatric malignancies: Fact, figures and costs. A joint consensus statement from the pediatric subcommittee of PTCOG, PROS and EPTN," *Radiotherapy and Oncology*, vol. 128, no. 1. Elsevier Ireland Ltd, pp. 44–55, Jul. 01, 2018, doi: 10.1016/j.radonc.2018.05.020.

[9] D. Schulz-Ertner *et al.*, "Results of carbon ion radiotherapy in 152 patients," in *International Journal of Radiation Oncology Biology Physics*, 2004, vol. 58, no.

2, pp. 631–640, doi: 10.1016/j.ijrobp.2003.09.041.

[10] W. D. Newhauser and R. Zhang, “The physics of proton therapy,” *Physics in Medicine and Biology*, vol. 60, no. 8. Institute of Physics Publishing, pp. R155–R209, Apr. 21, 2015, doi: 10.1088/0031-9155/60/8/R155.

[11] A. J. Lomax, “Charged Particle Therapy: The Physics of Interaction,” *Cancer J.*, vol. 15, no. 4, pp. 285–291, Jul. 2009, doi: 10.1097/PPO.0b013e3181af5cc7.

[12] T. Mitin and A. L. Zietman, “Promise and pitfalls of heavy-particles therapy,” *Journal of Clinical Oncology*, vol. 32, no. 26. American Society of Clinical Oncology, pp. 2855–2863, Sep. 10, 2014, doi: 10.1200/JCO.2014.55.1945.

[13] Y. Mi, Z. Shao, J. Vang, O. Kaidar-Person, and A. Z. Wang, “Application of nanotechnology to cancer radiotherapy,” *Cancer Nanotechnol.*, vol. 7, no. 1, p. 11, Dec. 2016, doi: 10.1186/s12645-016-0024-7.

[14] S. Her, D. A. Jaffray, and C. Allen, “Gold nanoparticles for applications in cancer radiotherapy: Mechanisms and recent advancements,” *Advanced Drug Delivery Reviews*, vol. 109. Elsevier B.V., pp. 84–101, Jan. 15, 2017, doi: 10.1016/j.addr.2015.12.012.

[15] A. Wicki, D. Witzigmann, V. Balasubramanian, and J. Huwyler, “Nanomedicine in cancer therapy: Challenges, opportunities, and clinical applications,” *J. Control. Release*, vol. 200, pp. 138–157, Feb. 2015, doi: 10.1016/J.JCONREL.2014.12.030.

[16] T. Schlathölter *et al.*, “Improving proton therapy by metal-containing nanoparticles: Nanoscale insights,” *Int. J. Nanomedicine*, 2016, doi: 10.2147/IJN.S99410.

[17] Z. Kuncic and S. Lacombe, “Nanoparticle radio-enhancement: principles, progress and application to cancer treatment,” *Phys. Med. Biol.*, vol. 63, no. 2, p. 02TR01, Jan. 2018, doi: 10.1088/1361-6560/aa99ce.

[18] P. Retif *et al.*, “Nanoparticles for Radiation Therapy Enhancement: the Key Parameters.,” *Theranostics*, vol. 5, no. 9, pp. 1030–44, 2015, doi: 10.7150/thno.11642.

[19] M. E. Davis, Z. (Georgia) Chen, and D. M. Shin, “Nanoparticle therapeutics: an emerging treatment modality for cancer,” in *Nanoscience and Technology*, Co-Published with Macmillan Publishers Ltd, UK, 2009, pp. 239–250.

[20] R. Abdul Rashid *et al.*, “Radiosensitization effects and ROS generation by high Z metallic nanoparticles on human colon carcinoma cell (HCT116) irradiated

under 150 MeV proton beam," *OpenNano*, vol. 4, p. 100027, Jan. 2019, doi: 10.1016/J.ONANO.2018.100027.

[21] J. F. Hainfeld, F. A. Dilmanian, D. N. Slatkin, and H. M. Smilowitz, "Radiotherapy enhancement with gold nanoparticles," *J. Pharm. Pharmacol.*, vol. 60, no. 8, pp. 977–985, Aug. 2008, doi: 10.1211/jpp.60.8.0005.

[22] S. J. McMahon *et al.*, "Biological consequences of nanoscale energy deposition near irradiated heavy atom nanoparticles," *Sci. Rep.*, vol. 1, 2011, doi: 10.1038/srep00018.

[23] C. Wälzlein, E. Scifoni, M. Krämer, and M. Durante, "Simulations of dose enhancement for heavy atom nanoparticles irradiated by protons," *Phys. Med. Biol.*, vol. 59, no. 6, pp. 1441–1458, Mar. 2014, doi: 10.1088/0031-9155/59/6/1441.

[24] F. Kazmi, K. A. Vallis, B. A. Vellayappan, A. Bandla, D. Yukun, and R. Carlisle, "Megavoltage radiosensitization of gold nanoparticles on a glioblastoma cancer cell line using a clinical platform," *Int. J. Mol. Sci.*, vol. 21, no. 2, Jan. 2020, doi: 10.3390/ijms21020429.

[25] L. Štefanciková *et al.*, "Effect of gadolinium-based nanoparticles on nuclear DNA damage and repair in glioblastoma tumor cells," *J. Nanobiotechnology*, vol. 14, no. 1, p. 63, Jul. 2016, doi: 10.1186/s12951-016-0215-8.

[26] X. Zhang, H. Wang, J. A. Coulter, and R. Yang, "Octaarginine-modified gold nanoparticles enhance the radiosensitivity of human colorectal cancer cell line LS180 to megavoltage radiation," *Int. J. Nanomedicine*, vol. 13, pp. 3541–3552, Jun. 2018, doi: 10.2147/IJN.S161157.

[27] Y. Du *et al.*, "Radiosensitization Effect of AGuIX, a Gadolinium-Based Nanoparticle, in Nonsmall Cell Lung Cancer," *ACS Appl. Mater. Interfaces*, vol. 12, no. 51, pp. 56874–56885, Dec. 2020, doi: 10.1021/acsami.0c16548.

[28] R. E *et al.*, "Impact of Superparamagnetic Iron Oxide Nanoparticles on In Vitro and In Vivo Radiosensitisation of Cancer Cells," Oct. 2020, doi: 10.21203/RS.3.RS-57415/V2.

[29] Z. Jing *et al.*, "Gallic acid-gold nanoparticles enhance radiation-induced cell death of human glioma <scp>U251</scp> cells," *IUBMB Life*, vol. 73, no. 2, pp. 398–407, Feb. 2021, doi: 10.1002/iub.2436.

[30] Z. Alyani Nezhad, G. Geraily, F. Hataminia, W. Parwaie, H. Ghanbari, and S. Gholami, "Bismuth oxide nanoparticles as agents of radiation dose enhancement

in intraoperative radiotherapy," *Med. Phys.*, p. mp.14697, Feb. 2021, doi: 10.1002/mp.14697.

[31] Y. Lin, H. Paganetti, S. J. McMahon, and J. Schuemann, "Gold nanoparticle induced vasculature damage in radiotherapy: Comparing protons, megavoltage photons, and kilovoltage photons," *Med. Phys.*, vol. 42, no. 10, pp. 5890–5902, Sep. 2015, doi: 10.1118/1.4929975.

[32] L. Dykman and N. Khlebtsov, "Gold nanoparticles in biomedical applications: recent advances and perspectives," *Chem. Soc. Rev.*, vol. 41, no. 6, pp. 2256–2282, Feb. 2012, doi: 10.1039/C1CS15166E.

[33] R. Kannan *et al.*, "Functionalized radioactive gold nanoparticles in tumor therapy," *Wiley Interdiscip. Rev. Nanomedicine Nanobiotechnology*, vol. 4, no. 1, pp. 42–51, Jan. 2012, doi: 10.1002/wnan.161.

[34] S. Klein, A. Sommer, L. V. R. Distel, W. Neuhuber, and C. Kryschi, "Superparamagnetic iron oxide nanoparticles as radiosensitizer via enhanced reactive oxygen species formation," *Biochem. Biophys. Res. Commun.*, vol. 425, no. 2, pp. 393–397, Aug. 2012, doi: 10.1016/j.bbrc.2012.07.108.

[35] I. Rosenberg, "Radiation Oncology Physics: A Handbook for Teachers and Students," *Br. J. Cancer 2008 985*, Mar. 2008.

[36] *Handbook of Radiotherapy Physics*. CRC Press, 2007.

[37] H. Nikjoo, *Interaction of Radiation with Matter*. CRC Press, 2016.

[38] C. Leroy and P. G. Rancoita, *Principles of radiation interaction in matter and detection, third edition*. World Scientific Publishing Co., 2011.

[39] H. Goldschmidt and W. K. Sherwin, "Reactions to ionizing radiation," *J. Am. Acad. Dermatol.*, vol. 3, no. 6, pp. 551–579, 1980, doi: 10.1016/S0190-9622(80)80067-3.

[40] "Khan's The Physics of Radiation Therapy - Faiz M. Khan, John P. Gibbons (Jr.)." .

[41] H. (Hartmut) Zabel, *Medical physics. Volume 2, Radiology, lasers, nanoparticles and prosthetics*. .

[42] C. Borschel and C. Ronning, *Ion Beam Modification of Solids*, vol. 61. Springer International Publishing, 2016.

[43] C. M. L. West, "Introduction to radiobiology," *International Journal of Radiation Biology*, vol. 62, no. 1, Informa Healthcare, pp. 125–125, 1992.

[44] K. D. Held, "Basic Clinical Radiobiology," *Int. J. Radiat. Biol.*, vol. 86, no. 11, pp.

996–996, Nov. 2010, doi: 10.3109/09553002.2010.496030.

[45] “Radiobiology: Biologic effects of ionizing radiations|INIS.” https://inis.iaea.org/search/search.aspx?orig_q=RN:19076172 (accessed Jan. 12, 2020).

[46] J. H. Hendry, “Introduction to Radiobiology. Edited by M. Tubiana, J. Dutreix & A. Wambersie,” *Cell Prolif.*, vol. 24, no. 3, pp. 339–339, May 1991, doi: 10.1111/j.1365-2184.1991.tb01162.x.

[47] A. Van Der Kogel, *Basic Clinical Radiobiology*. 2009.

[48] S. Her and D. A. Jaffray, “Gold nanoparticles for applications in cancer radiotherapy: Mechanisms and recent advancements,” *Adv. Drug Deliv. Rev.*, vol. 109, pp. 84–101, Jan. 2017, doi: 10.1016/J.ADDR.2015.12.012.

[49] D. T. Goodhead, “Energy deposition stochastics and track structure: what about the target?,” *Radiat. Prot. Dosimetry*, vol. 122, no. 1–4, pp. 3–15, Dec. 2006, doi: 10.1093/rpd/ncl498.

[50] K. D. Held, “Radiobiology for the Radiologist, 6th ed., by Eric J. Hall and Amato J. Giaccia,” *Radiat. Res.*, vol. 166, no. 5, pp. 816–817, Nov. 2006, doi: 10.1667/rr0771.1.

[51] M. Mahesh, “The Essential Physics of Medical Imaging, Third Edition.,” *Med. Phys.*, vol. 40, no. 7, p. 077301, Jun. 2013, doi: 10.1118/1.4811156.

[52] J. Ma, F. Wang, and M. Mostafavi, “Ultrafast Chemistry of Water Radical Cation, H2O•+, in Aqueous Solutions,” *Molecules*, vol. 23, no. 2, p. 244, Jan. 2018, doi: 10.3390/molecules23020244.

[53] J. Gu, J. Leszczynski, and H. F. Schaefer, “Interactions of electrons with bare and hydrated biomolecules: From nucleic acid bases to DNA segments,” *Chemical Reviews*, vol. 112, no. 11. pp. 5603–5640, Nov. 14, 2012, doi: 10.1021/cr3000219.

[54] S. Yamashita, M. Taguchi, G. Baldacchino, and Y. Katsumura, “Radiation Chemistry of Liquid Water with Heavy Ions,” in *Charged Particle and Photon Interactions with Matter*, CRC Press, 2010, pp. 325–354.

[55] D. T. Goodhead, “Initial events in the cellular effects of ionizing radiations: Clustered damage in DNA,” *Int. J. Radiat. Biol.*, vol. 65, no. 1, pp. 7–17, 1994, doi: 10.1080/09553009414550021.

[56] L. J. Mah, R. S. Vasireddy, M. M. Tang, G. T. Georgiadis, A. El-Osta, and T. C. Karagiannis, “Quantification of γH2AX foci in response to Ionising radiation,” *J.*

Vis. Exp., no. 38, 2010, doi: 10.3791/1957.

[57] J. P. Banáth and P. L. Olive, “Expression of phosphorylated histone H2AX as a surrogate of cell killing by drugs that create DNA double-strand breaks,” *Cancer Res.*, vol. 63, no. 15, pp. 4347–4350, Aug. 2003.

[58] M. Mirza-Aghazadeh-Attari, A. Mohammadzadeh, B. Yousefi, A. Mihanfar, A. Karimian, and M. Majidinia, “53BP1: A key player of DNA damage response with critical functions in cancer,” *DNA Repair*, vol. 73. Elsevier B.V., pp. 110–119, Jan. 01, 2019, doi: 10.1016/j.dnarep.2018.11.008.

[59] I. Eke *et al.*, “53BP1/RIF1 signaling promotes cell survival after multifractionated radiotherapy,” *Nucleic Acids Res.*, vol. 48, no. 3, pp. 1314–1326, Dec. 2019, doi: 10.1093/nar/gkz1139.

[60] I. M. Ward, K. Minn, J. van Deursen, and J. Chen, “p53 Binding Protein 53BP1 Is Required for DNA Damage Responses and Tumor Suppression in Mice,” *Mol. Cell. Biol.*, vol. 23, no. 7, pp. 2556–2563, Apr. 2003, doi: 10.1128/mcb.23.7.2556-2563.2003.

[61] S. Panier and S. J. Boulton, “Double-strand break repair: 53BP1 comes into focus,” *Nature Reviews Molecular Cell Biology*, vol. 15, no. 1. pp. 7–18, Jan. 2014, doi: 10.1038/nrm3719.

[62] A. Subiel, R. Ashmore, and G. Schettino, “Standards and methodologies for characterizing radiobiological impact of high-Z nanoparticles,” *Theranostics*, vol. 6, no. 10. Ivyspring International Publisher, pp. 1651–1671, 2016, doi: 10.7150/THNO.15019.

[63] A. C. Wéra, H. Riquier, A. C. Heuskin, C. Michiels, and S. Lucas, “In vitro irradiation station for broad beam radiobiological experiments,” in *Nuclear Instruments and Methods in Physics Research, Section B: Beam Interactions with Materials and Atoms*, Dec. 2011, vol. 269, no. 24, pp. 3120–3124, doi: 10.1016/j.nimb.2011.04.104.

[64] N. A. P. Franken, H. M. Rodermond, J. Stap, J. Haveman, and C. van Bree, “Clonogenic assay of cells in vitro,” *Nat. Protoc.*, vol. 1, no. 5, pp. 2315–2319, Dec. 2006, doi: 10.1038/nprot.2006.339.

[65] S. B. Curtis, “Lethal and potentially lethal lesions induced by radiation - A unified repair model,” *Radiat. Res.*, vol. 106, no. 2, pp. 252–270, May 1986, doi: 10.2307/3576798.

[66] P. Sigmund, *Stopping of heavy ions : a theoretical approach*. Springer, 2004.

[67] S. J. Seo, J. K. Jeon, S. M. Han, and J. K. Kim, “Reactive oxygen species-based measurement of the dependence of the Coulomb nanoradiator effect on proton energy and atomic Z value,” *Int. J. Radiat. Biol.*, vol. 93, no. 11, pp. 1239–1247, Nov. 2017, doi: 10.1080/09553002.2017.1361556.

[68] “James Ziegler - SRIM & TRIM.” http://www.srim.org/.

[69] G. Baldacchino *et al.*, “Importance of radiolytic reactions during high-LET irradiation modalities: LET effect, role of O 2 and radiosensitization by nanoparticles,” *Cancer Nanotechnology*. 2019, doi: 10.1186/s12645-019-0047-y.

[70] E. B. Podgorsak, Ed., *Radiotherapy Oncology Physics: A Handbook for Teachers and Students*. Radiotherapy Oncology Physics: A Handbook for Teachers and Students, 2005.

[71] R. Pathak, S. K. Dey, A. Sarma, and A. R. Khuda-Bukhsh, “Cell killing, nuclear damage and apoptosis in Chinese hamster V79 cells after irradiation with heavy-ion beams of 16O, 12C and 7Li,” *Mutat. Res. - Genet. Toxicol. Environ. Mutagen.*, vol. 632, no. 1–2, pp. 58–68, Aug. 2007, doi: 10.1016/j.mrgentox.2007.04.007.

[72] S. Penninckx, A. C. Heuskin, C. Michiels, and S. Lucas, “Gold nanoparticles as a potent radiosensitizer: A transdisciplinary approach from physics to patient,” *Cancers*, vol. 12, no. 8. MDPI AG, pp. 1–361, Aug. 01, 2020, doi: 10.3390/cancers12082021.

[73] S. Li *et al.*, “Antibody-functionalized gold nanoparticles as tumor-targeting radiosensitizers for proton therapy,” *Nanomedicine*, vol. 14, no. 3, pp. 317–333, Feb. 2019, doi: 10.2217/nnm-2018-0161.

[74] P. Tiwari, K. Vig, V. Dennis, and S. Singh, “Functionalized Gold Nanoparticles and Their Biomedical Applications,” *Nanomaterials*, vol. 1, no. 1, pp. 31–63, Jun. 2011, doi: 10.3390/nano1010031.

[75] J. Shen, Y. Yang, Y. Zhang, H. Yang, Z. Zhou, and S. Yang, “Functionalized Au-Fe3O4 nanocomposites as a magnetic and colorimetric bimodal sensor for melamine,” *Sensors Actuators, B Chem.*, 2016, doi: 10.1016/j.snb.2015.12.029.

[76] J. F. Affonso de Oliveira, F. R. Scheffer, R. F. Landis, É. Teixeira Neto, V. M. Rotello, and M. B. Cardoso, “Dual Functionalization of Nanoparticles for Generating Corona-Free and Noncytotoxic Silica Nanoparticles,” *ACS Appl. Mater. Interfaces*, vol. 10, no. 49, pp. 41917–41923, Dec. 2018, doi:

10.1021/acsami.8b12351.

[77] A. Chompoosor *et al.*, “The Role of Surface Functionality on Acute Cytotoxicity, ROS Generation and DNA Damage by Cationic Gold Nanoparticles,” *Small*, vol. 6, no. 20, pp. 2246–2249, Oct. 2010, doi: 10.1002/smll.201000463.

[78] D. Kalyane, N. Raval, R. Maheshwari, V. Tambe, K. Kalia, and R. K. Tekade, “Employment of enhanced permeability and retention effect (EPR): Nanoparticle-based precision tools for targeting of therapeutic and diagnostic agent in cancer,” *Materials Science and Engineering C*, vol. 98. Elsevier Ltd, pp. 1252–1276, May 01, 2019, doi: 10.1016/j.msec.2019.01.066.

[79] X. Yi *et al.*, “Imaging-Guided Combined Photothermal and Radiotherapy to Treat Subcutaneous and Metastatic Tumors Using Iodine-131-Doped Copper Sulfide Nanoparticles,” *Adv. Funct. Mater.*, vol. 25, no. 29, pp. 4689–4699, Aug. 2015, doi: 10.1002/adfm.201502003.

[80] J. A. Coulter, K. T. Butterworth, and S. Jain, “Prostate cancer radiotherapy: potential applications of metal nanoparticles for imaging and therapy,” *Br. J. Radiol.*, vol. 88, no. 1054, p. 20150256, Oct. 2015, doi: 10.1259/bjr.20150256.

[81] H. L. Byrne *et al.*, “Enhanced MRI-guided radiotherapy with gadolinium-based nanoparticles: Preclinical evaluation with an MRI-linac,” *Cancer Nanotechnol.*, vol. 11, no. 1, p. 9, Oct. 2020, doi: 10.1186/s12645-020-00065-5.

[82] “Tumor Microenvironment-responsive multifunctional nanoplatform Based on MnFe2O4-PEG for Enhanced Magnetic Resonance Imaging-guided Hypoxic Cancer Radiotherapy,” *J. Mater. Chem. B*, doi: 10.1039/d0tb02631j.

[83] K. V. Katti *et al.*, “Hybrid gold nanoparticles in molecular imaging and radiotherapy,” *Czechoslov. J. Phys.*, vol. 56, no. 1, pp. D23–D34, Jan. 2006, doi: 10.1007/s10582-006-1033-2.

[84] N. G. Chabloz *et al.*, “Combined Magnetic Resonance Imaging and Photodynamic Therapy Using Polyfunctionalised Nanoparticles Bearing Robust Gadolinium Surface Units,” *Chem. – A Eur. J.*, vol. 26, no. 20, pp. 4552–4566, Apr. 2020, doi: 10.1002/chem.201904757.

[85] A. Banstola, F. Emami, J.-H. Jeong, and S. Yook, “Current Applications of Gold Nanoparticles for Medical Imaging and as Treatment Agents for Managing Pancreatic Cancer,” *Macromol. Res.*, pp. 1–10, Aug. 2018, doi: 10.1007/s13233-018-6139-4.

[86] X. Cai, Q. Zhu, Y. Zeng, Q. Zeng, X. Chen, and Y. Zhan, “Manganese Oxide

Nanoparticles As MRI Contrast Agents In Tumor Multimodal Imaging And Therapy," *Int. J. Nanomedicine*, doi: 10.2147/IJN.S218085.

[87] S. Harmsen, M. A. Wall, R. Huang, and M. F. Kircher, "Cancer imaging using surface-enhanced resonance Raman scattering nanoparticles," *Nat. Protoc.*, vol. 12, no. 7, pp. 1400–1414, Jun. 2017, doi: 10.1038/nprot.2017.031.

[88] H. L. Byrne *et al.*, "Enhanced MRI-guided radiotherapy with gadolinium-based nanoparticles: preclinical evaluation with an MRI-linac," *Cancer Nanotechnol.*, doi: 10.1186/s12645-020-00065-5.

[89] "MRI-traceable theranostic nanoparticles for targeted cancer treatment," *Theranostics*, doi: 10.7150/thno.48811.

[90] S. Bonvalot *et al.*, "First-in-human study testing a new radioenhancer using nanoparticles (NBTXR3) activated by radiation therapy in patients with locally advanced soft tissue sarcomas," *Clin. Cancer Res.*, vol. 23, no. 4, pp. 908–917, Feb. 2017, doi: 10.1158/1078-0432.CCR-16-1297.

[91] S. Bonvalot *et al.*, "NBTXR3, a first-in-class radioenhancer hafnium oxide nanoparticle, plus radiotherapy versus radiotherapy alone in patients with locally advanced soft-tissue sarcoma (Act.In.Sarc): a multicentre, phase 2–3, randomised, controlled trial," *Lancet Oncol.*, vol. 20, no. 8, pp. 1148–1159, Aug. 2019, doi: 10.1016/S1470-2045(19)30326-2.

[92] S. J. Seo *et al.*, "Enhanced production of reactive oxygen species by gadolinium oxide nanoparticles under core–inner-shell excitation by proton or monochromatic X-ray irradiation: implication of the contribution from the interatomic de-excitation-mediated nanoradiator effec," *Radiat. Environ. Biophys.*, vol. 54, no. 4, pp. 423–431, Aug. 2015, doi: 10.1007/s00411-015-0612-7.

[93] B. Yu, T. Liu, Y. Du, Z. Luo, W. Zheng, and T. Chen, "X-ray-responsive selenium nanoparticles for enhanced cancer chemo-radiotherapy," *Colloids Surfaces B Biointerfaces*, vol. 139, pp. 180–189, Mar. 2016, doi: 10.1016/j.colsurfb.2015.11.063.

[94] B. Ghaemi, O. Mashinchian, T. Mousavi, R. Karimi, S. Kharrazi, and A. Amani, "Harnessing the Cancer Radiation Therapy by Lanthanide-Doped Zinc Oxide Based Theranostic Nanoparticles," *ACS Appl. Mater. Interfaces*, vol. 8, no. 5, pp. 3123–3134, Feb. 2016, doi: 10.1021/acsami.5b10056.

[95] H. N. McQuaid *et al.*, "Imaging and radiation effects of gold nanoparticles in

tumour cells," *Sci. Rep.*, vol. 6, no. 1, p. 19442, May 2016, doi: 10.1038/srep19442.

[96] X. Liu *et al.*, "The synergistic radiosensitizing effect of tirapazamine-conjugated gold nanoparticles on human hepatoma HepG2 cells under X-ray irradiation," *Int. J. Nanomedicine*, vol. 11, pp. 3517–3531, Jul. 2016, doi: 10.2147/IJN.S105348.

[97] N. Ma *et al.*, "Shape-Dependent Radiosensitization Effect of Gold Nanostructures in Cancer Radiotherapy: Comparison of Gold Nanoparticles, Nanospikes, and Nanorods," *ACS Appl. Mater. Interfaces*, vol. 9, no. 15, pp. 13037–13048, Apr. 2017, doi: 10.1021/acsami.7b01112.

[98] S. Cho, B. Lee, W. Park, X. Huang, and D. H. Kim, "Photoperiodic Flower Mimicking Metallic Nanoparticles for Image-Guided Medicine Applications," *ACS Appl. Mater. Interfaces*, vol. 10, no. 33, pp. 27570–27577, Aug. 2018, doi: 10.1021/acsami.8b09596.

[99] J. Deng, S. Xu, W. Hu, X. Xun, L. Zheng, and M. Su, "Tumor targeted, stealthy and degradable bismuth nanoparticles for enhanced X-ray radiation therapy of breast cancer," *Biomaterials*, vol. 154, pp. 24–33, Feb. 2018, doi: 10.1016/j.biomaterials.2017.10.048.

[100] Y. Sun *et al.*, "FePt-Cys nanoparticles induce ROS-dependent cell toxicity, and enhance chemo-radiation sensitivity of NSCLC cells in vivo and in vitro," *Cancer Lett.*, vol. 418, pp. 27–40, Apr. 2018, doi: 10.1016/j.canlet.2018.01.024.

[101] M. Zabihzadeh *et al.*, "Enhancement of radio-sensitivity of colorectal cancer cells by gold nanoparticles at 18 MV energy," *18 MV energy. Nanomed J*, vol. 5, no. 2, pp. 111–120, Apr. 2018, doi: 10.22038/nmj.2018.005.008.

[102] M. Zangeneh, H. A. Nedaei, H. Mozdarani, A. Mahmoudzadeh, and M. Salimi, "Enhanced cytotoxic and genotoxic effects of gadolinium-doped ZnO nanoparticles on irradiated lung cancer cells at megavoltage radiation energies," *Mater. Sci. Eng. C*, vol. 103, p. 109739, Oct. 2019, doi: 10.1016/j.msec.2019.109739.

[103] V. J. Pizzuti *et al.*, "Folic Acid-Conjugated Radioluminescent Calcium Tungstate Nanoparticles as Radio-Sensitizers for Cancer Radiotherapy," *ACS Biomater. Sci. Eng.*, vol. 5, no. 9, pp. 4776–4789, Sep. 2019, doi: 10.1021/acsbiomaterials.9b00773.

[104] H. Sun, X. Wang, and S. Zhai, "The rational design and biological mechanisms

of nanoradiosensitizers," *Nanomaterials*, vol. 10, no. 3. MDPI AG, p. 504, Mar. 01, 2020, doi: 10.3390/nano10030504.

[105] Y. Li, K. H. Yun, H. Lee, S. H. Goh, Y. G. Suh, and Y. Choi, "Porous platinum nanoparticles as a high-Z and oxygen generating nanozyme for enhanced radiotherapy in vivo," *Biomaterials*, vol. 197, pp. 12–19, Mar. 2019, doi: 10.1016/j.biomaterials.2019.01.004.

[106] H. Nosrati, J. Charmi, M. Salehiabar, F. Abhari, and H. Danafar, "Tumor Targeted Albumin Coated Bismuth Sulfide Nanoparticles (Bi2S3) as Radiosensitizers and Carriers of Curcumin for Enhanced Chemoradiation Therapy," *ACS Biomater. Sci. Eng.*, vol. 5, no. 9, pp. 4416–4424, Sep. 2019, doi: 10.1021/acsbiomaterials.9b00489.

[107] A. Meidanchi and A. Motamed, "Preparation, characterization and in vitro evaluation of magnesium ferrite superparamagnetic nanoparticles as a novel radiosensitizer of breast cancer cells," *Ceram. Int.*, vol. 46, no. 11, pp. 17577–17583, Aug. 2020, doi: 10.1016/j.ceramint.2020.04.057.

[108] N. H. M. Zainudin, K. A. Razak, S. Z. Abidin, N. Dollah, and W. N. Rahman, "Investigation of the bismuth oxide nanoparticles on bystander effect in MCF-7 and hFOB 1.19 cells," in *Journal of Physics: Conference Series*, Apr. 2020, vol. 1497, no. 1, p. 12017, doi: 10.1088/1742-6596/1497/1/012017.

[109] S. Jafari, M. Cheki, M. B. Tavakoli, A. Zarrabi, S. K. Ghazikhanlu, and R. Afzalipour, "Investigation of combination effect between 6 MV X-ray radiation and polyglycerol coated superparamagnetic iron oxide nanoparticles on U87-MG cancer cells," *J. Biomed. Phys. Eng.*, vol. 10, no. 1, pp. 15–24, Feb. 2020, doi: 10.31661/jbpe.v0i0.929.

[110] F. Gao *et al.*, "Facile synthesis of Bi2S3-MoS2 heterogeneous nanoagent as dual functional radiosensitizer for triple negative breast cancer theranostics," *Chem. Eng. J.*, vol. 395, p. 125032, Sep. 2020, doi: 10.1016/j.cej.2020.125032.

[111] C. Peng *et al.*, "Hollow Mesoporous Tantalum Oxide Based Nanospheres for Triple Sensitization of Radiotherapy," *ACS Appl. Mater. Interfaces*, vol. 12, no. 5, pp. 5520–5530, Feb. 2020, doi: 10.1021/acsami.9b20053.

[112] R. Ahmad *et al.*, "Radiobiological Implications of Nanoparticles Following Radiation Treatment," *Part. Part. Syst. Charact.*, doi: 10.1002/ppsc.201900411.

[113] R. Casta, J. P. Champeaux, M. Sence, P. Moretto-Capelle, and P. Cafarelli, "Comparison between gold nanoparticle and gold plane electron emissions: a

way to identify secondary electron emission," *Phys. Med. Biol.*, vol. 60, no. 23, pp. 9095–9105, Nov. 2015, doi: 10.1088/0031-9155/60/23/9095.

[114] B. Damato, A. Kacperek, M. Chopra, I. R. Campbell, and R. D. Errington, "Proton beam radiotherapy of choroidal melanoma: The Liverpool-Clatterbridge experience," *Int. J. Radiat. Oncol. Biol. Phys.*, vol. 62, no. 5, pp. 1405–1411, Aug. 2005, doi: 10.1016/j.ijrobp.2005.01.016.

[115] R. Ahmad, G. Royle, A. Lourenço, M. Schwarz, F. Fracchiolla, and K. Ricketts, "Investigation into the effects of high-Z nano materials in proton therapy," *Phys. Med. Biol.*, vol. 61, no. 12, pp. 4537–4550, May 2016, doi: 10.1088/0031-9155/61/12/4537.

[116] I. Martínez-Rovira and Y. Prezado, "Evaluation of the local dose enhancement in the combination of proton therapy and nanoparticles," *Med. Phys.*, vol. 42, no. 11, pp. 6703–6710, Nov. 2015, doi: 10.1118/1.4934370.

[117] A. V. Belousov *et al.*, "The Change in the Linear Energy Transfer of a Clinical Proton Beam in the Presence of Gold Nanoparticles," *Biophys. (Russian Fed.*, vol. 65, no. 4, pp. 541–547, Jul. 2020, doi: 10.1134/S0006350920040053.

[118] D. Brivio *et al.*, "Kilovoltage radiosurgery with gold nanoparticles for neovascular age-related macular degeneration (AMD): a Monte Carlo evaluation," *Phys. Med. Biol.*, vol. 60, no. 24, pp. 9203–9213, Dec. 2015, doi: 10.1088/0031-9155/60/24/9203.

[119] J. Cho, C. Gonzalez-Lepera, N. Manohar, M. Kerr, S. Krishnan, and S. H. Cho, "Quantitative investigation of physical factors contributing to gold nanoparticle-mediated proton dose enhancement.," *Phys. Med. Biol.*, vol. 61, no. 6, pp. 2562–81, Mar. 2016, doi: 10.1088/0031-9155/61/6/2562.

[120] K. Rieck, K. Bromma, W. Sung, A. Bannister, J. Schuemann, and D. B. Chithrani, "Modulation of gold nanoparticle mediated radiation dose enhancement through synchronization of breast tumor cell population," *Br. J. Radiol.*, doi: 10.1259/bjr.20190283.

[121] R. Gabbasov, M. Polikarpov, V. Safronov, E. Sozontov, A. Yurenya, and V. Panchenko, "Monte Carlo simulation of dose distribution in water around 57Fe3O4 magnetite nanoparticle in the nuclear gamma resonance condition," *Hyperfine Interact.*, vol. 237, no. 1, p. 34, Dec. 2016, doi: 10.1007/s10751-016-1267-8.

[122] H. Yan *et al.*, "Monte Carlo dosimetry modeling of focused kV x-ray radiotherapy

of eye diseases with potential nanoparticle dose enhancement," *Med. Phys.*, vol. 45, no. 10, pp. 4720–4733, Oct. 2018, doi: 10.1002/mp.13144.

[123] S. H. Cho, "Estimation of tumour dose enhancement due to gold nanoparticles during typical radiation treatments: A preliminary Monte Carlo study," *Phys. Med. Biol.*, vol. 50, no. 15, p. N163, Aug. 2005, doi: 10.1088/0031-9155/50/15/N01.

[124] A. Ghasemi-Jangjoo and H. Ghiasi, "Monte Carlo study on the gold and gadolinium nanoparticles radio-sensitizer effect in the prostate 125I seeds radiotherapy," *Polish J. Med. Phys. Eng.*, doi: 10.2478/pjmpe-2019-0022.

[125] M. K. K. Leung, J. C. L. Chow, B. D. Chithrani, M. J. G. Lee, B. Oms, and D. A. Jaffray, "Irradiation of gold nanoparticles by x-rays: Monte Carlo simulation of dose enhancements and the spatial properties of the secondary electrons production," *Med. Phys.*, vol. 38, no. 2, pp. 624–631, Jan. 2011, doi: 10.1118/1.3539623.

[126] S. M. Gadoue, P. Zygmanski, and E. Sajo, "The dichotomous nature of dose enhancement by gold nanoparticle aggregates in radiotherapy," *Nanomedicine*, vol. 13, no. 8, pp. 809–823, Apr. 2018, doi: 10.2217/nnm-2017-0344.

[127] E. Porcel *et al.*, "Platinum nanoparticles: A promising material for future cancer therapy?," *Nanotechnology*, vol. 21, no. 8, p. 085103, Jan. 2010, doi: 10.1088/0957-4484/21/8/085103.

[128] J. D. Carter, N. N. Cheng, Y. Qu, G. D. Suarez, and T. Guo, "Nanoscale energy deposition by X-ray absorbing nanostructures," *J. Phys. Chem. B*, vol. 111, no. 40, pp. 11622–11625, Oct. 2007, doi: 10.1021/jp075253u.

[129] H. M. Garnica-Garza, "Microdosimetry of X-ray-irradiated gold nanoparticles," *Radiat. Prot. Dosimetry*, vol. 155, no. 1, pp. 59–63, Jun. 2013, doi: 10.1093/rpd/ncs278.

[130] Y. Lin, S. J. McMahon, M. Scarpelli, H. Paganetti, and J. Schuemann, "Comparing gold nano-particle enhanced radiotherapy with protons, megavoltage photons and kilovoltage photons: A Monte Carlo simulation," *Physics in Medicine and Biology*, vol. 59, no. 24. Institute of Physics Publishing, pp. 7675–7689, Dec. 21, 2014, doi: 10.1088/0031-9155/59/24/7675.

[131] J. C. Polf, L. F. Bronk, W. H. P. Driessen, W. Arap, R. Pasqualini, and M. Gillin, "Enhanced relative biological effectiveness of proton radiotherapy in tumor cells with internalized gold nanoparticles," *Appl. Phys. Lett.*, vol. 98, no. 19, May 2011, doi: 10.1063/1.3589914.

[132] C. Wang, X. Li, Y. Wang, Z. Liu, L. Fu, and L. Hu, “Enhancement of radiation effect and increase of apoptosis in lung cancer cells by thio-glucose-bound gold nanoparticles at megavoltage radiation energies,” *J. Nanoparticle Res.*, vol. 15, no. 5, 2013, doi: 10.1007/s11051-013-1642-1.

[133] D. Peukert, I. Kempson, M. Douglass, and E. Bezak, “Metallic nanoparticle radiosensitisation of ion radiotherapy: A review,” *Physica Medica*, vol. 47. Associazione Italiana di Fisica Medica, pp. 121–128, Mar. 01, 2018, doi: 10.1016/j.ejmp.2018.03.004.

[134] J. K. Kim *et al.*, “Enhanced proton treatment in mouse tumors through proton irradiated nanoradiator effects on metallic nanoparticles,” *Phys. Med. Biol.*, vol. 57, no. 24, pp. 8309–8323, Dec. 2012, doi: 10.1088/0031-9155/57/24/8309.

[135] M. Lainé *et al.*, “Reaction Mechanisms in Talc under Ionizing Radiation: Evidence of a High Stability of H• Atoms,” *J. Phys. Chem. C*, vol. 120, no. 4, pp. 2087–2095, Feb. 2016, doi: 10.1021/acs.jpcc.5b11396.

[136] L. Cui, S. Her, G. R. Borst, R. G. Bristow, D. A. Jaffray, and C. Allen, “Radiosensitization by gold nanoparticles: Will they ever make it to the clinic?,” *Radiother. Oncol.*, vol. 124, no. 3, pp. 344–356, Sep. 2017, doi: 10.1016/j.radonc.2017.07.007.

[137] O. Desouky, N. Ding, and G. Zhou, “Targeted and non-targeted effects of ionizing radiation,” *J. Radiat. Res. Appl. Sci.*, vol. 8, no. 2, pp. 247–254, Apr. 2015, doi: 10.1016/j.jrras.2015.03.003.

[138] Y. Mikami, A. Dhakshinamoorthy, M. Alvaro, and H. García, “Catalytic activity of unsupported gold nanoparticles,” *Catalysis Science and Technology*, vol. 3, no. 1. pp. 58–69, Jan. 2013, doi: 10.1039/c2cy20068f.

[139] B. Hvolbæk, T. V. W. Janssens, B. S. Clausen, H. Falsig, C. H. Christensen, and J. K. Nørskov, “Catalytic activity of Au nanoparticles,” *Nano Today*, vol. 2, no. 4. pp. 14–18, Aug. 2007, doi: 10.1016/S1748-0132(07)70113-5.

[140] Peter N. Njoki, Jin Luo, Lingyan Wang, Mathew M. Maye, and Huzaifa Quaizar, and C.-J. Zhong*, “Platinum-Catalyzed Synthesis of Water-Soluble Gold−Platinum Nanoparticles,” 2005, doi: 10.1021/LA047555I.

[141] Z. Zhang, A. Berg, H. Levanon, R. W. Fessenden, and D. Meisel, “On the interactions of free radicals with gold nanoparticles,” *J. Am. Chem. Soc.*, vol. 125, no. 26, pp. 7959–7963, Jul. 2003, doi: 10.1021/ja034830z.

[142] D. Mateo, P. Morales, A. Ávalos, and A. I. Haza, “Oxidative stress contributes to

gold nanoparticle-induced cytotoxicity in human tumor cells," *Toxicol. Mech. Methods*, vol. 24, no. 3, pp. 161–172, Mar. 2014, doi: 10.3109/15376516.2013.869783.

[143] Y. Pan *et al.*, "Gold Nanoparticles of Diameter 1.4 nm Trigger Necrosis by Oxidative Stress and Mitochondrial Damage," *Small*, vol. 5, no. 18, pp. 2067–2076, Sep. 2009, doi: 10.1002/smll.200900466.

[144] W. Su *et al.*, "Auger Electrons Constructed Active Sites on Nanocatalysts for Catalytic Internal Radiotherapy," *Adv. Sci.*, p. 1903585, Apr. 2020, doi: 10.1002/advs.201903585.

[145] A. A. Borran, A. Aghanejad, A. Farajollahi, J. Barar, and Y. Omidi, "Gold nanoparticles for radiosensitizing and imaging of cancer cells," *Radiation Physics and Chemistry*, vol. 152. Elsevier Ltd, pp. 137–144, Nov. 01, 2018, doi: 10.1016/j.radphyschem.2018.08.010.

[146] M. Misawa and J. Takahashi, "Generation of reactive oxygen species induced by gold nanoparticles under x-ray and UV Irradiations," *Nanomedicine Nanotechnology, Biol. Med.*, vol. 7, no. 5, pp. 604–614, Oct. 2011, doi: 10.1016/j.nano.2011.01.014.

[147] S. Klein *et al.*, "NOBF $_4$ -Functionalized Au–Fe $_3$ O $_4$ Nanoheterodimers for Radiation Therapy: Synergy Effect Due to Simultaneous Reactive Oxygen and Nitrogen Species Formation," *ACS Appl. Mater. Interfaces*, vol. 10, no. 20, pp. 17071–17080, May 2018, doi: 10.1021/acsami.8b03660.

[148] N. N. Cheng *et al.*, "Chemical Enhancement by Nanomaterials under X-ray Irradiation," *J. Am. Chem. Soc.*, vol. 134, no. 4, pp. 1950–1953, Feb. 2012, doi: 10.1021/ja210239k.

[149] F. Geng *et al.*, "Thio-glucose bound gold nanoparticles enhance radio-cytotoxic targeting of ovarian cancer," *Nanotechnology*, vol. 22, no. 28, p. 285101, Jul. 2011, doi: 10.1088/0957-4484/22/28/285101.

[150] C. Yao *et al.*, "Gold Nanoparticle Mediated Phototherapy for Cancer," *J. Nanomater.*, vol. 2016, pp. 1–29, 2016, doi: 10.1155/2016/5497136.

[151] S. Simonet *et al.*, "Gadolinium-Based Nanoparticles Can Overcome the Radioresistance of Head and Neck Squamous Cell Carcinoma Through the Induction of Autophagy," *J. Biomed. Nanotechnol.*, vol. 16, no. 1, pp. 111–124, Jan. 2020, doi: 10.1166/jbn.2020.2871.

[152] T.-L. Tsai, Y.-H. Lai, and H. H. W. Chen, "Overcoming radiation resistance by

iron-platinum metal alloy nanoparticles in human copper transport 1-overexpressing cancer cells via mitochondrial targeting," doi: 10.21203/rs.3.rs-63975/v1.

[153] K. Kobayashi, N. Usami, E. Porcel, S. Lacombe, and C. Le Sech, "Enhancement of radiation effect by heavy elements," *Mutation Research - Reviews in Mutation Research*, vol. 704, no. 1–3. pp. 123–131, Apr. 2010, doi: 10.1016/j.mrrev.2010.01.002.

[154] S. Lacombe, E. Porcel, and E. Scifoni, "Particle therapy and nanomedicine: state of art and research perspectives," *Cancer Nanotechnol.*, vol. 8, no. 1, p. 9, Dec. 2017, doi: 10.1186/s12645-017-0029-x.

[155] O. Roth, B. Dahlgren, and J. A. LaVerne, "Radiolysis of Water on ZrO_2 Nanoparticles," *J. Phys. Chem. C*, vol. 116, no. 33, pp. 17619–17624, Aug. 2012, doi: 10.1021/jp304237c.

[156] K. Rieck, K. Bromma, W. Sung, A. Bannister, J. Schuemann, and D. B. Chithrani, "Modulation of gold nanoparticle mediated radiation dose enhancement through synchronization of breast tumor cell population," *Br. J. Radiol.*, 2019, doi: 10.1259/bjr.20190283.

[157] J. Marill, N. Mohamed Anesary, and S. Paris, "DNA damage enhancement by radiotherapy-activated hafnium oxide nanoparticles improves cGAS-STING pathway activation in human colorectal cancer cells," *Radiother. Oncol.*, vol. 141, pp. 262–266, Dec. 2019, doi: 10.1016/j.radonc.2019.07.029.

[158] Z. Liu *et al.*, "Enhancement of radiotherapy efficacy by silver nanoparticles in hypoxic glioma cells," *Artif. Cells, Nanomedicine, Biotechnol.*, vol. 46, no. sup3, pp. S922–S930, Nov. 2018, doi: 10.1080/21691401.2018.1518912.

[159] M. Ghita, S. J. McMahon, L. E. Taggart, K. T. Butterworth, G. Schettino, and K. M. Prise, "A mechanistic study of gold nanoparticle radiosensitisation using targeted microbeam irradiation," *Sci. Rep.*, vol. 7, no. 1, p. 44752, 2017, doi: 10.1038/srep44752.

[160] Z. He, H. Yan, W. Zeng, K. Yang, and P. Rong, " Tumor microenvironment-responsive multifunctional nanoplatform based on MnFe 2 O 4 -PEG for enhanced magnetic resonance imaging-guided hypoxic cancer radiotherapy ," *J. Mater. Chem. B*, vol. 9, no. 6, pp. 1625–1637, Feb. 2021, doi: 10.1039/d0tb02631j.

[161] D. Howard, S. Sebastian, Q. V.-C. Le, B. Thierry, and I. Kempson, "Chemical

Mechanisms of Nanoparticle Radiosensitization and Radioprotection: A Review of Structure-Function Relationships Influencing Reactive Oxygen Species," *Int. J. Mol. Sci.*, vol. 21, no. 2, p. 579, Jan. 2020, doi: 10.3390/ijms21020579.

[162] L. Cui *et al.*, "Hypoxia and cellular localization influence the radiosensitizing effect of gold nanoparticles (AuNPs) in breast cancer cells," *Radiat. Res.*, vol. 182, no. 5, pp. 475–488, Nov. 2014, doi: 10.1667/RR13642.1.

[163] S. Penninckx, A.-C. Heuskin, C. Michiels, and S. Lucas, "Thioredoxin Reductase Activity Predicts Gold Nanoparticle Radiosensitization Effect," *Nanomaterials*, 2019, doi: 10.3390/nano9020295.

[164] J. T. Hancock, R. Desikan, and S. J. Neill, "Role of reactive oxygen species in cell signalling pathways," *Biochem. Soc. Trans.*, vol. 29, no. 2, pp. 345–349, May 2001, doi: 10.1042/bst0290345.

[165] E. Chelnokov *et al.*, "Electron transfer at oxide/water interfaces induced by ionizing radiation," *J. Phys. Chem. C*, vol. 118, no. 15, pp. 7865–7873, Apr. 2014, doi: 10.1021/jp501396a.

[166] S. W. Ryter *et al.*, "Mechanisms of cell death in oxidative stress," *Antioxidants and Redox Signaling*, vol. 9, no. 1. Mary Ann Liebert, Inc. 2 Madison Avenue Larchmont, NY 10538 USA , pp. 49–89, Jan. 20, 2007, doi: 10.1089/ars.2007.9.49.

[167] L. E. Taggart, S. J. McMahon, F. J. Currell, K. M. Prise, and K. T. Butterworth, "The role of mitochondrial function in gold nanoparticle mediated radiosensitisation," *Cancer Nanotechnol.*, vol. 5, no. 1, p. 5, Dec. 2014, doi: 10.1186/s12645-014-0005-7.

[168] S. J. McMahon, A. L. McNamara, J. Schuemann, K. M. Prise, and H. Paganetti, "Mitochondria as a target for radiosensitisation by gold nanoparticles," *J. Phys. Conf. Ser.*, vol. 777, no. 1, p. 012008, Jan. 2017, doi: 10.1088/1742-6596/777/1/012008.

[169] X. Fang *et al.*, "Mitochondria-targeting Au nanoclusters enhance radiosensitivity of cancer cells," *J. Mater. Chem. B*, vol. 5, no. 22, pp. 4190–4197, Jun. 2017, doi: 10.1039/c7tb00422b.

[170] H. Paquot, J. Daouk, A. Chateau, P. Rétif, M. Barberi-Heyoba, and S. Pinela, "Radiation-Induced Mitotic Catastrophe Enhanced by Gold Nanoparticles: Assessment with a Specific Automated Image Processing Workflow," *Radiat. Res.*, 2019, doi: 10.1667/rr14962.1.

[171] S. Jain *et al.*, “Cell-Specific Radiosensitization by gold nanoparticles at megavoltage radiation energies,” *Int. J. Radiat. Oncol. Biol. Phys.*, vol. 79, no. 2, pp. 531–539, Feb. 2011, doi: 10.1016/j.ijrobp.2010.08.044.

[172] T. M. Pawlik and K. Keyomarsi, “Role of cell cycle in mediating sensitivity to radiotherapy,” *Int. J. Radiat. Oncol. Biol. Phys.*, vol. 59, no. 4, pp. 928–942, Jul. 2004, doi: 10.1016/j.ijrobp.2004.03.005.

[173] M. A. Mackey, F. Saira, M. A. Mahmoud, and M. A. El-Sayed, “Inducing Cancer Cell Death by Targeting Its Nucleus: Solid Gold Nanospheres versus Hollow Gold Nanocages,” *Bioconjug. Chem.*, vol. 24, no. 6, pp. 897–906, Jun. 2013, doi: 10.1021/bc300592d.

[174] B. Kang, M. A. Mackey, and M. A. El-Sayed, “Nuclear targeting of gold nanoparticles in cancer cells induces DNA damage, causing cytokinesis arrest and apoptosis,” *J. Am. Chem. Soc.*, vol. 132, no. 5, pp. 1517–1519, Feb. 2010, doi: 10.1021/ja9102698.

[175] C. Yu *et al.*, “Targeted iron nanoparticles with platinum-(IV) prodrugs and anti-EZH2 siRNA show great synergy in combating drug resistance in vitro and in vivo,” *Biomaterials*, vol. 155, pp. 112–123, Feb. 2018, doi: 10.1016/j.biomaterials.2017.11.014.

[176] W. Roa *et al.*, “Gold nanoparticle sensitize radiotherapy of prostate cancer cells by regulation of the cell cycle,” *Nanotechnology*, vol. 20, no. 37, Sep. 2009, doi: 10.1088/0957-4484/20/37/375101.

[177] C. Deraedt *et al.*, “Sodium borohydride stabilizes very active gold nanoparticle catalysts,” *Chem. Commun.*, vol. 50, no. 91, pp. 14194–14196, Sep. 2014, doi: 10.1039/C4CC05946H.

[178] E. M. N. De Oliveira, M. S. Da Rocha, A. P. P. Froner, N. R. S. Basso, M. L. Zanini, and R. M. Papaléo, “Synthesis and nuclear magnetic relaxation properties of composite iron oxide nanoparticles,” *Quim. Nova*, vol. 42, no. 1, 2019, doi: 10.21577/0100-4042.20170309.

[179] E. C. Filippi-Chiela, M. M. Oliveira, B. Jurkovski, S. M. Callegari-Jacques, V. D. da Silva, and G. Lenz, “Nuclear morphometric analysis (NMA): Screening of senescence, apoptosis and nuclear irregularities,” *PLoS One*, vol. 7, no. 8, p. 42522, Aug. 2012, doi: 10.1371/journal.pone.0042522.

[180] S. Behzadi *et al.*, “Cellular uptake of nanoparticles: Journey inside the cell,” *Chemical Society Reviews*, vol. 46, no. 14. Royal Society of Chemistry, pp.

4218–4244, Jul. 21, 2017, doi: 10.1039/c6cs00636a.

[181] A. Banerjee, J. Qi, R. Gogoi, J. Wong, and S. Mitragotri, “Role of nanoparticle size, shape and surface chemistry in oral drug delivery,” *J. Control. Release*, vol. 238, pp. 176–185, Sep. 2016, doi: 10.1016/j.jconrel.2016.07.051.

[182] T. Dos Santos, J. Varela, I. Lynch, A. Salvati, and K. A. Dawson, “Quantitative assessment of the comparative nanoparticle-uptake efficiency of a range of cell lines,” *Small*, vol. 7, no. 23, pp. 3341–3349, Dec. 2011, doi: 10.1002/smll.201101076.

[183] K. T. Thurn *et al.*, “Endocytosis of titanium dioxide nanoparticles in prostate cancer PC-3M cells,” *Nanomedicine Nanotechnology, Biol. Med.*, vol. 7, no. 2, pp. 123–130, Apr. 2011, doi: 10.1016/j.nano.2010.09.004.

[184] H. Yasui *et al.*, “Radiosensitization of tumor cells through endoplasmic reticulum stress induced by PEGylated nanogel containing gold nanoparticles,” *Cancer Lett.*, vol. 347, no. 1, pp. 151–158, May 2014, doi: 10.1016/J.CANLET.2014.02.005.

[185] L. Štefančíková *et al.*, “Cell localisation of gadolinium-based nanoparticles and related radiosensitising efficacy in glioblastoma cells,” *Cancer Nanotechnol.*, vol. 5, no. 1, pp. 1–15, Oct. 2014, doi: 10.1186/s12645-014-0006-6.

[186] Yanli Liu, Mathew K. Shipton, Joseph Ryan, Eric D. Kaufman, * and Stefan Franzen, and D. L. Feldheim*, “Synthesis, Stability, and Cellular Internalization of Gold Nanoparticles Containing Mixed Peptide−Poly(ethylene glycol) Monolayers,” 2007, doi: 10.1021/AC061578F.

[187] Q. Xia, H. Li, Y. Liu, S. Zhang, Q. Feng, and K. Xiao, “The effect of particle size on the genotoxicity of gold nanoparticles,” *J. Biomed. Mater. Res. Part A*, vol. 105, no. 3, pp. 710–719, Mar. 2017, doi: 10.1002/jbm.a.35944.

[188] A. Mesbahi, F. Jamali, and N. Gharehaghaji, “Effect of photon beam energy, gold nanoparticle size and concentration on the dose enhancement in radiation therapy,” *BioImpacts*, vol. 3, no. 1, pp. 29–35, 2013, doi: 10.5681/bi.2013.002.

[189] Peukert, Kempson, Douglass, and Bezak, “Gold Nanoparticle Enhanced Proton Therapy: Monte Carlo Modeling of Reactive Species’ Distributions Around a Gold Nanoparticle and the Effects of Nanoparticle Proximity and Clustering,” *Int. J. Mol. Sci.*, vol. 20, no. 17, p. 4280, Sep. 2019, doi: 10.3390/ijms20174280.

[190] H. Dong, Y. Dai, X. Zhang, Z. Zhang, S. Fu, and Z. Zhong, “The influence of amine structures on the stability and catalytic activity of gold nanoparticles

stabilized by amine-modified hyperbranched polymers," *Nanotechnology*, vol. 29, no. 5, p. 055705, Feb. 2018, doi: 10.1088/1361-6528/aaa0fe.

[191] H. Ghaznavi *et al.*, "Folic acid conjugated PEG coated gold–iron oxide core–shell nanocomplex as a potential agent for targeted photothermal therapy of cancer," *Artif. Cells, Nanomedicine, Biotechnol.*, pp. 1–11, Oct. 2017, doi: 10.1080/21691401.2017.1384384.

[192] K. Haume, P. de Vera, A. Verkhovtsev, E. Surdutovich, N. J. Mason, and A. V. Solov'yov, "Transport of secondary electrons through coatings of ion-irradiated metallic nanoparticles," *Eur. Phys. J. D*, vol. 72, no. 6, Jun. 2018, doi: 10.1140/epjd/e2018-90050-x.

[193] R. Mehvar, "Dextrans for targeted and sustained delivery of therapeutic and imaging agents," *Journal of Controlled Release*, vol. 69, no. 1. Elsevier, pp. 1–25, Oct. 03, 2000, doi: 10.1016/S0168-3659(00)00302-3.

[194] L. Thoren, "The dextrans - Clinical data," *Dev. Biol. Stand.*, vol. Vol. 48, pp. 157–167, Jan. 1981, Accessed: Jun. 11, 2021. [Online]. Available: https://europepmc.org/article/med/6168501.

[195] S. Jain *et al.*, "Gold nanoparticle cellular uptake, toxicity and radiosensitisation in hypoxic conditions," *Radiother. Oncol.*, vol. 110, no. 2, pp. 342–347, Feb. 2014, doi: 10.1016/j.radonc.2013.12.013.

[196] C. Wang, Y. Jiang, X. Li, and L. Hu, "Thioglucose-bound gold nanoparticles increase the radiosensitivity of a triple-negative breast cancer cell line (MDA-MB-231)," *Breast Cancer*, vol. 22, no. 4, pp. 413–420, Jul. 2015, doi: 10.1007/s12282-013-0496-9.

[197] D. B. Chithrani *et al.*, "Gold Nanoparticles as Radiation Sensitizers in Cancer Therapy," *Radiat. Res.*, vol. 173, no. 6, p. 719, Jun. 2010, doi: 10.1667/rr1984.1.

[198] F. E. Stevens, H. Beamish, R. Warrener, and B. Gabrielli, "Histone deacetylase inhibitors induce mitotic slippage," *Oncogene*, vol. 27, no. 10, pp. 1345–1354, Feb. 2008, doi: 10.1038/sj.onc.1210779.

[199] H. Vakifahmetoglu, M. Olsson, and B. Zhivotovsky, "Death through a tragedy: Mitotic catastrophe," *Cell Death and Differentiation*, vol. 15, no. 7. Nature Publishing Group, pp. 1153–1162, Jul. 11, 2008, doi: 10.1038/cdd.2008.47.

[200] P. W. Nagle and R. P. Coppes, "Current and Future Perspectives of the Use of Organoids in Radiobiology," *Cells*, vol. 9, no. 12, p. 2649, Dec. 2020, doi: 10.3390/cells9122649.

Pontifícia Universidade Católica do Rio Grande do Sul
Pró-Reitoria de Graduação
Av. Ipiranga, 6681 - Prédio 1 - 3º. andar
Porto Alegre - RS - Brasil
Fone: (51) 3320-3500 - Fax: (51) 3339-1564
E-mail: prograd@pucrs.br
Site: www.pucrs.br